

[2014]

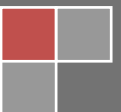
International Journal of Computational Engineering Research

Volume 04 Issue 12 December 2014

International Journal of Computational Engineering Research (IJCER) is dedicated to protecting personal information and will make every reasonable effort to handle collected information appropriately. All information collected, as well as related requests, will be handled as carefully and efficiently as possible in accordance with IJCER standards for integrity and objectivity.

IJCER

Open access Journal



Editorial Board

Editor-In-Chief

Prof. Chetan Sharma

Specialization: Electronics Engineering, India
Qualification: Ph.d, Nanotechnology, IIT Delhi, India

Editorial Committees

DR.Qais Faryadi

Qualification: PhD Computer Science
Affiliation: USIM(Islamic Science University of Malaysia)

Dr. Lingyan Cao

Qualification: Ph.D. Applied Mathematics in Finance
Affiliation: University of Maryland College Park,MD, US

Dr. A.V.L.N.S.H. HARIHARAN

Qualification: Phd Chemistry
Affiliation: GITAM UNIVERSITY, VISAKHAPATNAM, India

DR. MD. MUSTAFIZUR RAHMAN

Qualification: Phd Mechanical and Materials Engineering
Affiliation: University Kebangsaan Malaysia (UKM)

Dr. S. Morteza Bayareh

Qualificatio: Phd Mechanical Engineering, IUT
Affiliation: Islamic Azad University, Lamerd Branch
Daneshjoo Square, Lamerd, Fars, Iran

Dr. Zahéra Mekkioui

Qualification: Phd Electronics
Affiliation: University of Tlemcen, Algeria

Dr. Yilun Shang

Qualification: Postdoctoral Fellow Computer Science
Affiliation: University of Texas at San Antonio, TX 78249

Lugen M.Zake Sheet

Qualification: Phd, Department of Mathematics
Affiliation: University of Mosul, Iraq

Mohamed Abdellatif

Qualification: PhD Intelligence Technology
Affiliation: Graduate School of Natural Science and Technology

Meisam Mahdavi

Qualification: Phd Electrical and Computer Engineering

Affiliation: University of Tehran, North Kargar st. (across the ninth lane), Tehran, Iran

Dr. Ahmed Nabih Zaki Rashed

Qualification: Ph. D Electronic Engineering

Affiliation: Menoufia University, Egypt

Dr. José M. Merigó Lindahl

Qualification: Phd Business Administration

Affiliation: Department of Business Administration, University of Barcelona, Spain

Dr. Mohamed Shokry Nayle

Qualification: Phd, Engineering

Affiliation: faculty of engineering Tanta University Egypt

CONTENTS:

S.No.	Title Name	Page No.
Version I		
1.	The Aerial Wetted Path of Geostationary Transmission Luis G. Hidalgo , Jesús A. Hidalgo, Antonio Vidal	01-04
2.	The Impact of Interstitial Carbon on Dislocation Motion in the alpha-Fe Lattice K. D. Njoroge, G. O. Rading, J. M. Kihui, M. J. Witcomb, L. A. Cornish	05-09
3.	An Efficient approach of Integrated file Replication and Consistency Maintenance In peer-to-peer systems R.Sakunthala jenni , Dr.T.Pandikumar ,G.S.Aiswarya	10-14
4.	Detecting of NH ₃ , CO ₂ polluted gases by using ZnO- In ₂ O ₃ thin films Dr. Shatha Shammon Batros , Dr. Ghada Sabah Karam	15-21
5.	Implementation of Elliptic Curve Digital Signature Algorithm Using Variable Text Based Message Encryption with Message Digest Rajasekhar Bandapalle Mulinti, Dr.G.A.Ramachandra	22-30
6.	A Study on Partial Replacement of Natural Granite Aggregate with Pelletized Fly Ash Aggregate Dr. V.Bhaskar Desai , A.Sathyam	31-40
7.	An Experimental Investigation to Optimize the Process Parameters of Surface Finish in Turning AISI 202 Stainless Steel Using Taguchi Approach Anoop Pandey, Sandeep Garg, Payal Damle, Mahindra Rautela, Mohit Choudhary, Harshit Bhalla	41-45
8.	New Hybrid Intrusion Detection System Based On Data Mining Technique to Enhance Performance LUCKY SHARMA	46-53
9.	Implementation of a plus shaped fractal antennas for multi-band applications Maisarla.Chinnayya, Valluri.Dhana Raj, Dr.A.Mallikarjuna Prasad,Dr.M.Satyanarayana, Dr.G.M.V.Prasad	54-60

Version II

1.	Facial Expression Recognition System: A Digital Printing Application Mahasweta Mandal, Somnath Banerjee	01-12
2.	A Survey on Rendezvous Based Techniques for Power Conservation in Wireless Sensor Networks Ruthvic S D , Ravi B , Dr. Uday Kumar Shenoy	13-16
3.	Factors Affecting the Discharge Capacity of Shahi Katta Drain, Peshawar City Pakistan Navid Ahmad , Syed Salman A Shah , Gulfam Shahzad	17-21
4.	Study Of Strenth Charataristic Of Black Cotton Stablizing With Fly Ash And Rice Husk Ash Anil Kumar Singhai , Sudhanshu Shekhar Singh	22-27
5.	Study of Velocity and Pressure Distribution Characteristics Inside Of Catalytic Converter Geometry With Fluent 2D – Modeling & Simulation D. K. Sakhare , S.L.Sinha , S.P.Singh	28-33
6.	Audio Noise Removal – The State of the Art Srinidhi S Shetty , Reeja S R	34-37
7.	Efficient Load Balancing Routing in Wireless Mesh Networks S.Irfan	38-42
8.	Multimode Vector Modalities of HMM-GMM in Augmented Categorization of Bioacoustics' Signals Mayorga P. , Ibarra D. ,Druzgalski C.	43-52

The Aerial Wetted Path of Geostationary Transmission

Luis G. Hidalgo¹, Jesús A. Hidalgo² and Antonio Vidal³

¹ Universidad Central de Venezuela, Caracas, Venezuela.

² Universidad Simón Bolívar, Baruta, Sartenejas, Estado Miranda,

³ Universidad Simón Bolívar, Baruta, Sartenejas, Estado Miranda,

Abstract:

The aerial effective wetted path of geostationary satellite transmission focused to the Earth's surface was both defined taking into account the warm sector of rainy cloud and estimated as a function of signal strength. A standard path of 4.88 km was obtained for Caracas with a 60 cm dish parabolic receptor pointing with a 55° elevation angle to an associated direct TV satellite in Ku band. Such function helps to estimate rainfall intensity with ± 3 mm/h bulk error for stormy weather. Myriad of users of direct TV and other satellite applications with their receptors providing signal strength may apply the present issue to estimate paths and rain rates but doing verifications and adjusts by new coordinates and new dish sizes.

Keywords: Wetted, path, satellite, rainfall, geostationary, signal, strength

1. Introduction

The information transmitted from geostationary satellites toward receptors located at the Earth's surface must to cross the lower part of the atmosphere named *troposphere* in which the phenomenon of attenuation of the electromagnetic energy of the waves used for transmission occurs. The rain produces strong attenuation through a descending sloped distance across water droplets named here effective wetted path (D , km) with its vertical component supposed proportional to the rainfall intensity R (mm/h). Formulas give R from the unitary attenuation γ (dBz//km). Even though those receptors are not designed as rain gauges, the signal strength (S , %), most of the time included as a menu option in the commands of equipment, may be used to calculate decibels (dBz) but D remains unknown. Figure 1 shows the antenna of a receptor of direct TV transmission broadcasted by the G-3C satellite in a moment during a rainy event; the signal strength S was attenuated by rain from 98% to 80%. The objective here is then the estimation of D as a function of S to late calculate R . The R value may be considered important in times of abundant or scarce rain for human use of fresh water, thus any new issue on this matter would be reported. Receptors of direct TV transmission are considered here but other options may be useful. Myriad of users of direct TV and other satellite applications with receptors providing signal strength may apply the issue reported here to estimate both paths and rain rates but doing verifications and adjusts by new coordinates and new dish sizes.

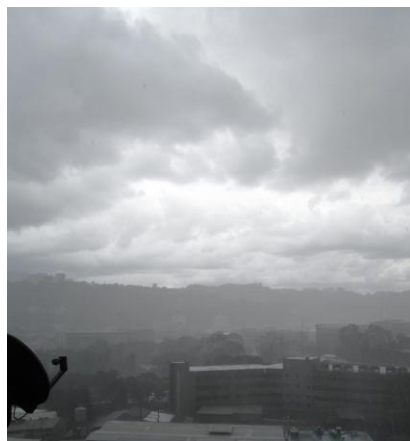


Figure 1. Image of a parabolic antenna of Direct TV receptor (TC121) during a rainy event.

2. Specific rainfall attenuation theory

A geostationary satellite transmits radio waves to the Earth's surface that can be captured by special device named receiver which has parabolic antenna composed by dish and horn at the front of the dish. The radio waves, most of the time in the microwave band, are composed by a combination of carrier, subcarrier and encoded data rename popularly *the signal*. The transmission must to cross the troposphere where a phenomenon named attenuation occurs. This phenomenon consists in the energy withdrawal of the carrier due to permanent and temporary factors. The permanent or basic attenuation is caused by fixed factors as the Fresnel divergence and energy abortion by CO_2 and O_2 . Energy withdrawal named *rain fade* caused by energy absorption and dispersion by temporary rainfall droplets is here the subject matter of study. Droplets reflect radio waves energy but water molecules absorb it. The relative signal strength S is measured respect to a standard from 0% to 100% by a meter included in the receptor. In the perfect receptor $S=0\%$ for strong *rain fade* with no detected signal but $S=100\%$ for no rainfall. The radio waves must to cross the troposphere in which the attenuation can be maximized by strong rains; the total length across rain showers in the clouds and below the clouds is the effective wetted path D (km). Designed for Caracas, Figure 2 helps to understand the wetted path dimension of the direct TV transmissions (Satellite G-3C) across a 12000 m high troposphere during heavy rainy episodes. The descending inclined wetted path runs $D_0=4883$ m from the 0°C ice level to TC121 crossing the condensation level at 500 m above TC121. The horizontal projection of this path reaches 2801 m. TC121 is located at altitude 877 m but 33 m above the soil. Data for that figure were obtained from [1]. In the present case S was measured with the TC121 receptor referred in Figure 1. The real D can be different to D_0 (km).

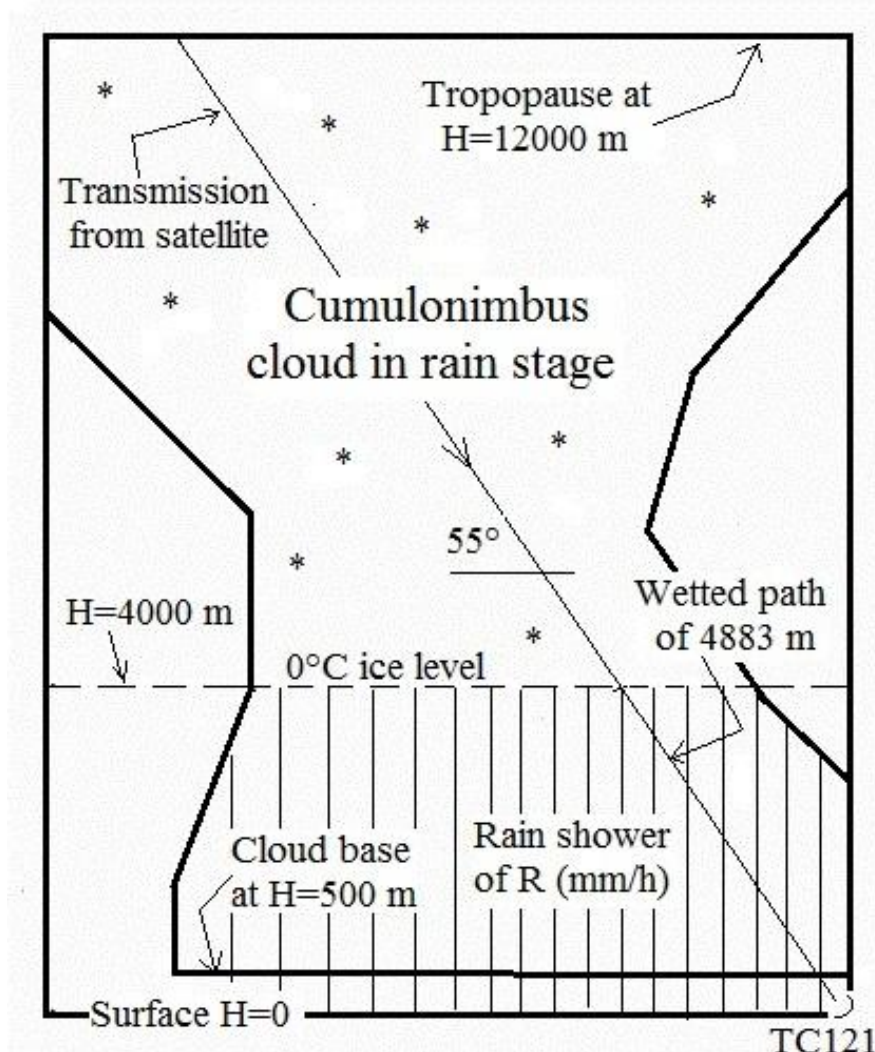


Figure 2. Standard scheme of transmission crossing a large rain stage cumulus over TC121.

The D valued will be actualized as follows. During no rains $S=S_{max}$ but during rains S is less than S_{max} and the attenuation is:

$$\gamma = [-\log(S/S_{max})]/D \quad (1)$$

Where γ is the bulk unitary attenuation in dBz/km, S is the signal strength measured with the meter in the receiver at a moment with rainfall and S_{max} is local S measured without rainfall; both for a specific satellite transponder. A transponder is a satellite device used to focus radio waves to areas of the Earth's surface. Most references present a standard formula for rain attenuation like this:

$$\gamma = a \cdot R^b \quad (2)$$

Where γ is the bulk unitary attenuation in dBz/km of horizontal radio wave at a specific moment crossing a falling down vertical shower of rainfall R (mm/h); constants a and b are parameters depending of the radio wave frequency. The International Telecommunication Union (ITU) presents mean values $a=0.0242$ and $b=1.1879$ for 12 GHz [2]. $D=0$ for $R=0$. To actualize D for each moment was used c value between 0 and 1 with the following linear interpolation:

$$D = c \cdot (1 - S/S_{max}) \cdot D_0 \quad (3)$$

3. Rain gauging experiments

During the years 2008 to 2012 were collected observational data of 7 storms that permitted to obtain pairs of true rainfall intensity R^* and S . In an electronic sheet was programmed the calculation of R from S assuming c values until the mean error of R^* minus R reaches zero with a specific standard deviation. The $c=1.84$ gave the zero error with standard deviation ± 2.9 mm/h. In those experiments was used transponder 13 with $S_{max}=98$. Table 1 shows results summary. The attenuation Beer's law may be used also for calculations but this was not intended here.

Day	Begin	End	R (mm/h)	R^* (mm/h)	Error (mm/h)
10Aug2009	16:00	17:00	14.7	17.0	-2.3
15Nov2009	13:00	14:00	13.4	13.0	0.4
30Jul2009	19:13	19:31	20.6	15.0	5.6
04Oct2009	16:58	18:45	15.9	15.1	0.8
23Oct2008	16:58	18:34	12.7	16.3	-3.5
04May2011	13:46	13:53	13.4	13.7	-0.3
12Jun2012	15:28	15:28	17.5	18.0	-0.5
					2.9

4. Effective or bulk wetted path

The maximum occasional value of the inclined wetted path corresponding to heavy cumulonimbus (Cb) rains reached temporary 1.84 times the standard value of 4.88 km or near 9 km assuring the presence of water droplets above the 0°C ice level inside Cb. Observations during jet flying in the area permitted detect the joint occurrence of ice crystal and droplets above the 0°C ice level touching the windows of the jets occasional. More information of this fact is not available due to notable gap of cloud physic studies in the area. The top of this kind of Cb clouds reaches height of 12 km near the *tropopause*.

5. Final verification

In 16 August 2014 for the 150 minutes from 16:35 to 19:05 local time were collected 157 values of S which were transformed in 157 values of R using the above formulation with $c=1.84$ to obtain a bulk intensity value of 19 mm/h against a measured value of 18 mm/h. Figure 3 shows detail of D variation during this complex rainy event. *Out-of-signal time* was 12 minutes. The error +1 mm/h is inside the above mentioned bulk of ± 3 mm/h, thus it may be considered acceptable. With this verification the present stage of research touches final but further research should be expected to minimize errors.

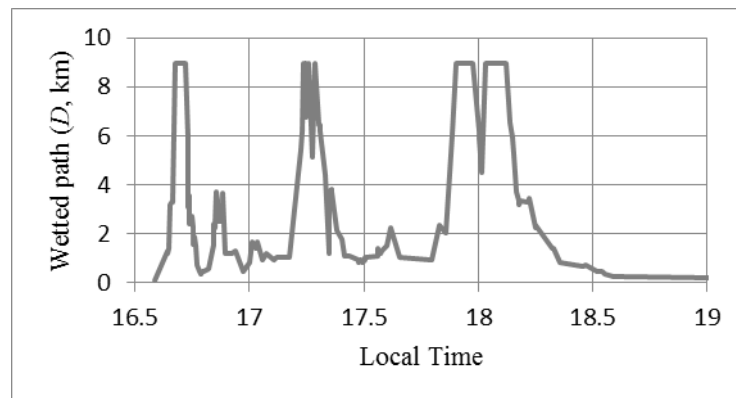


Figure 3. Histogram of wetted path during stormy episode of 16 August 2014.

6. Conclusions

It has been possible to estimate the wetted path of satellite transmission and the rainfall intensity from the signal strength measured with a low cost direct TV receptor during stormy weather episodes. An error of nearly ± 3 mm/h was obtained. The change of receptor to a dish of 120 cm instead the 60 cm used actually is recommendable to minimize error. Occasional *out-of-signal* events of heavy rainfall constitute the main restriction of the present development. As satellite geostationary transmission runs downward over an inclined path and the above mentioned rain attenuation formula was designed for horizontal path, more specific research on this subject must be undertaken to minimize errors doubtless.

7. Acknowledgments

We owe thanks to both the Telecommunication Technicians Ramon Arturo Hernandez who teaches us *rain fade* calculations and the Electronic Engineer Diego Stanfield who advices us on the possibility of watching the signal strength using menu options in most satellite receptors as that of direct TV.

References

- [1] L.G. Hidalgo and J. A. Hidalgo. Cálculo de la intensidad de lluvia por satélite. ISBN 9789801252429. 2011.
- [2] ITU. Specific attenuation model for rain for use in prediction models. ITU-R P-838-P. 2005

Figure and table captions should be 10-point boldface Helvetica (or a similar sans-serif font). Callouts should be 9-point non-boldface Helvetica. Initially capitalize only the first word of each figure caption and table title. Figures and tables must be numbered separately. For example: “Figure 1. Database contexts”, “Table 1. Input data”. Figure captions are to be centered *below* the figures. Table titles are to be centered *above* the tables.

The Impact of Interstitial Carbon on Dislocation Motion in the α -Fe Lattice

^{1,5} K. D. Njoroge, ^{1,5} G. O. Rading, ^{2,5} J. M. Kihiu, ^{3,5} M. J. Witcomb,
^{3,4,5} L. A. Cornish

¹ Department of Mechanical Engineering, School of Engineering, University of Nairobi
P.O. Box 30197-00100, Nairobi, Kenya.

² Department of Mechanical Engineering, Jomo Kenyatta University of Agriculture and Technology
P.O. Box 62000-00200, Nairobi, Kenya

³ DST-NRF Centre of Excellence in Strong Materials, University of the Witwatersrand
Private Bag 3, WITS, 2050, South Africa

⁴ School of Chemical and Metallurgical Engineering, University of the Witwatersrand
Private Bag 3, WITS, 2050, South Africa

⁵ African Materials Science and Engineering Network (AMSEN), a RISE Network.

ABSTRACT:

The effect of the introduction of interstitial carbon into the α -Fe lattice on the behavior of dislocation cores is presented. The simulations carried out were based on an EAM formulation that generated stress cycles resulting from the movement of dislocations, caused by the rigid displacement of rows of atoms on one side of a slip plane. The “path of least resistance” (POLR) mechanism accounting for stress evolution at the dislocation core was applied to predict the Peierls stress. This paper presents the behavior of the edge and screw dislocations in the Fe-C lattice.

Keywords: Embedded atom method; Body centered cubic; Dislocation cores; Peierls stress; Path of least resistance (POLR)

I. INTRODUCTION

This study was conducted as part of a project to develop a multi-scale simulation platform utilizing atomic scale phenomena as input in a mechanistic plasticity model. This stage sought to model the behavior of dislocation cores in the Fe-C lattice. To characterize the behavior of the dislocation core, the interaction of dislocation core atoms was established using the embedded atom method (EAM). The behavior of dislocation cores in body centered cubic (BCC) iron and the effects of interstitial carbon on the evolution of the dislocations are reported.

The structure of the dislocation core has been used to predict the physical behavior of the dislocation in terms of motion and evolution, and to determine the strain energy and the Peierls stress at which these physical actions take place. Peierls stress calculations for BCC metals have been driven by the realization that their dislocation core effects contribute to a high Peierls stress [1]. However, most of the studies characterize the lattice resistance by the changes in the binding energy, and reports on computations and experiments determining the Peierls stress for Fe are few.

Several methods have been applied to predict the Peierls stress. The Peierls-Nabarro model [2,3] utilized inter-planar de-registry between rows of atoms to develop an analytical expression to predict the Peierls peak. This model did not account for the dislocation core structure and was initially confined to 2-dimensional geometry. Additionally, it was limited to a homogeneous system of atoms and did not account for variations in the inter-atomic interactions. A review of the evolution of this model was presented by Nabarro [4]. Lubarda and Markenscoff [5] proposed a variable core model to develop an analytical expression to predict the Peierls stress. Their model applied the shear stress of a distribution of infinitesimal dislocations to predict the energy of the whole stressed crystal between the stable equilibrium and the unstable states of the dislocation. This approach therefore did not apply the sinusoidal relationship between the shear stress and slip discontinuity along the slip plane as in the Peierls-Nabarro model [4].

Duesbery [6], Xu [7] and Wang et al. [8] presented the application of inter-atomic potentials in the computation of the core structure and the Peierls stress of dislocations. This method gave a more versatile approach to the modeling of varied spatial arrangements and elemental configurations. However, the method was limited to the suitability of the potentials used and the need to maintain a small atomic volume to accommodate computational limitations. Electronic structure calculations employing density functional theory based calculations were reported by Shimizu et al. [9,10]. This method was limited by the need to keep the simulation volume small, due computational constraints and the effects of boundary conditions on the electron field. This method has found application where a varied elemental configuration and non-equilibrium spatial arrangements are important.

In all these approaches, snapshots of various configurations of the evolving dislocation were considered. In contrast, Terentyev, Osetsky and Bacon [11] and Wang et al. [12] applied molecular dynamics to study the mobility of dislocations in BCC elements. In this approach, the application of dynamics allowed the spatial evolution of the lattice points to define the physical state of the material matrix, providing more realistic results in the computation.

Comparisons of the Peierls stress values determined by several different researchers [10,11,13,14] and the amplitude of the “path of least resistance” (POLR) stress [15] reveal some correlation between the two properties. The POLR value for the pure screw dislocation of 1.01 GPa [15] and symmetric screw dislocation of 1.883 GPa [15] compared well with density functional theory based calculations reported by Kaburaki [10] of a Peierls stress of 1.1 GPa for the screw dislocation in a stress driven computation with an initial symmetric screw dislocation configuration. However, Njoroge et al. [15] neglected to discuss the evolution of the configuration of the dislocation and it is unclear if the Peierls stress documented applies to the pure screw or the symmetric screw dislocation. These results [15] also suggested that the Peierls stress of the pure edge dislocation was higher than that of the pure screw dislocation. This inconsistency was explained by visualizing the edge dislocation motion as a multi-step translation of $[\bar{1} 1 1]$ and $[001]$ motions. The edge dislocation Peierls stress was therefore more closely related to the POLR value for the edge dislocation moving in the $[\bar{1} 1 1]$ direction of 1.578 GPa [15]. Similar inversion of relative Peierls stress values for the edge and screw dislocations were reported by Terentyev, Osetsky and Bacon [11]: 1.5 GPa for the edge dislocation and 1.4 GPa for the screw dislocation. They attributed this anomaly to the constriction of the edge dislocation core at the Peierls peak that inhibits dislocation motion.

Petukhov [16] reported a Peierls stress for a dislocation kink of 0.95 GPa. Available empirical findings on the dislocation kink [1] led to the conclusion that the edge dislocation component processes a greater mobility than the screw component. It may be inferred that the edge dislocation would have a Peierls stress in the order of 0.95 GPa. The POLR value of 1.578 GPa [15] for the edge dislocation moving in the $[\bar{1} 1 1]$ direction therefore compared much more favourably with the Peierls stress reported by Petukhov [16] and supported the assertion that the edge dislocation was more likely to move by a combination of $[\bar{1} 1 1]$ and $[001]$ motions. Terentyev, Osetsky and Bacon [11] reported a Peierls stress of 1.5 GPa at T=0K for a $\langle 100 \rangle$ edge dislocation in α -Fe. This result compared well with the POLR value for the $\langle \bar{1}12 \rangle$ edge dislocation moving in the $[\bar{1} 1 1]$ direction and further reinforced the assertion that the edge dislocation moved by a combination of $[\bar{1} 1 1]$ and $[001]$ motions [15]. Njoroge et al. [15] also showed an increase in the Peierls stress for the screw dislocation on the introduction of a symmetric dislocation core reconstruction. These findings therefore suggested that the screw components in dislocation kinks would contain appreciable sections of reconstruction defects, which would result in a higher POLR value for the screw component than the edge dislocation moving in the $[\bar{1} 1 1]$ direction. The POLR technique was therefore considered an acceptable approach in the estimation of the Peierls peak.

II.METHOD

Simulations in this work were carried out on computer code using the Fe-Fe potential developed by Mendelev et al. [17] in an embedded atom method formulation. This potential has been tested and found to stabilize the non-degenerate dislocation core sliding on $\{110\}$ glide planes, in agreement with experimental data for dislocation motion at low temperatures [13]. The formulation also applied the potential by Becquart et al. [18], which has been found to be suitable for modeling of a single element lattice with interstitial impurities. This combination of potentials was applied in this study of ferritic Fe-C solid solutions with low carbon concentrations.

Introduction of the initial distortion was achieved by the application of the distortion vector to atoms on one side of the slip plane. The distortion vector was selected such that together with the dislocation line, it defined the type of dislocation introduced. Dislocation flips were achieved by the application of displacement vectors to the core atoms, according to the definition of each type of dislocation flip. The resulting additional distortion was transferred to the dislocated lattice by a suitable algorithm. The carbon atoms were introduced at the octahedral interstitial sites at a frequency of one carbon atom in each BCC unit cell along the dislocation core.

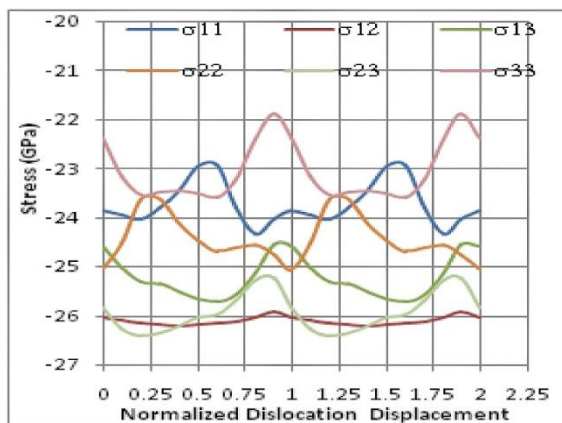
Dislocation dynamics was achieved by rigidly displacing atoms on one side of the slip plane using atomic scale displacements. A uniform dislocation line displacement vector was applied. In this technique, no effort was made to attain equilibrium conditions, as these were considered unlikely in actual loading conditions. This work evaluated the stresses cycles and predicted the Peierls stress of the type of dislocation. The dislocation core stress components were calculated at lattice sites occupied by atoms adjacent to the slip plane. The simulations generated stress components σ_{ij} corresponding to the Cartesian coordinate system coincident with the edges of the BCC unit cell. Benchmarking of the simulation results was achieved by comparison with data generated by other researchers [10,13,14,16] using empirical and *ab initio* techniques.

III. RESULTS AND DISCUSSION

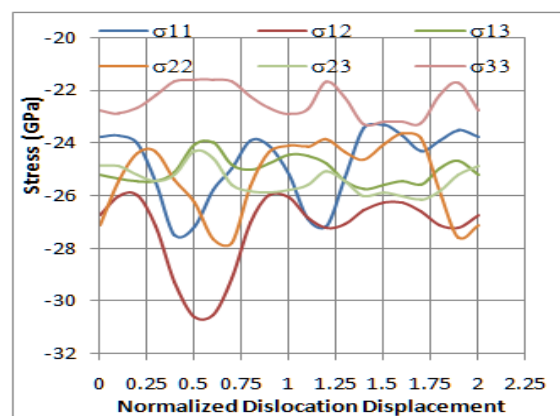
Simulations of the motion of the edge and screw dislocations were carried out and curves of the six independent stress components plotted in Figures 1 and 2. All dislocations generated cyclic stress variations for all stress components, differing in the pattern formed and the amplitude of individual curves. The cyclic behaviour is consistent with dislocation behaviour described in the Peierls-Nabarro model [19,20]. The positive and negative values were interpreted as tensile and compressive stresses respectively, and it was noted that the direct stress were negative for the Fe-C lattice.

1.1. Screw Dislocation

The stress curves for screw dislocation core in the Fe-C lattice are presented in Figure 1. The curves show an increase in stress component values of -21.9 GPa to -26.4 GPa, up from 5.41 GPa to -6.44 GPa in the carbon free lattice [15]. The introduction of interstitial carbon in the Fe lattice therefore resulted in a considerable increase in lattice resistance to dislocation motion. These results are in qualitative agreement with existing knowledge where carbon in the Fe lattice enhances yield strength. In addition, the introduction of interstitial carbon resulted in compressive stresses in the dislocation core as the dislocation moved through the lattice. This observation is consistent with the formation of matensite in the Fe-C lattice, which forms as a body centered tetragonal (BCT) structure above a concentration of 0.6% carbon by mass [21], and which is closely related to the BCC lattice adopted by the simulations.



$\bar{\sigma}$ I



$\bar{\sigma}$ 1

$\bar{\sigma}$

$\bar{\sigma}$

$[\bar{1}\bar{1}1]$

$\bar{\sigma}$

$[\bar{1}\bar{1}2]$

$\bar{\sigma}$

The curves in Figure 1 give a POLR value of 1.6 GPa. The directions generating the POLR correspond to σ_{33} and σ_{11} stress components, with σ_{33} providing the major contribution. It is also noteworthy that the direct stresses provide the POLR, as was the case in for the carbon-free lattice [15]. The amplitude of the POLR changed from 1.01 GPa [15] to 1.6 GPa as interstitial carbon was introduced. This is consistent with the expected strengthening of the lattice with introduction

of interstitial carbon. The stress amplitude is of the same order of magnitude as the Peierls stress, and it is suggested that this parameter is more closely related to the Peierls stress than the absolute stress value of the stress cycle.

1.2. Edge Dislocation

The stress curves for edge dislocation core in the Fe-C lattice are shown in Figure 2. The POLR amplitude increased from 1.578 GPa for the edge dislocation moving in the $[\bar{1}11]$ direction [15] in a carbon-free lattice to 1.7 GPa in the Fe-C lattice. This increase in amplitude suggests that dislocation mobility decreased on the introduction of carbon into the lattice. This is consequent with empirical findings at the macro-scale which suggest that dislocation motion is inhibited by interstitial carbon atoms [22].

The pattern of the stress curves for the Fe-C lattice is similar to that observed for the carbon-free lattice. However, unlike the curves for the carbon-free lattice, the intersections of stress component curves were reduced, implying a reduction in the number of degrees of freedom of motion for this dislocation. Consequently, it was concluded that the edge dislocation motion in the Fe-C lattice should experience a reduction in the ability of dislocation core atoms to “peel” around the core, and this would result in a lower mobility of this dislocation. This inference is consistent with the relatively brittle nature of the Fe-C lattice.

1.3. The Peierls Stress For BCC Lattice Structures

A summary of the active stresses simulated by the POLR for the Fe-C lattice is shown in Table 1. The results reveal an increase in the stress amplitude for the screw and the edge dislocations consistent with expectations. Clouret et al. [23] demonstrated that the binding energy of the carbon atom to dislocation core sites was higher for the edge dislocation than the screw dislocation. A consequence of this observation was that carbon forming Cottrell atmospheres would result in more effective pinning of the edge dislocation core, and hence a higher Peierls stress [23]. This was consistent with the current results where the edge dislocation presented a higher POLR value than the screw dislocation.

Dislocation Type	Stress Range (GPa)		Stress Amplitude (GPa) - POLR	Peierls stress (GPa)
	Lower	Upper		
Symmetric screw	-22.3	-24.0	1.7	-
Anti-symmetric screw	-22.7	-26.8	4.1	-
Pure screw	-21.9	-23.5	1.6	1.2 - 1.8 [11,13]; 1.3 - 1.8 [14]; 1.1 [10]
70.53° screw	-21.6	-23.2	1.6	-
35.26° screw	-21.5	-23.4	1.9	-
Pure edge	-21.6	-23.3	1.7	1.5 [11]

IV. CONCLUSIONS

It is concluded that the path of least resistance (POLR) stress is related to the Peierls stress for the Fe-C lattice. It is also concluded that the Peierls stress is attributed to the contribution of dislocation core direct stress components, and that the variation of the POLR stress between the different dislocation types is not significant in the Fe-C lattice. It is noted that data on the stress tensor components in Fe-C lattice as dislocations move through the lattice have not been presented elsewhere, to the best of the authors’ knowledge.

ACKNOWLEDGEMENTS

This research has been supported by the African Materials Science and Engineering Network (AMSEN) funded by the Carnegie Corporation of New York. This support is greatly appreciated.

REFERENCES

- [1]. C. Woodward, S.I. Rao., Flexible Ab Initio Boundary Conditions: Simulating Isolated Dislocations in BCC Mo & Ta. *Physical Review Letters*. 2002, Vol. 88, 21, pp. 6402-6405.
- [2]. R. Peierls. The Size of the Dislocation. *Proceedings of the Physical Society*. 1940, Vol. 52, pp. 34-37.
- [3]. F. R. N. Nabarro. Dislocations in Simple Cubic Lattice. *Proceedings of the Physical Society*. 1947, Vol. 59, 2, pp. 256-272.
- [4]. F. R. N. Nabarro. Fifty-year study of the Peierls-Nabarro stress. *Materials Science and Engineering*. 1997, Vols. A234-236, pp. 67-76.
- [5]. V. A. Luarda, X. Markenscoff. Variable Core Model and the Peierls Stress for the Mixed (Screw-Edge) Dislocation. *Applied Physics Letters*. 2006, Vol. 89, 151923.
- [6]. M. S. Duesbery. On Kinked Screw Dislocations in the BCC Lattice I: The Structure and Peierls Stress of Isolated Kinks. *Acta Metallurgica*. 1983, Vol. 31, 10, pp. 1747-1750.
- [7]. W. Xu, J. Moriarty. Accurate Atomistic Simulations of the Peierl's Barrier and Kink-Pair Formation Energy for $\langle 111 \rangle$ Screw Dislocations in BCC Mo. *Computational Material Science*. 1998, Vol. 9, 3-4, pp. 348-356.
- [8]. G. Wang, A. Strachan, T. Cagun, W. A. Goddard. Role of Core Polarization Curvature of Screw Dislocations in Determining the Peierls Stress in BCC Ta: A Criterion for Designing High-Performance Materials. *Physical Review B*. 2003, Vol. 67, 14, pp. 1-4.
- [9]. F. Shimizu, S. Ogata, H. Kimizuka, T. Kano, J. Lu, H. Kaburaki. First Principles Calculation on Screw Dislocation Core Properties in BCC Molybdenum. *Journal of Earth Simulator*. 2007, Vol. 7, pp. 17-21.

- [10]. **F. Shimizu, S. Ogata, M Yamaguchi, T. Kano, H. Kimizuka, M. Itakura, H. Kaburaki,** *First Principles Calculation on Core Structures and Peierls Stress of a Screw Dislocation in BCC Iron*. Japan Atomic Energy Agency . s.l. : Epoch Making Simulation, 2007. Chapter 3 Epoch Making Simulation.
- [11]. **D. A. Terentyev, Y. N. Osetsky, D. J. Bacon.** Effects of Temperature on Structure and Mobility of the <100> Edge Dislocation in Body Centered Cubic Iron. *Acta Materialia*. 2010, Vol. 58, 7, pp. 2477-2482.
- [12]. **G. Wang, A. Strachan, T. Cagin, W. A. Goddard III.** Calculating the Peierls Energy and Peierls Stress from Atomistic Simulations of Screw Dislocation Dynamics: Application to BCC Tantalum. *Modelling and Simulation in Materials Science and Engineering*. 2004, Vol. 12, pp. S371-S389.
- [13]. **J. Chaussidon, M. Fivel, D. Rodney.** The Glide of Screw Dislocations in BCC Fe: Atomistic Static and Dynamic Simulations. *Acta Materialia*. 2006, Vol. 54, 13, pp. 3407-3416.
- [14]. **L. Ventelon.** *Core Structure of Screw Dislocations in Fe From First-Principles*. Department of Materials for Nuclear Energy at the Nuclear Energy Division, Commissariat à l'énergie Atomique et aux Energies Alternatives. 2008. PhD Thesis.
- [15]. **K. D. Njoroge, G. O. Rading, J. M. Kihiu, M. J. Witcomb, L. A. Cornish.** Dynamic Analysis of Dislocation Cores in a-Fe Lattice Using the Embedded Atom Method. *International Journal of Computational Engineering Research*. 2012, Vol. 2, 3, pp. 851-859.
- [16]. **B. V. Petukhov.** Theory of Solid Solution Softening in Comparison with Experiments on alpha-Fe. *Physica Status Solidi (A)*. 1985, Vol. 90, 1, pp. 225-229.
- [17]. **M. I. Mendelev, S. Han, D. J. Srolovitz, G. J. Ackland, D. Y. Sun, M. Asta.** Development of Interatomic Potentials appropriate for Crystalline and Liquid Iron. *Philosophical Magazine*. 2003, Vol. 83, 35, pp. 3977-3994.
- [18]. **C. S. Becquart, J. M. Raulot, G. Bencteux, C. Domain, M. Perez, S. Garruchet, H. Nguyen.** Atomistic Modeling of an Fe System with a Small Concentration of C. *Computational Materials Science*. 2007, Vol. 40, pp. 119-129.
- [19]. **Y. Yao, T. Wang.** Peierls Nabarro Model of Interfacial Misfit Dislocation: An Analytical Solution. *Physical Review B*. 1999, Vol. 59, 12, pp. 8232-8236.
- [20]. **B. Joos, J. Zhou.** The Peierls Nabarro Model and the Mobility of the Dislocation Line. *Philosophical Magazine A*. 2001, Vol. 81, 5, pp. 1329-1340.
- [21]. **O. D. Sherby, J. Wadsworth, D. R. Lesuer, C. K. Syn.** Revisiting the Structure of Martensite in Iron-Carbon Steels. *Materials Transactions*. 2008, Vol. 49, 9, pp. 2016 - 2027.
- [22]. **D. Caillard.** An In Situ Study of Hardening and Softening of Iron by Carbon. *Acta Materialia*. 2011, Vol. 59, 15, pp. 4974-4989.
- [23]. **E. Clouet, S. Garruchet, H. Nguyen, M Perez, C. S. Becquart.** Dislocation Interaction with C in a-Fe: A Comparison Between Atomic Simulations and Elasticity Theory. *Acta Materialia*. 2008, Vol. 56, pp. 3450-3460.

An Efficient approach of Integrated file Replication and Consistency Maintenance In peer-to-peer systems

R.Sakunthala jenni¹, Dr.T.Pandikumar²,G.S.Aiswarya³

1. Assistant Professor, Department of Computer Science and Engineering, Kalaivani College of Technology, Coimbatore, India-641105,
2. Associate Professor, Dept. of Computer and Information Technology, Defence University, Ethiopia.
3. Assistant Professor, Department of Electronics and communication Engineering, Tamizhan College of Engineering and Technology, Kanyakumari, India-629304,

ABSTRACT:

Peer-to-Peer is a decentralized system which is well known for its high scalability and reliability. So applications on a P2P system are used widely now days. For high system performance of this peer-to-peer file sharing systems, file replication and consistency maintenance are widely used techniques. These two techniques are intimately connected to each other. File replication needs consistency maintenance to keep the consistency between a file and its replicas, and on the other hand, the overhead of consistency maintenance is determined by the number of replicas. Connecting the two important components will greatly enhance system performance. Traditional file replication and consistency maintenance methods either are not sufficiently effective or incur prohibitively high overhead. To overcome these, IRM (Integrated file Replication and Consistency Maintenance in P2P systems) can be used which will achieve high efficiency at a significantly lower cost. Instead of passively accepting replicas and updates, nodes autonomously determine the need for file replication and validation based on file query rate and update rate. It guarantees the high utilization of replicas, high query efficiency and fidelity of consistency. IRM reduces redundant file replicas, consistency maintenance overhead, and unnecessary file updates.

Keywords: Consistency Maintenance, File Replication, Replica Node, Peer-to-Peer.

I. INTRODUCTION

Now in a P2P file sharing system, every node has a routing table regarding its neighbors. So when a node requests a file the request will be forwarded to the file's destination and then the file will be sent back to the requester. In P2P file sharing systems, the file access is highly repetitive. So if a node becomes a hot spot, there will be a delayed response. File replication is one solution to deal with such problems. It replicates a file to some other node in order to distribute the query load among the number of nodes and to avoid a hot spot so the file query efficiency can be enhanced. File replication means file consistency maintenance in order to keep the consistency between file and its replicas. For example, a file is changing all its replicas should be updated corresponding.

File replication is an effective method to deal with the problem of overload condition due to flash crowds or hot files. It distributes load over replica nodes and improves file query efficiency. File consistency maintenance to maintain the consistency between a file and its replicas is indispensable to file replication. In most current file replication methods, file owners rigidly specify replica nodes and the replica nodes passively accept replicas. The methods were designed without considering the efficiency of subsequent file consistency maintenance. The number of replicas has a significant impact on the overhead of file consistency maintenance. Large number of replicas needs more updates hence high consistency maintenance overhead and vice versa. So the methods lead to high overhead for unnecessary file replications and consistency maintenance.

IRM integrates file replication and consistency maintenance in a harmonized and coordinated manner. IRM achieves high efficiency in file replication and consistency maintenance at a significantly lower cost. Each node actively decides to create or delete a replica and to poll for update based on file query and update rates in a totally decentralized and autonomous manner. IRM improves replica utilization, file query efficiency, and consistency fidelity. It avoids unnecessary file replications and updates by dynamically adapting to time varying

file query and update rates. A significant feature of IRM is that it achieves an optimized trade-off between overhead and query efficiency as well as consistency guarantees.

IRM is good for P2P systems due to a number of reasons. 1) IRM does not require a file owner to keep track of replica nodes. So, it is resilient to node joins and leaves, and thus suitable for highly dynamic P2P systems. 2) Since each node determines its need for a file replication or replica update autonomously, the decisions can be made based on its actual query rate, eliminating unnecessary replications and validations. 3) IRM enhances the guarantee of file consistency. It offers the flexibility to use different replica update rate to cater to different consistency requirements determined by the nature of files and user needs. 4) IRM ensures high possibility of up-to-date file responses.

II. RELATED WORKS

File replication in P2P systems is targeted to release the load in hot spots and at the same time decrease file query latency. Generally, the methods replicate files near file owners, file requesters or along a query path from a requester to a owner.

[2]PAST, [3]CFS, and Backslash replicate each file on close nodes near the file's owner. Backslash also pushes cache one hop closer to requesters as soon as nodes are overloaded. In LAR and Gnutella, overloaded nodes replicate a file at requesters. Freenet replicates files on the path from a requester to a file owner. [3]CFS, [2] PAST,LAR cache routing hints along the search path of a query.

[4]Cox et al. studied providing DNS service over a P2P network as an alternative to traditional DNS. The caches index entries, which are DNS mappings, along search query paths. Overlook deploys client-access history to place a replica of a popular file on a node with most lookup requests for fast replica location. [21] Less Log determines the replicated nodes by constructing a lookup tree based on IDs to determine the location of the replicated node.

In Ocean Store, files are replicated and stored on multiple servers for security concern without restricting the placement of replicas. Ocean Store maintains two-tier replicas: a small durable primary tier and a large soft-state second tier. Other studies of file replication investigated the relationship between the number of replicas, file query latency, and load balance in unstructured P2P systems. In most of these methods, file owners rigidly determine replica nodes and nodes passively accept replicas. They are unable to keep track replica utilization to reduce underutilized replicas and ensure high utilization of existing replicas. Thus, unnecessary replicas lead to a waste of consistency maintenance.

[5]Yang et al. proposed Parity Replication in IPNetwork Storages (PRINS). PRINS replicates the parity of a data block upon each write operation instead of the data block itself. The data block will be recomputed back at the replica storage site upon receiving the parity. PRINS trades off high-speed computation for communication that is costly distributed storages.

An efficient and adaptive decentralized [6] File replication algorithm in P2P file sharing systems called EAD. In the method, traffic hubs that carry more query load and frequently requesters are chosen as replica nodes.[7]Lv et al. and Cohen and Shenker showed that replicating objects proportionally to their popularity achieves optimal load balance but has varied search latency, while uniform replication has the same average search latency for all files but causes load imbalance.

[8]Tewari and Kleinrock showed that proportional replication can optimize flooding-based search, download time, and workload distribution. They also showed that local storage management algorithms such as Least Recently Used (LRU) automatically achieve near-proportional replication and that the system performance with the replica distribution achieved by LRU is very close to optimal. APRE adaptively expands or contracts the replica set of a file in order to improve the sharing process and achieve a low load distribution among the providers.

The value is increased by an additive amount if the file doesn't change between successive polls

$$TTR = TTR_{old} + \alpha$$

The TTR value is reduced by a multiplicative factor

$$TTR = TTR_{old} / \beta$$

Values that fall outside these bounds are set to

$$TTR = \max(TTR_{min}, \min(TTR_{max}, TTR))$$

TTR_{poll} should be calculated based on the following formula:

$$TTR_{poll} = \begin{cases} T_{query} & TTR \leq T_{query}, \\ TTR & TTR > T_{query} \end{cases}$$

Pseudo-code for the IRM adaptive file

consistency maintenance algorithm

==operation at time instant T_{poll}

if there is a query for the file **then**
include a polling request into the query for file f
else

send out a polling request

if get a validation reply from file owner **then**

{

if file is valid **then**

$$TTR = TTR_{old} + \alpha$$

if file is stale **then** {

$$TTR = TTR_{old} / \beta$$

update file replica

}

if $TTR > TTR_{max}$ or $TTR < TTR_{min}$ **then**

$$TTR = \max(TTR_{min}, \min(TTR_{max}, TTR))$$

if $TTR \leq T_{query}$ **then**

$$TTR_{poll} = T_{query}$$

else

$$TTR_{poll} = TTR_g$$

V. COMPARISON STUDY ABOUT IRM

IRM integrates file replication and consistency maintenance in a harmonized and coordinated manner. File replication helps to minimize the number of replicas in order to minimize the overhead of consistency maintenance. At the same time, consistency maintenance helps to guarantee the fidelity of consistency among replicas in file replication dynamism. This principle helps IRM achieve high efficiency and effectiveness in both file replication and consistency maintenance. The Impact of File Replication on Consistency Maintenance. The Impact of consistency Maintenance on File Replication. IRM minimizes the number of replicas while maintaining high efficiency and effectiveness of file replication. It produces much less replicas than the traditional file replication methods while still keeping high utilization of replicas. This significantly reduces the overhead of replica update in consistency maintenance phase, and hence enhances the scalability and efficiency of P2P file sharing systems.

IRM consistency maintenance is to guarantee that a replica file is up to date when being provided. The query rate is also used for consistency maintenance. Based on the query rate, a replica node can know if its replica should be updated or not.

VI. PROPOSED WORK

IRM associates a time-to-refresh (TTR) value with each replica. The TTR denotes the next time instant a node should poll the owner to keep its replica updated. The TTR value is varied dynamically based on the results of each polling. But in case there is no change in file for more than 5 or 10 TTR, there is a waste of querying the owner and increase the burden of network. messages based on message spreading or a structure without considering file replication dynamism, leading to inefficient file update and hence high possibility of outdated file response.

An Integrated file Replication and consistency Maintenance mechanism (IRM) that integrates the two techniques in a systematic and harmonized manner. It achieves high efficiency in file replication and consistency maintenance at a significantly low cost. It reduces overhead and yields significant improvements on the efficiency of both file replication and consistency maintenance approaches.

REFERENCES

- [1]. H. Shen, "IRM: Integrated File Replication and Consistency Maintenance in P2P Systems," Proc. IEEE 2010.
- [2]. A. Rowstron and P. Druschel, "Storage Management and Caching in PAST, a Large-Scale, Persistent Peer-to-Peer Storage Utility," Proc. ACM Symp. Operating Systems Principles (SOSP), 2001.
- [3]. F. Dabek, M.F. Kaashoek, D. Karger, R. Morris, and I. Stoica, "Wide Area Cooperative Storage with CFS," Proc. ACM Symp. Operating Systems Principles (SOSP), 2001.
- [4]. R. Cox, A. Muthitacharoen, and R.T. Morris, "Serving DNS Using a Peer-to-Peer Lookup Service," Proc. First Int'l Workshop Peer-to-Peer Systems (IPTPS), 2002.
- [5]. Q. Yang, W. Xiao, and J. Ren, "PRINS: Optimizing Performance of Reliable Internet Storages," Proc. 26th Int'l Conf. Distributed Computing Systems (ICDCS), p. 32, 2006.
- [6]. H. Shen, "EAD: An Efficient and Adaptive Decentralized File Replication Algorithm in P2P File Sharing Systems," Proc. Eighth Int'l Conf. Peer-to-Peer Computing (P2P '08), 2008.
- [7]. Q. Lv, P. Cao, E. Cohen, K. Li, and S. Shenker, "Search and Replication in Unstructured Peer-to-Peer Networks," Proc. 16th Int'l Conf. Supercomputing (ICS), 2001.
- [8]. S. Tewari and L. Kleinrock, "On Fairness, Optimal Download Performance and Proportional Replication in Peer-to-Peer Networks," Proc. IFIP Networking, 2005.
- [9]. I. Stoica, R. Morris, D. Liben-Nowell, D.R. Karger, M.F. Kaashoek, F. Dabek, and H. Balakrishnan, "Chord: A Scalable Peer-to-Peer Lookup Protocol for Internet Applications," IEEE/ACM Trans. Networking, vol. 11, no. 1, pp. 17-32, Feb. 2003.
- [10]. S. Ratnasamy, P. Francis, M. Handley, R. Karp, and S. Shenker, "A Scalable Content-Addressable Network," Proc. ACM SIGCOMM, pp. 329-350, 2001.
- [11]. G. Xie, Z. Li, and Z. Li, "Efficient and Scalable Consistency Maintenance for Heterogeneous Peer-to-Peer Systems," IEEE Trans. Parallel and Distributed Systems, vol. 19, no. 12, pp. 1695-1708, Dec. 2008.
- [12]. X. Chen, S. Ren, H. Wang, and X. Zhang, "SCOPE: Scalable Consistency Maintenance in Structured P2P Systems," Proc. IEEE INFOCOM, 2005.
- [13]. P. Druschel, M. Castro, A.-M. Kermarrec, and A. Rowstron, "Scribe: A Large-Scale and Decentralized Application-Level Multicast Infrastructure," IEEE J. Selected Areas in Comm., vol. 20, no. 8, pp. 1489-1499, Oct. 2002.
- [14]. M. Roussopoulos and M. Baker, "CUP: Controlled Update Propagation in Peer to Peer Networks," Proc. USENIX Ann. Technical Conf., 2003.
- [15]. L. Yin and G. Cao, "DUP: Dynamic-Tree Based Update Propagation in Peer-to-Peer Networks," Proc. 21st Int'l Conf. Data Eng. (ICDE), 2005.
- [16]. A. Datta, M. Hauswirth, and K. Aberer, "Updates in Highly Unreliable, Replicated Peer-to-Peer Systems," Proc. 23rd Int'l Conf. Distributed Computing Systems (ICDCS), 2003.
- [17]. I. Clarke, O. Sandberg, B. Wiley, and T.W. Hong, "Freenet: A Distributed Anonymous Information Storage and Retrieval System," Proc. Int'l Workshop Design Issues in Anonymity and Unobservability, pp. 46-66, 2001.
- [18]. J. Lan, X. Liu, P. Shenoy, and K. Ramamritham, "Consistency Maintenance in Peer-to-Peer File Sharing Networks," Proc. Third IEEE Workshop Internet Applications (WIAPP), 2003.
- [19]. M. Theimer and M. Jones, "Overlook: Scalable Name Service on an Overlay Network," Proc. 22nd Int'l Conf. Distributed Computing Systems (ICDCS), 2002.
- [20]. K. Huang, T. Huang, and J. Chou, "LessLog: A Logless File Replication Algorithm for Peer-to-Peer Distributed Systems," Proc. 18th Int'l Parallel and Distributed Processing Symp. (IPDPS), 2004.

Detecting of NH_3 , CO_2 polluted gases by using $\text{ZnO-In}_2\text{O}_3$ thin films

Dr. Shatha Shammon Batros¹, Dr. Ghada Sabah Karam²

¹Ministry of Science and Technology / Baghdad – Iraq

²Al Mustansereya University / Baghdad -Iraq

ABSTRACT

Polycrystalline $\text{ZnO-In}_2\text{O}_3$ thin films for gas sensor were prepared on to glass substrates by using spray pyrolysis method from solution of 0.1 M ZnCl_2 and 0.1M InCl_3 at 300°C temperature and 100 course of spray. A number of techniques including X-ray diffraction (XRD), atomic force microscope (AFM) and scanning electron microscope (SEM) are used to study the morphology of $\text{ZnO-In}_2\text{O}_3$ thin films. Polycrystalline structured of as-obtained films was confirmed by using these techniques. Optical properties, and sensitivity of thin film to NH_3 , CO_2 gases was also studied.

KEYWORDS: Thin films, crystalline structure, $\text{ZnO-In}_2\text{O}_3$ thin films, sensors.

I. INTRODUCTION

Metal oxide thin films like indium oxide and zinc doped indium oxide have unique characteristics such as good conductivity, high optical transmittance over the visible wavelength region, excellent adhesion to substrates and chemical stability and photochemical properties. These properties are resulted from their n-type semiconductor behavior and wide band gaps. Therefore, indium oxide and zinc doped indium oxide are used in a wide range of applications including solar energy conversion and photovoltaic devices, flat panel displays and biocatalytic redox transformation. New applications require IZO films with lower resistivity and higher optical transmissions over the visible wavelength region. In order to obtain optimal characteristic i.e. high transparency and low sheet resistance, the parameters such as thickness of the film, dopant type and its amount and the other deposition conditions have to be optimized. It is well known that the electrical and optical properties of semiconducting oxides like In_2O_3 depend strongly on defect density created by external doping or disturbed stoichiometry as well as their preparation and growth conditions [1-5].

However, high cost of In_2O_3 has motivated efforts to develop substitutes. Recently, zinc oxide (ZnO) is a promising material in the above applications. It has a great interest in wide band gap semiconductors, because of the ever increasing commercial desire for short wavelength light emitting devices. As a good candidate, ZnO nano structured films have wide band gap (3.37 eV) [6] at room temperature (RT). The efficiency and performance of any optical and electrical nano devices are directly determined by the properties of underlying nanostructures, which are in turn greatly dependent on the crystallographic orientation, size, shape, and morphology. A highly transparent ZnO films have been prepared by many different deposition techniques and their corresponding deposition parameters play an important role in controlling the morphology and physical properties of the nanostructures. Both physical deposition, including thermal evaporation, sputtering, spray pyrolysis, metal organic chemical vapor deposition (MOCVD), pulsed laser deposition, molecular beam epitaxy (MBE) [7-15], and chemical synthetic routes, including hydro thermal, sol-gel, electrochemical, chemical bath deposition [16-26] have been successfully employed to prepare a wide variety of ZnO nanostructures.

Spray pyrolysis technology is a convenient for the deposition of semiconductor thin films and has the several advantages in comparison with other deposition techniques such as low cost of the source materials, producing high quality films using comparatively simple deposition equipment, moderate substrate temperatures, deposition scaled for large area and uniform deposition with very thin layers with specific composition, morphology, good adhesion between the deposited film and controlling the shape and sizes. The morphology of the material depends on the thermal treatment [27].

Gas sensor play vital role in detecting, monitoring and controlling the presence of hazardous and poisonous gases in the atmosphere at very low concentrations. Semiconductor gas sensors in the form of thin films are highly sensitive and reliable, having a performance/price ratio comparable to that of microelectronic components [28].

In the present investigation, pyrolysis methods has been used to prepared a polycrystalline $\text{ZnO-In}_2\text{O}_3$ thin films, the structural characterization from XRD, SEM and AFM were studied. Optical properties, and Sensing properties also was calculated for NH_3 , CO_2 gas.

II-EXPEREMENTAL

Chemical spray pyrolysis is one of the major techniques used to deposit a wide variety of materials including metal or alloy oxides. Generally, spray pyrolysis deposition system which is mainly consists of the following four sections: (a) the reactants and carrier gas assembly connected to the spray nozzle at the entrance of the reaction chamber, (b) the reaction chamber in which there is a resistive heater used to heat the substrate to the required temperature for thin film deposition, (c) the temperature controller that monitors the deposition temperature and controls the desired substrate temperature and (d) the exhausting gas module, as it shown in figure (1). The substrate temperature was measured using a K-type thermocouple to an accuracy of ± 1 K. The film were prepared on clean glass substrates, the slides first cleaned in distilled water in order to remove the impurities and residuals from their surfaces, followed by rinsing in chromatic acid (for two day), to introduce functional groups called nucleation and /or epitaxial centers, which formed the basis for layer films growth. Then the samples were washed repeatedly in deionized water, and finally put in ultrasonic agitation with distilled water for 15 min then dried. The solution used for the preparation the films investigated here had the following amounts: the mixture of 1.1425 gm of ZnCl_2 and 0.88212 gm of InCl_3 at (50:50) molar ratio, at molarities 0.1M for both solutions. The glass substrate temperature was 300°C . The atomization of the solution into a spray of fine droplets was carried out by the spray nozzle with 1 mm inner diameter, with the help of compressed air as carrier gas. During the course of spray (100 course), the substrate temperature was monitored using a thermocouple with the help of digital millimeter. The slides then were placed on the surface of a substrate heater when sprayed. The nozzle-to-substrate distance was 25 cm.

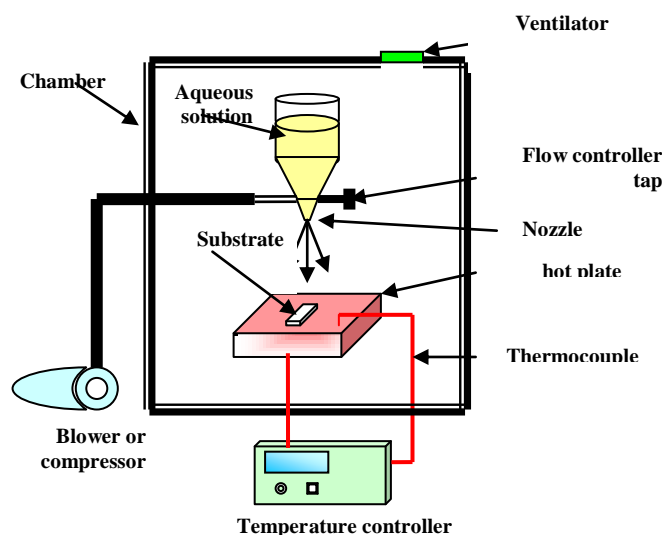


Figure (1): Spray Pyrolysis System

III- RESULTS AND DISCUSSION

3.1 The structure and morphology of films :

Typical XRD pattern for $\text{ZnO-In}_2\text{O}_3$ films prepared by pyrolysis method is presented as in figure (2). As exhibited in figure (2) the films show a crystalline structure. Diffraction peaks at $2\theta = 31.592^\circ$ and 34.357° were assigned to hexagonal ZnO planes (100) and (002) respectively) based on comparison with JCPDS standard [28]. In the same pattern can be observed at $2\theta = 35.981^\circ$ and, the reflection of (400) planes of In_2O_3 cubic structure [29], this results are the same with the other research [28,30]. Table (1) refers to the structural parameters to the prepared samples.

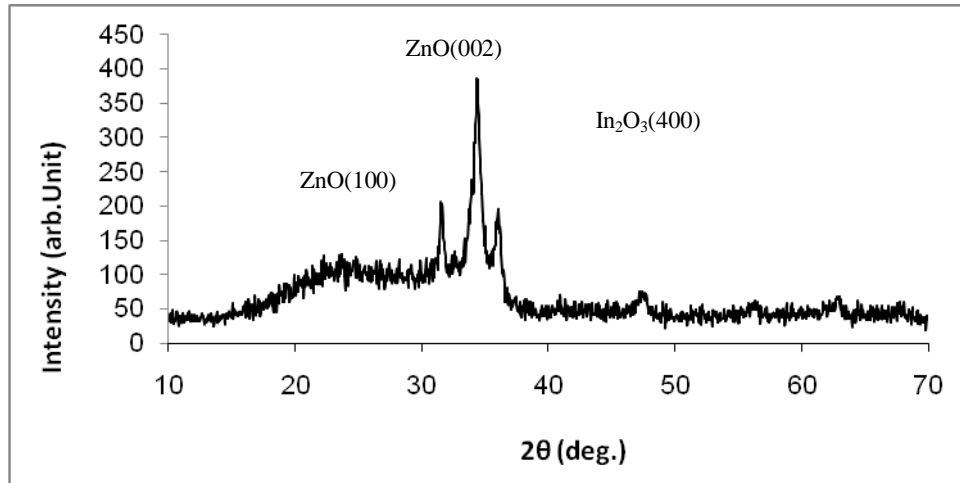


Figure (2) XRD pattern of ZnO-In₂O₃ sample prepared by pyrolysis method

Table (1): Values of some structure parameters of ZnO-In₂O₃ thin film

Sample	2Theta(deg)	d(A°)	hkl	FWHM
ZnO	31.592	2.82977	100	0.6154
ZnO	34.357	2.60807	002	0.8504
In ₂ O ₃	35.981	2.49499	400	0.7889

From the XRD patterns it is possible to evaluate the average grain size (D) of the ZnO-In₂O₃ thin films by using the Well-known Deby- Scherer's formula [31].

$$D=K\lambda/\beta\cos\theta,.....(1)$$

Where, the constant K is a constant of the order unity, λ is the wavelength of X-rays (1.4506A°) for CuK_α, θ is the Bragg's angle and β is the full width at half maximum. The dislocation density (δ) has been evaluated from Williamson and Smallman's formula [31].

$$\delta=1/D^2 \text{ lines /m}^2.....(2)$$

The micro strain (ε) is obtained using the relation [31].

$$\epsilon=\beta \cos \theta/4.....(3)$$

All these parameters are calculated and presented in Table 2.

Table (2) structural parameters of ZnO-In₂O₃ thin films

Samples	Grain Size (D)X10 nm	Density (δ) x10 ¹⁵ Lines/m ²	Micro strain (ε) x10 ⁻³
ZnO (100)	14.010	5.094	2.589
ZnO (002)	10.209	9.594	3.554
In ₂ O ₃ (400)	11,059	9.594	3.278

The surface morphology of the thin films was also investigated. SEM and AFM characteristic photographs are shown in figure (3) and (4).

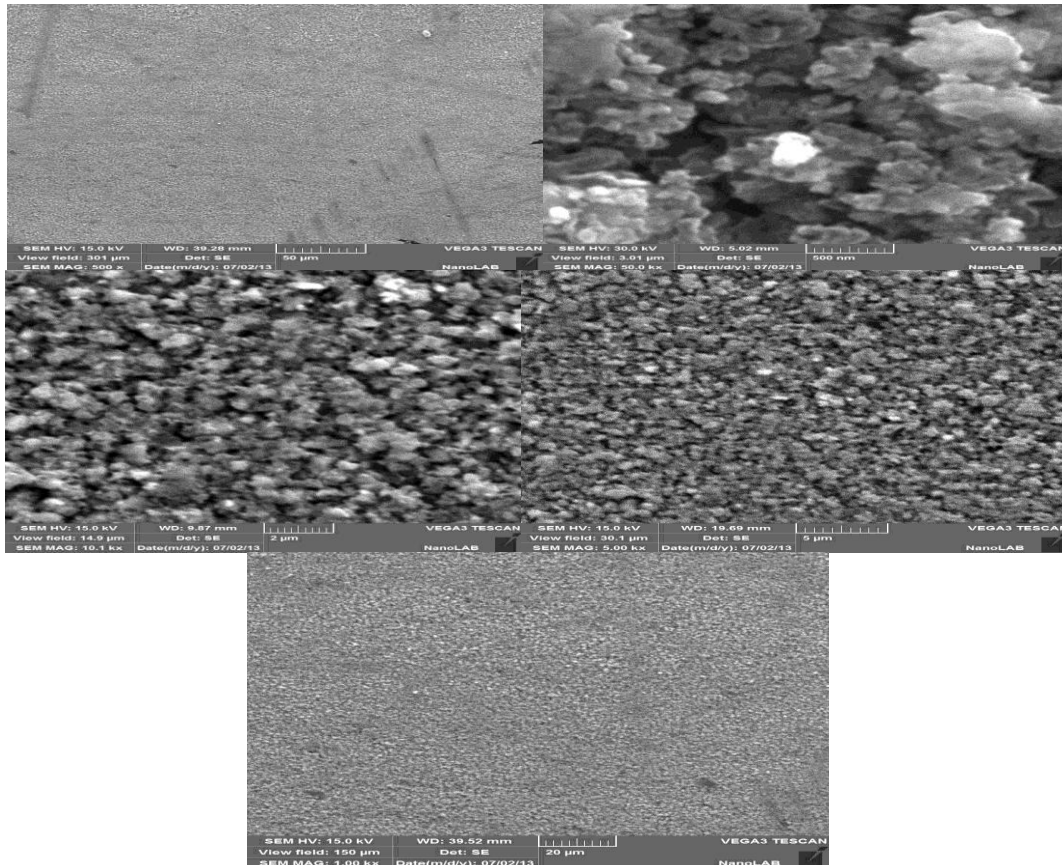
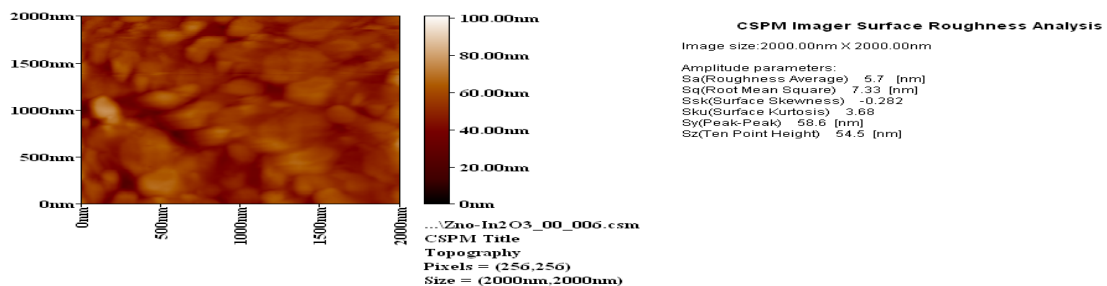


Figure (3) SEM micrographs characteristic of $\text{ZnO-In}_2\text{O}_3$ thin film

From figure (3), the SEM micrograph of as-deposited film shows uniform deposition over the substrate well. SEM characteristic micrograph, given the extremely small crystallite size, few tens or even few hundred nm and reveals that the ZnO film consists of round shape particles. In figure (4), a typical $2 \times 2 \mu\text{m}^2$ sized AFM image of $\text{ZnO-In}_2\text{O}_3$ film surface is shown. The film crystallites are well shape and uniform in size. It was observed, from 3D image that, the films exhibit a surface columnar morphology, which can be a consequence of crystalline preferential orientation. The film roughness was 5.7 nm. AFM images indicate that the used preparation conditions of the films are more favorable to obtain sample with excellent surface morphology. All used investigation techniques reveal the polycrystalline structure of the obtained films.



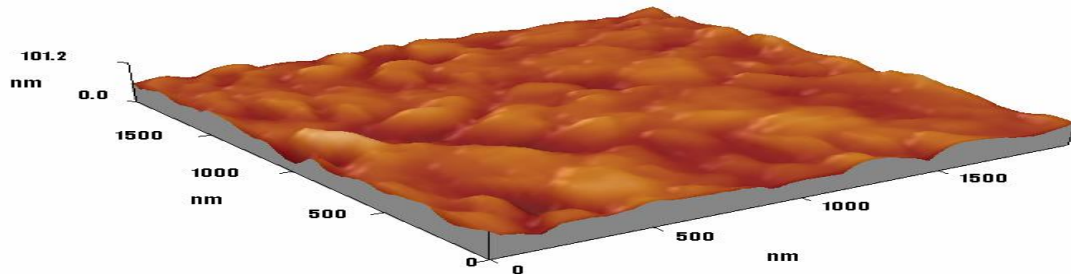


Figure (4) AFM micrographs characteristic of ZnO- In_2O_3 thin film

3.2 Optical properties

The optical properties of a material provide information about the electronic band structures, localized states and the nature (types) of optical transitions, the optical properties are very important for the understanding of the materials. Figure (5) shows the combination of optical absorbance spectra for ZnO- In_2O_3 thin film . The spectra of the deposited thin film was measured using UV-VIS spectrum (Optima Sp – 300 Plus) in the wavelength region of 305-900 nm.

Figure (6), show the variation between absorption coefficients (α) with wavelength. The $(\alpha hv)^2$ versus hv for optical band gap of the ZnO- In_2O_3 thin film was studied. The optical band gap values have been determined by the extrapolation of the linear portion on the energy axis. The value of the optical band was 3.11 eV as it shown in figure (7).

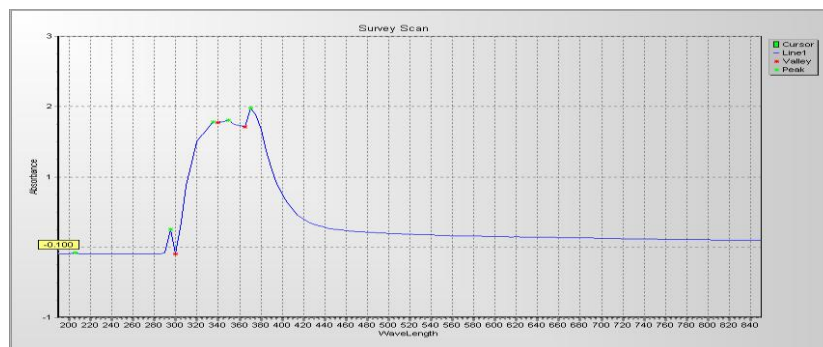


Figure (5) Typical optical absorption spectra for ZnO- In_2O_3 thin film

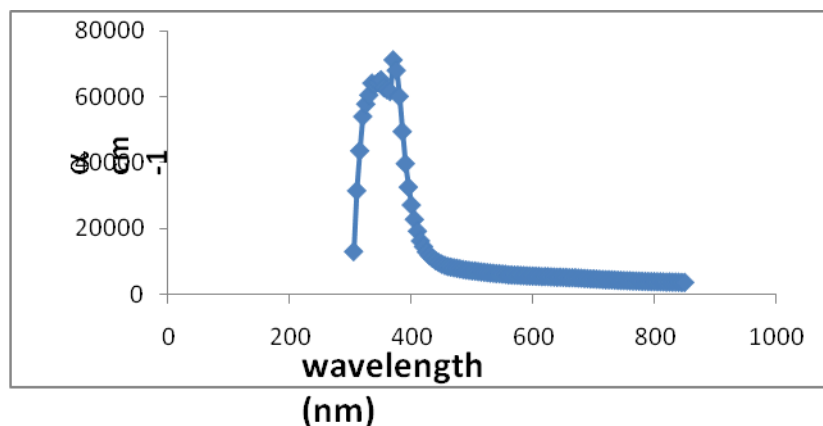


Figure (6) Plot of α versus wavelength curve of ZnO- In_2O_3 thin film

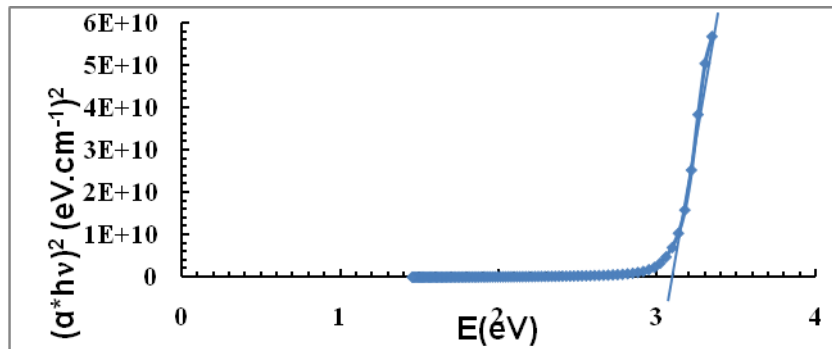


Figure (7) Plot of $(\alpha hv)^2$ versus (hv) curve of ZnO -In₂O₃ thin film

3.3 Response to gases vapor

The experimental arrangement for sensitivity measurement for NH₃, CO₂ gases vapor is shown in figure (8). Nitrogen gas was purged for 20 min to clean the sample environment, examined gases (NH₃, CO₂) was injected by micro-syringe into test chamber and sensing characteristics of the sensor was then observed. The change in electrical resistance of a sensor was measured by electrometer. The time taken by the sensor for all of resistance was considered as response time of a sensor. The ratio of measured resistance before and after exposing the sample surface to gas vapor gives the value of sensitivity [26], as it calculated from the equation (4). Figure (9) shows the sensitivity of the sensor to gases.

$$S = \left| \frac{R_{(air)} - R_{(gas)}}{R_{(air)}} \right| \dots\dots\dots(4)$$

The sensing properties were studied at low concentrations (9 ppm) of gases vapor. The optioned results in pyrolysis methods are promising for the preparation of sensitive and low cost gas sensor operating in room temperatures. It can be fabricating sensor to detect variety of gases.



Figure (8) Experimental arrangement system for gas detecting

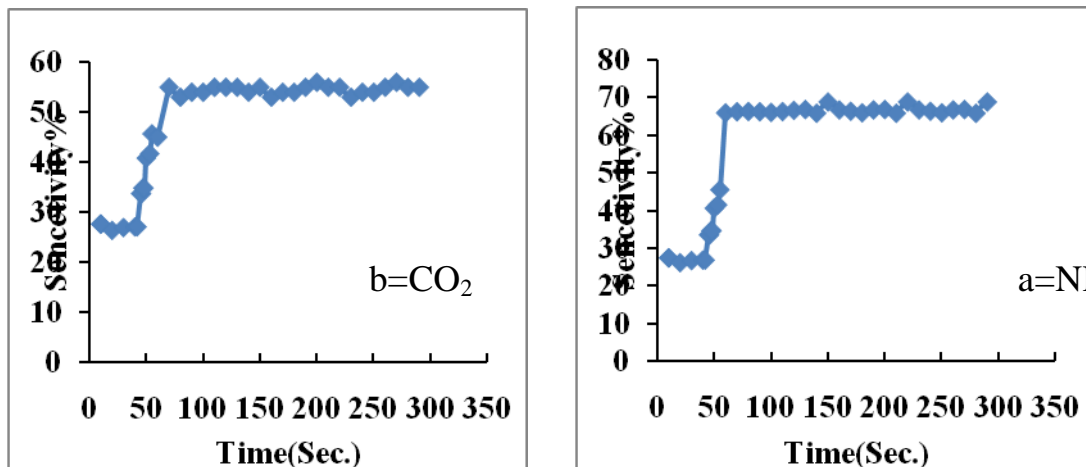


Figure (9:a,b) Sensitivity vs. time of ZnO-In₂O₃ thin film to NH₃, CO₂ gases**IV- CONCLUSION**

Polycrystalline ZnO-In₂O₃ thin film sensor for NH₃, CO₂ gases has been prepared in pyrolysis method successfully. The films have been characterized by x-ray diffraction, SEM microscopic and AFM microscopic. From the optical properties of thin films we observe the optical gap which is about 3.11eV. The sensitivity of the sensor to NH₃, CO₂ has been obtained at room temperature. The ratio of sensitivity of NH₃ is better than CO₂ vapor. This result obtained in pyrolysis methods are promising for the preparation of sensitive and low cost NH₃, CO₂ sensor operating in room temperatures.

REFERENCES

- [1] M. Wirtz J. Kluczik, M. Rivera, J. Am. Chem. Soc. 2000, 122, 1047–1056.
- [2] C. A. Martinez, J. D. Stewart, Curr. Org. Chem. 2000, 4, 263–268.
- [3] C. G. Granquist, Appl. A: Solids Surf. 1993, 57, 19–22.
- [4] G. Haacke, J. Appl. Phys. 1976, 47, 4086–4089.
- [5] C. Liu, T. Matsutani, N. Yamamoto, M. Kiuchi, Europhys. Lett. 2002, 59, 606–610.
- [6] Y. Zhizhen, M. Dewei, H. Junhui, J Crystal Growth 2003, 256, 78.
- [7] Debabrata Pradhan, Shrey Sindhwani, K. T. Leung, Nanos-scale Res Lett 2010, 5, 1727.
- [8] P. Puspharajah, S. Radhakrishna, J Mater Sci 1997, 32, 3001.
- [9] G. Zhang, M. Adachi, S. Ganjil, A. Nakamura, J. Temmyo, Y. Matsui, Jpn. J. Appl. Phys. Part 2, 2007, 46, L730.
- [10] C. Gorla, N. Emanetoglu, S. Liang, W. Mayo, Y. Lu, M. Wraback, H. Shen, J Appl Phys 2000,85, 2595.
- [11] B. Sang, K. Kushiya, D. Okumura, O. Yamase, Sol Energy Mater Sol Cells 2001, 67, 237.
- [12] M. Lorenz, E.M. Kaidashev, A. Rahm, Th. Nobis, J. Lenzner, G. Wagner, D. Spemann, H. Hochmuth, M. Grundmann, Appl. Phys. Lett. 2005, 86, 143113.
- [13] YR. Ryu, S. Zhu, JD. Budai, HR. Chandrasekhar, PF. Miceli, HW. White, Appl Phys Lett 2000, 88, 201.
- [14] Y. Segawa, A. Ohtomo, M. Koinuma, ZK. Tang, P. Yu, GKL. Wong, Phys Stat Sol (b) 1997,202, 669.
- [15] HB. Kang, K. Nakamara, SH. Lim, D. Shindo, Jpn J Appl Phys. 1998, 37, 781.
- [16] C. Wang, B. Mao, E. Wang, Z. Kang, C. Tian, Solid State Commun. 2007, 141, 620.
- [17] B. Liu, H.C. Zeng, Chem Mater 2007, 19, 5824.
- [18] Y. Sun, N. George Ndifor-Angwafor, D.J. Riley, M.N.R. Ashfold, Chem. Phys. Lett. 2006, 431, 352.
- [19] S. Kar, A. Dev, S. Chaudhuri, J. Phys. Chem. B 2006, 110, 17848.
- [20] S.K.N. Ayudhya, P. Tonto, O. Mekasuwandumrong, V. Pa-varajarn, P. Prasertthdam, Cryst. Growth Des. 2006, 6, 2446.
- [21] C.V. Santilli, S.H. Pulcinelli, M.S. Tokumoto, V. Briosis, J. Eur. Ceramic Soc. 2007, 27, 3691.
- [22] P. Bhattacharyya, P.K. Basu, H. Saha, S. Basu, Sens. Actua-tors B Chem. B 2007,124, 62.
- [23] S. Peulon, D. Lincot, Adv. Mater. 1996, 8, 166.
- [24] W. Peng, S. Qu, G. Cong, Z. Wang, Cryst. Growth Des. 2006, 6, 1518.
- [25] B. Cao and W. Cai, J. Phys. Chem. C 2008,112, 680.
- [26] L. Znaidi, GJAA. Soler Illia, S. Benyahia, C. Sanchez, AV. Kanaev, Thin Solid Films, 2003, 428, 257.
- [27] Li Wang, Yong Pu, Wenqing Fang, Jiangnan Dai, Changda Zheng, Chunlan Mo, Chuanbin Xiong and Fengyi Jiang, Thin Solid Films, 2005,491, 323.
- [28] K K Makhija, Arabinda Ray, R M Patel U B Trivedi And H N Kapse, Bell . Mater, Sci., vol 28, no.1 2005, pp. 9-17.
- [29] ICDD 1997 JCPDS International center for diffraction data A rights reserved PCPDFWIN v.1.30.
- [30] R. Sarhaddi, N. Shahtahmasebi, M. Rezaee Rohn-Abadi, M.M. Bagheri-Mohagheghi, "Effect of post-annealing temperature on nano-structure and energyband gap of indium tin oxide (ITO) nano-particles synthesized by polymerizing-complexing sol-gel method" .. physics E 43,(2010), 452-457
- [31]. K.Girija, S.Thirumalairajan, S.M.Mohan, J.Chandrasekaran, "Structural, Morphological And Optical Studies Of Cdse Thin Films From Ammonia Bath", Chalocogenide Letters Vol.6.No.8, August 2009, p.351-357.

Implementation of Elliptic Curve Digital Signature Algorithm Using Variable Text Based Message Encryption with Message Digest

Rajasekhar Bandapalle Mulinti^{1,2} Dr.G.A.Ramachandra

^{1,2} Research Scholar, Department of Computer Science & Technology, ^{1,2} Associate Professor, Sri Krishnadevaraya University, INDIA

ABSTRACT:

Digital Signatures are considered as digital counterparts to handwritten signatures, and they are the basis for validating the authenticity of a connection. It is well known that with the help of digital signature, forgery of digital information can be identified and it is widely used in e-commerce and banking applications. Elliptic curve digital signatures (ECDSA) are stronger and ideal for constrained environments like smart cards due to smaller bit size, thereby reducing processing overhead. We have implemented ECDSA over Elliptic Curve (EC) P-192 and P-256 using various Text Message encryptions which are Variable Size Text Message (VTM), Fixed Size Text Message (FTM) and Text Based Message (TBM) encryption methods and compared their performance. In the existing Variable Text Based Message used the plain message for generating digital signature but in the new approach, we have converted plain message to digested message using SHA algorithm and then created digital signature which is more faster than existing approach.

Keywords: Digital Signature, Elliptic Curve Digital Signature Algorithm, Elliptic Curve Cryptography, ECDLP.

I. Introduction

Cryptography is the branch of cryptology dealing with the design of algorithms for encryption and decryption, intended to ensure the secrecy and/or authenticity of message. The Digital Signature Algorithm (DSA) was proposed in August 1991 by the U.S. National Institute of Standards and Technology (NIST). Digital signature authentication schemes provide secure communication with minimum computational cost for real time applications, such as electronic commerce, electronic voting, etc. The sender generates the signature of a given message using his secret key; the receiver then verifies the signature by using sender's public key. The ECDSA have a smaller key size, which leads to faster computation time and reduction in processing power, storage space and bandwidth. This makes the ECDSA ideal for constrained devices such as pagers, cellular phones and smart cards. The Elliptic-Curve Digital Signature Algorithm (ECDSA) is a Digital Signature Scheme based on ECC. ECDSA was first proposed in 1992 by Scott Vanstone in response of NIST (Nation Institute of Standards and Technology) request for public comments on their proposal for Digital Signature Schemes[1].

Digital Signature authenticated schemes, have the following properties.

1. **Confidentiality.** Secret information shared between sender and receiver; any outsider cannot read the information.
2. **Authentication.** The sender imprints his identity by means of the digital signature, which only the designated receiver can unravel and verify. An anonymous adversary cannot send a malicious message impersonating the genuine sender, because he does not have the necessary tools to generate the signature.
3. **Non-repudiation.** The signature firmly establishes the identity of the sender. The sender cannot deny having sent the message and the signature.

In this paper we discuss ECC in detail and ECDSA Implementation with different Text Message encryption methods and compared the results.

II. Elliptic Curve Discrete Logarithm Problem

An elliptic curve E , [2] defined over a field K of characteristic $\neq 2$ or 3 is the set of solutions $(x, y) \in K'$ to the equation $y^2 = x^3 + ax + b$ (1)

$a, b \in K$ (where the cubic on the right has no multiple roots). Two nonnegative integers, a and b , less than p that satisfy:

$$4a^3 + 27b^2 \pmod{p} = 0 \quad (2)$$

Then $E_p(a, b)$ denotes the elliptic group mod p whose elements (x, y) are pairs of nonnegative integers less than p satisfying:

$$y^2 = x^3 + ax + b \pmod{p} \quad (3)$$

together with the point at infinity O .

The elliptic curve discrete logarithm problem (ECDLP) can be stated as follows. Fix a prime p and an elliptic curve.

$$Q = xP \quad (4)$$

where xP represents the point P on elliptic curve added to itself x times. Then the elliptic curve discrete logarithm problem is to determine x given P and Q . It is relatively easy to calculate Q given x and P , but it is very hard to determine x given Q and P .

ECC is based on ECDLP. ECDH and ECDSA are cryptographic schemes based on ECC. The best known algorithm for solving ECDLP is Pollard-Rho algorithm which is fully exponential having a running time of $\sqrt{(\Pi*n/2)}$.

III. Elliptic Curve Cryptography

The Elliptic curve cryptosystems (ECC) were invented by Neal Koblitz [2] and Victor Miller[3] in 1985. They can be viewed as elliptic curve analogues of the older discrete logarithm (DL) cryptosystems in which the subgroup of Z_p^* is replaced by the group of points on an elliptic curve over a finite field. The mathematical basis for the security of elliptic curve cryptosystems is the computational intractability of the elliptic curve discrete logarithm problem (ECDLP) [4].

ECC is a relative of discrete logarithm cryptography. An elliptic curve E over Z_p as in Figure 1 is defined in the

Cartesian coordinate system by an equation of the form:

$$y^2 = x^3 + ax + b \quad (5)$$

where $a, b \in Z_p$, and $4a^3 + 27b^2 \pmod{p} \neq 0 \pmod{p}$, together with a special point O , called the point at infinity. The set

$E(Z_p)$ consists of all points (x, y) , $x \in Z_p$, $y \in Z_p$, which satisfy the defining equation, together with O .

Each value of a and b gives a different elliptic curve. The public key is a point on the curve and the private key is a random

number. The public key is obtained by multiplying the private key with a generator point G in the curve.

The definition of groups and finite fields, which are fundamental for the construction of elliptic curve cryptosystem are discussed in next subsections.

3.1. Groups

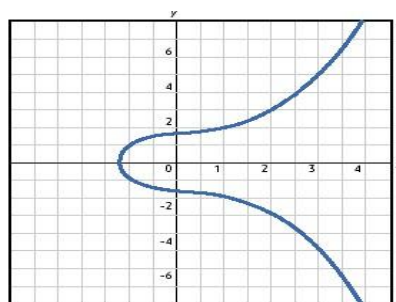


Figure 1. An Elliptic Curve

A group with an operation $*$ is defined on pairs of elements of G . The operations satisfy the following properties:

- Closure: $a * b \in G$ for all $a, b \in G$
- Associativity: $a * (b * c) = (a * b) * c$ for all $a, b, c \in G$
- Existence of Identity: There exists an element $e \in G$, called the identity, such that $e * a = a * e = a$ for all $a \in G$.
- Existence of Inverse: For each $a \in G$ there is an element $b \in G$ such that $a * b = b * a = e$. The element b is called the inverse of a .

Moreover, a group G is said to be abelian if $a * b = b * a$ for all $a, b \in G$. The order of a group G is the number of elements in G .

3.2. Finite Field

A finite field consists of a finite set of elements together with two binary operations called addition and multiplication, which satisfy certain arithmetic properties. The order of a finite field is the number of elements in the field. There exists a finite field of order q if and only if q is a prime power. If q is a prime power, then there is essentially only one finite field of order q ; this field is denoted by F_q . There are, however, many ways of representing the elements of F_q . Some representations may lead to more efficient implementations of the field arithmetic in hardware or in software. If $q = p^m$ where p is a prime and m is a positive integer, then p is called the characteristic of F_q and m is called the extension degree of F_q .

3.2.1. Prime Field F_p

Let p be a prime number. The finite field F_p called a prime field, is comprised of the set of integers $\{0, 1, 2, \dots, p-1\}$ with the following arithmetic operations:

- Addition: If $a, b \in F_p$ then $a + b = r$, where r is the remainder when $a + b$ is divided by p and $0 \leq r \leq p-1$ known as addition modulo p .
- Multiplication: If $a, b \in F_p$ then $a \cdot b = s$, where s is the remainder when $a \cdot b$ is divided by p and $0 \leq s \leq p-1$ known as multiplication modulo p .
- Inversion: If a is non-zero element in F_p , the inverse of modulo a modulo p , denoted by a^{-1} , is the unique integer $c \in F_p$ for which $a \cdot c = 1$.

3.2.2. Binary Field F_2^m

The field F_2^m , called a characteristic two finite field or a binary finite field, can be viewed as a vector space of dimension m over the field F_2 which consists of the two elements 0 and 1. That is, there exist m elements $\alpha_0, \alpha_1, \dots, \alpha_{m-1}$ in F_2^m such that each element α can be uniquely written in the form:

$$\alpha = a_0 \alpha_0 + a_1 \alpha_1 + \dots + a_{m-1} \alpha_{m-1}, \text{ where } a_i \in \{0, 1\}$$

Such a set $\{\alpha_0, \alpha_1, \dots, \alpha_{m-1}\}$ is called a basis of F_2^m over F_2 . Given such a basis, a field element α can be represented as the bit string $(a_0 + a_1 \dots + a_{m-1})$. Addition of field elements is performed by bitwise XOR-ing the vector representations. The multiplication rule depends on the basis selected. ANSI X9.62 permits two kinds of bases: polynomial bases and normal bases.

3.2.3. Domain Parameters

The domain parameters for ECDSA consist of a suitably chosen elliptic curve E defined over a finite field F_q of characteristic p , and a base point $G \in E(F_q)$. Domain parameters may either be shared by a group of entities, or specific to a single user. To summarize, domain parameters are comprised of:

1. A field size q , where either $q = p$, an odd prime, or $q = 2^m$
2. An indication FR (field representation) of the representation used for the elements of F_q
3. (optional) a bit string seed E of length at least 160 bits
4. Two field elements a and b in F_q which define the equation of the elliptic curve E over F_q (i.e., $y^2 = x^3 + ax + b$ in the case $p > 3$, and $y^2 + xy = x^3 + ax + b$ in the case $p = 2$)
5. Two field elements x_G and y_G in F_q which define a finite point $G = (x_G, y_G)$ of prime order in $E(F_q)$
6. The order of the point G , with $n > 2^{160}$ and $n > 4\sqrt{q}$ and
7. The cofactor $h = \#E(F_q)/n$

3.3. Elliptic Curve Operations over Finite Fields[8]

The main operation is Point multiplication is achieved by two basic elliptic curve operations.

- i. Point addition, adding two points P and Q to obtain another point R i.e. $R = P + Q$.
- ii. Point doubling, adding a point P to itself to obtain another point R i.e. $R = 2P$.

3.3.1. Point Addition

Point addition is the addition of two points P and Q on an elliptic curve to obtain another point R on the same elliptic curve.

Consider two points P and Q on an elliptic curve as shown in Figure 2. If $P \neq -Q$ then a line drawn through the points P and Q will intersect the elliptic curve at exactly one more point $-R$. The reflection of the point $-R$ with respect to x-axis gives the point R, which is the result of addition of points P and Q. Thus on an elliptic curve $R = P + Q$. If $Q = -P$ the line through this point intersect at a point at infinity O. Hence $P + (-P) = O$. A negative of a point is the reflection of that point with respect to x-axis.

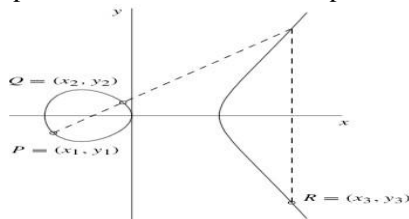


Figure 2: Point Addition

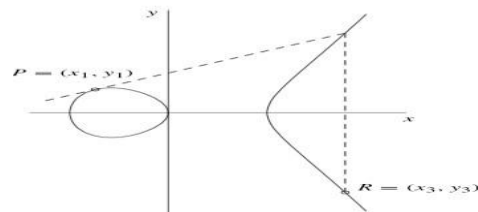


Figure 3: Point Doubling

3.3.2. Point Doubling

Point doubling is the addition of a point P on the elliptic curve to itself to obtain another point R on the same elliptic curve

To double a point J to get L, i.e. to find $R = 2P$, consider a point P on an elliptic curve as shown in Figure 3. If y coordinate of the point P is not zero then the tangent line at P will intersect the elliptic curve at exactly one more point $-R$. The reflection of the point $-R$ with respect to x-axis gives the point R, which is the result of doubling the point P, i.e., $R = 2P$. If y coordinate of the point P is zero then the tangent at this point intersects at a point at infinity O. Hence $2P = O$ when $y_j = 0$. Figure 3 shows point doubling.

3.3.3. Algebraic Formulae over F_p

Let p be a prime in F_p and $a, b \in F_p$ such that $4a^3 + 27b^2 \neq 0 \pmod p$ in F_p , then an elliptic curve E (F_p) is defined as $E(F_p) := \{ p(x, y), x, y \in F_p \}$ Such that $y^2 = x^3 + ax + b \pmod p$ together with a point O, called the point at infinity. Below is the definition of addition of points P and Q on the elliptic curve E (F_p). Let $P(x_1, y_1)$ and $Q(x_2, y_2)$ then

$$R = P + Q = \begin{cases} (x_3, y_3) & \text{if } x_1 = x_2 \text{ and } y_2 = -y_1 \\ Q = Q + P & \text{if } P = O \\ \text{otherwise} & \end{cases}$$

$$\text{Where } x_3 = \begin{cases} \lambda^2 - x_1 - x_2 & \text{if } P \neq \pm Q \text{ (Point Addition)} \\ \lambda^2 - 2x_1 & \text{if } P = Q \text{ (Point Doubling)} \end{cases}$$

$$y_3 = \lambda(x_1 - x_3) - y_1, \text{ and}$$

$$\lambda = \begin{cases} \frac{y_2 - y_1}{x_2 - x_1} & \text{if } P \neq \pm Q \text{ (Point Addition)} \\ \frac{3x_1^2 + a}{2y_1} & \text{if } P = Q \text{ (Point Doubling)} \end{cases}$$

The point $p(x, -y)$ is said to be the negation of $p(x, y)$.

3.3.4. Algebraic Formulae over F^m

Denote the (non-super singular) elliptic curve over F_2^m by $E(F_2^m)$. If $a, b \in F_2^m$ such that $b \neq 0$ then $E(F_2^m) = \{p(x, y), x, y \in F_2^m\}$ together with a point O , called the point at infinity. The addition of points on $E(F_2^m)$ is given as follows: Let $P(x_1, y_1)$ and $Q(x_2, y_2)$ be points on the elliptic curve $E(F_2^m)$, then

$$R = P+Q = \begin{cases} O & \text{If } x_1 = x_2 \text{ and } y_2 = -y_1 \\ Q = Q+P & \text{If } P = O(x_3, y_3) \text{ otherwise} \end{cases}$$

Where $x_3 =$

$$\lambda^2 + \lambda + x_2 + x_1 + a \quad \text{If } P \neq \pm Q \text{ (Point Addition)}$$

$$\lambda^2 + \lambda + a \quad \text{If } P = Q \text{ (Point Doubling)}$$

$$y_3 = \lambda(x_1 + x_3) + x_3 + y_1 \quad \text{and}$$

$$\begin{cases} y_2 + y_1 \\ x_2 + x_1 \\ \lambda = \\ x_1 - x_1 \\ y_1 \end{cases} \begin{cases} \text{If } P \neq \pm Q \text{ (Point Addition)} \\ \text{If } P = \pm Q \text{ (Point Doubling)} \end{cases}$$

IV. Implementation

This paper presents VTM Encryption, VTM decryption [5], ECDSA key generation, signature generation and signature

verification algorithms [8] and ECDSA was implemented over Elliptic Curve (EC) P-192 and P-256 using Text Message

Encryption methods which are VTM [5], FTM[5] and TBM [6] encryption methods and compared their performance.

Algorithm-1

VTM Encryption Algorithm[5]

NOTATION: TM - Text message

M - Message units VS - variable size IV - Initial Vector

k - Auxiliary base parameter

XRM - XORed message

Block – a word with followed space

INPUT: sextuple $T = (p, a, b, G, n, h)$, Digest Message

OUTPUT: Encrypted Message

Begin

$n = \text{wordCount}(\text{DM})$

for $i = 1$ to n **do**

$\text{XRM} = \text{IV} \oplus \text{Block}[i]$ $M = \text{ASCII}(\text{XRM})$

for $j = 0$ to $k-1$ **do**

let $x_j = M * K + j \text{ mod } p$

3

if $z_j = x_j$
break

end if end for

if $j < k$ **then**

$+ x_j + b$ has a square root mod p **then**

```
compute  $y_j$  a square root of  $z_j \pmod p$  map  $M$  to  $(x_j, y_j)$ 
else
output "unsuccessful in attempt to map  $M$  to an EC point"
end if
 $C_m[i] = \{ kG, P_m + kP_B \}$   $IV = XRM$ 
end for
End
```

Algorithm-2

VTM Decryption Algorithm[5]

INPUT: sextuple $T = (p, a, b, G, n, h)$, Encrypted Message

OUTPUT: Decrypted/Plain Digest Message

Begin

```
for  $i = 1$  to  $n$  do //where  $n$  is number of cipher texts
 $P_m(x, y) = P_m + K(nBG) - nB(kG)$  //  $nB$  receivers private key
 $M = x/k$ 
 $D_m = \text{Text}(M)$  //  $M$  is decimal value of base 256 format
 $TM[i] = D_m \oplus IV$   $IV = D_m$ 
 $TM = TM || TM[i]$ 
end for
End
```

Algorithm-3

ECDSA Key pair generation Algorithm[8]

INPUT: Domain parameters $D = (q, FR, a, b, G, n, h)$.

OUTPUT: Public key Q , private key d .

Select $d \in [1, \dots, n-1]$ Compute $Q = dG$ Return (Q, d)

Algorithm-4

ECDSA Signature Generation Algorithm[8]

INPUT: Domain parameters $D = (q, FR, a, b, G, n, h)$, private key d , Encrypted message m' .

OUTPUT: Signature (r, s)

begin repeat

$k = \text{Random}[1, \dots, n-1]$ // select random value

$r = x\text{-coord}([k]G) \pmod n$ $e = H(m')$

$s = k^{-1}(e + dr) \pmod n$

until $r \neq 0$ and $s \neq 0$

return (r, s) .

end

Algorithm-5

ECDSA Signature Verification Algorithm[8]

INPUT: Domain parameters $D = (q, FR, a, b, G, n, h)$, public key Q , Encrypted Message m' , Signature (r, s) .

OUTPUT: Acceptance or rejection of the signature.

begin

if $r, s \notin [1, \dots, n]$ **then**

Return ("Reject the signature")

```

end if
e = H(m')
w = s-1 mod n u1 = ew mod n u2 = rw mod n

x = u1G + u2Q
if x = ∞ then
Return ("Reject the signature")
end if
v = x-coord( X ) mod n
if v = r then
Return ("Accept the signature")
else
Return ("Reject the signature")
end if
end.

```

Elliptic Curve based Signature Generation & Signature Verification processes are described below and the same is represented in graphical format in figure 4 and figure 5.

Signature Generation steps:

1. Digest the plain message using SHA algorithm.
2. Encrypt the message using EC Encryption algorithm which is VTM/FTM/TBM
3. Compute signature for Encrypted message using Algorithm-4
3. Send the digitally signed message

Signature Verification Steps:

1. Verify Signature using Algorithm-5.
2. If verification fails then reject the signature
3. If verification success, then decrypt the message using respective EC Decryption Algorithm.

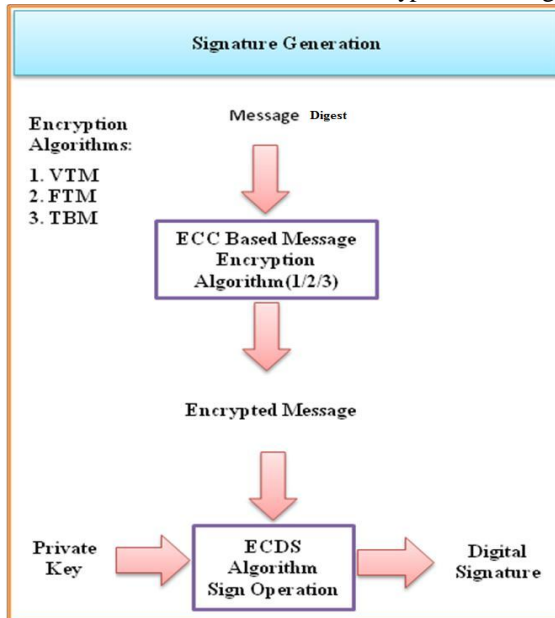


Figure 4: Signature Generation Process

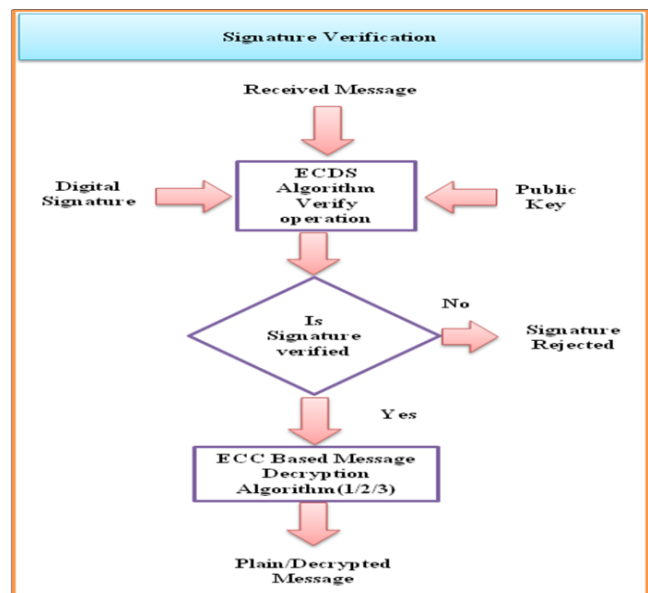


Figure 5: Signature Verification Process

V. Results and Discussion

In this section represents implementation results of ECDSA using VTM encryption over EC P-192 and P-256.

5.1. Results over Elliptic Curve P-192

Message m = "hello this is a raajasekhar from kurnool so plan to go us in the next year for working in DW Practice LL atlanta georgia "

Private key = 2055107281

Public Key = (5841942716391479201550342297351085963270983519924994377602, 5584890377300947026793868981513336619407548239394095574193)

This message encrypted and follows Signature Generation and Verification as mentioned below. Encrypted message hash value H(E(m)) = -2682108996977278156968408606235438945161064554

- ECDSA SIGNATURE as follows: Select k= 1583021364

Compute $kG = (3792194627815960440118002914594551166312864178888962630882, 2891190659620656059990718022662146728564853605540168001982)$
 $r = 62742A904369649DB4FD7CAD870EA7E7D2058DD5$
Compute $s = k^{-1}(e + dr) \bmod n = 3411184681610252308390502359065554562708605093739075483483$
Signature for the message m is (r, s) .

- ECDSA VERIFICATION as follows:
Compute $w = 5777480145803669741573423688926176979417082505271032360268$
Compute $u_1 = 4666422527249034100042022946337090008510597277184111303696$ $u_2 = 4455907927429886473277204474990236853124877171335661271649$
 $u_1G = (3929708989969467697197486716672122446942315632094831043367, 4537003456571103380284504813721792096119198047543959491671)$
 $u_2Q = (1277661715800205348067420766016806475954133626929696383370, 4380808460387567649107054289732585886848088206125448742447)$
 $v = 62742A904369649DB4FD7CAD870EA7E7D2058DD5$
We obtain $v = r$, that is accept the signature.

5.2. Results over Elliptic Curve P-256

Message $m =$ " The Elliptic Curve Digital Signature Algorithm Validation System (ECDSAVS) specifies the procedures involved in validating implementations of the Elliptic Curve Digital Signature Algorithm (ECDSA) as approved in FIPS 186-2, Digital Signature Standard (DSS)[1] and specified in ANSIX9.62-1998, Public Key Cryptography for Financial Services Industry: The Elliptic Curve Digital Signature Algorithm (ECDSA)[2]. The ECDSAVS is designed to perform automated testing on Implementations Under Test (IUTs). This document provides the basic design and configuration of the ECDSAVS. "

Private Key = 978425864

Public Key = (11891048790927442902274348574213558155367351099854008212509694993459447093822, 13669879720968471114272195759617137248100136400499358975374400163505099163986) This message encrypted and follows Signature Generation and Verification as mentioned below.

Encrypted message hash value $H(E(m)) = 537703090379649770402195397051062323069092491846$

- ECDSA SIGNATURE as follows:

Select $k = 11579208921035624876269744694940757352999695522413576034242259061068383502243$

Compute

$KG = (86500881224166483227925267313354237293018428812409245047778807509807358555053, 39579053610346434470532506438011786967057506613223689314593851851982117599776)$

$r = 86500881224166483227925267313354237293018428812409245047778807509807358555053$

Compute $s = k^{-1}(e + dr) \bmod n$

$= 104389700715501732796614779737855463749375844486540618622018054702970561091708$

Signature for the message m is (r, s) .

- ECDSA VERIFICATION as follows:

Compute $w = 106506396977556145535418054052339447393078832993181450002668470251312371474276$

Compute $u_1 = 4382449521180328495403435242713327430416111843142728664431922692704699529209$

$u_2 = 57692616982311160984176366728847647733800539362706147029132815066162592219439$

$u_1G = (1014746278933925641509492137032002037288731119848 92002825714765996844262058436, 6093742310915923099034833694998080 4564361965690646211671726514999151554795408)$

$u_2Q = (109322103145683055628956971282445177307378355734712278598030249871906512163766, 42753639382524136274231334284305572212602843186842236043136827079395299552547)$

$v = 86500881224166483227925267313354237293018428812409245047778807509807358555053$

We obtain $v = r$, that is accept the signature.

In the same way we have used TBM with plain message and encrypted for Signature generation and signature verification. ECDSA using Variable Size Text Message Encryption is better in performance aspect when compare with the other two methods and the results comparison is presented graphically in the next section.

VI. Comparison Of ECDSA Using Various Text Based Cryptosystems

We compare the results of ECDSA using Text Based Message with plain text (TBM) Encryption [6] and Text Based Message with message digest [6]. Figure 6 and Figure 7 presents total time taken for Signature Generation and Signature Verification when we use different text based encryption methods in ECDSA implementation. From Figure 6 and Figure 7, performance of ECDSA using Text Based Message with message digest Encryption is better when compare with ECDSA using TBM with plain text. The

reason is TBM based ECDSA used message digest compare with other one method. Performance of ECDSA is inversely proportional to key size, and security of the system depends on key size.

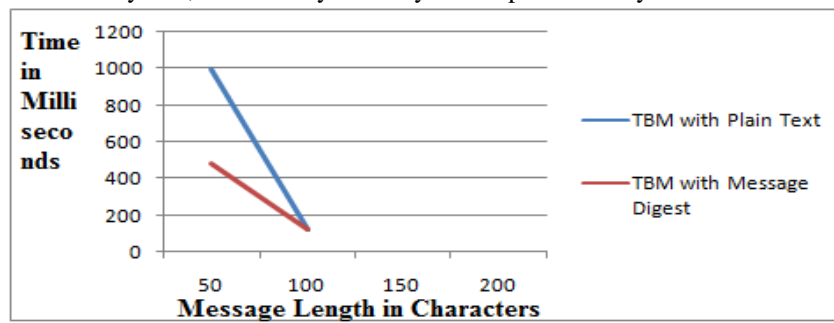


Figure 6: Performance comparison of various ECDSA methods for over EC P-192

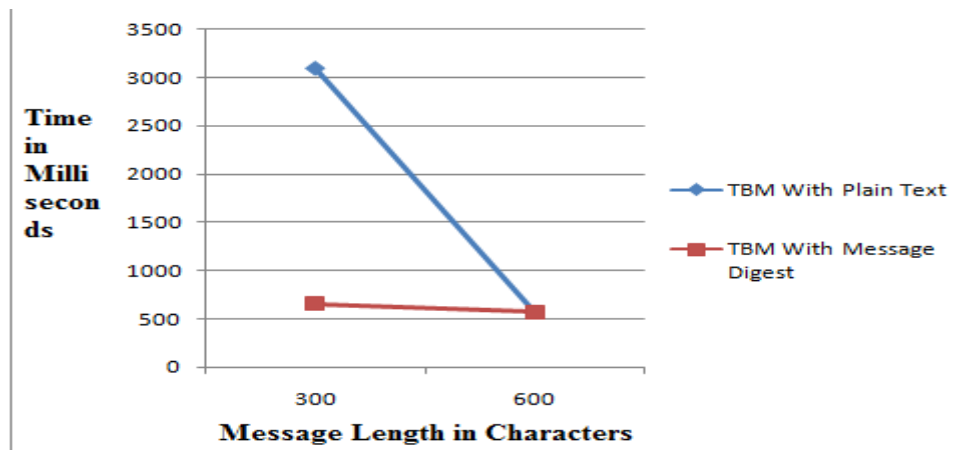


Figure 7: Performance comparison of various ECDSA methods for over EC P-256

VII. Conclusion

In this paper we have implemented ECDSA for various domain parameters, after observing the results when the key size increases then complexity increases and performance decreased. After comparing TBM with plain message and message digest based ECDSA methods, ECDSA using Variable Text Message Encryption with message digest is better when comparing with plain text Encryption used ECDSA. The main reason is, the speed of scalar multiplication which plays an important role in the efficiency of whole system [7]. In VTM based ECDSA method, number of scalar multiplications are reduced, so this method is efficient when compared with FTM and TBM based methods.

References

- [1] Navneet Randhawa, Lolita Singh, A Systematic Way to Provide Security for Digital Signature Using Elliptic Curve Cryptography, IJCST Vol.2, Issue 3, Sep-2011, 185-188
- [2] Koblitz, N., 1987. Elliptic curve cryptosystems. Mathematics of Computation 48, 203-209. [3] Miller, V., 1985. Use of elliptic curves in cryptography. CRYPTO 85.
- [4] Certicom ECC Challenge. 2009. Certicom Research
- [5] Jayabhaskar Muthukuru, Bachala Sathyanarayana, Fixed and Variable Size Text Based Message Mapping Techniques Using ECC, GJCST Vol.12, Issue 3, Feb-2012, 25-30.
- [6] S. Maria Celestin Vigila , K. Muneeswaran "Implementation of Text based Cryptosystem using Elliptic Curve Cryptography", IEEE Sep-2009, pp. 82-85.
- [7] Harsandeep Brar , Rajpreet Kaur, "Design and Implementation of Block Method for Computing NAF" IJCA, Volume 20- No.1, April 2011, pp. 37-41.
- [8] Hankerson, D., Menezes, A., Vanstone, S., Guide to Elliptic Curve Cryptography (Springer, 2004).

A Study on Partial Replacement of Natural Granite Aggregate with Pelletized Fly Ash Aggregate

¹Dr. V.Bhaskar Desai , ² A.Sathyam

¹ Professor, Dept. of Civil Engineering, JNTUA College of Engineering, Anantapuramu – 515002, A.P.

² Conservation Assistant Gr-I, Archaeological Survey of India, Anantapuramu Sub Circle, Central Stores Road, Anantapuramu & Research Scholar, JNTUA College of Engineering, Anantapuramu – 515002, A.P.

ABSTRACT : In this paper the use of pelletized fly ash aggregate in concrete as a partial replacement of granite aggregate has been examined. The concrete so produced is light weight in nature and the development of such concrete with cold bonded pelletized fly ash aggregate is to minimize the conventional aggregate, which results in protection of the natural environment. With the partial replacement (0%, 25%, 50%, 75% and 100%) of natural granite aggregate by pelletized fly ash aggregate, the strength properties of concrete such as compressive strength, split tensile strength, flexural strength and young's modulus of elasticity are studied.

KEY WORDS: Pelletization, cold bond, fly ash, light weight aggregate.

I. INTRODUCTION

Presently, in the construction industry throughout the world most of the concrete prepared is with natural granite aggregate as a major constituent. It's extensive usage results in geological and environmental imbalance. Also naturally available granite aggregate resources get depleted and it will be left nothing for future generations. Hence there is a necessity for preparing artificial aggregates making use of waste materials from agricultural products and industrial wastes. From the earlier studies, it appears that much less attention has been made towards study of usage of artificial coarse aggregate. An attempt has been made to use fly ash as the basic ingredient in preparing the artificial coarse aggregate which is also light in nature. Fly ash, a by-product of coal based material collected from Rayalaseema Thermal Power Plant (RTPP), Muddanur village of Andhrapradesh state has been used in this investigation. It consists of vitreous particles with a surface area is around 8.20 m²/gm when measured by nitrogen absorption techniques with particles approximately 100 to 150 times smaller than the cement particle. Because of its extreme fineness, it is an effective pozzolanic material and is used in concrete to improve its properties. One of the main properties of fly ash is its pozzolanic reactivity; hence it is suitable for most of its applications in various areas.

II. REVIEW OF LITERATURE

The Pelletization process is used to manufacture light weight Coarse aggregate. Some of the parameters need to be considered for the efficiency of the production of pellets are speed of revolution of pelletizer disc, moisture content, and angle of pelletizer disc and duration of Pelletization (HariKrishnan and RamaMurthy, 2006)¹. In the cold bonded method increase of strength of pellets is by increase the fly ash / lime & cement ratio by weight. Moisture content and angle of drum influence the size growth of pellets. Different types of pelletizer machines earlier were used to make the pellets such as disc or pan type, drum type, cone type and mixer type. With mixer type pelletizer small grains are formed initially and are subsequently increased. The dosage of binding agent is more important for making the fly ash balls. Initially some percentage of water is added to the binder and remaining water is sprayed during the rotation period because while rotating without water in the drum, the fly ash and binders (Lime & Cement) tend to form lumps and do not ensure the even distribution of particle size. The pellets are formed approximately in duration of 6 to 7 minutes. The cold bonded pellets are hardened by normal water curing method. The aggregates so prepared are fly ash based light weight aggregates (Gal'pern et al. 1990; Voortam et al. 1998; Watanable)²⁻⁴. The pelletized fly ash aggregate is light weight in nature and its use in concrete reduces the self weight of the structure (Bomhard, 1980; Roberts, 1992)⁵.⁶ besides attaining better thermal insulation properties. It is known that from the recent basic studies that the pelletized silica fume aggregate gives satisfactory strengths (Bhaskardesai and Sathyam, 2013)⁷. The setup of machine for manufacture of fly ash aggregate is as shown in plate 1.

(Owens, 1993)⁸ has stated that Light weight aggregate concrete is used for structural purposes since the 20th century. As per this study, the Light weight aggregate concrete is a material with low unit weight and often made with spherical aggregates. The density of structural Light weight aggregate concrete typically ranges from 1400 to 2000 kg/m³ when compared with that of normal weight aggregate concrete whose density is around 2400 kg/m³.(Siva lingaRao et al. 2011)⁹ concluded that 60 percent replacement of conventional aggregate with cinder by volume along with cement replaced by 10 percent of silica fume by weight, yields the target mean strength of M20 concrete. It is worth to be noted that there is a slight increase in strength and other properties due to extended curing periods and the unit weight of the cinder concrete varies from 1980 kg/m³ to 2000 kg/m³ with different percentages of cinder.

III. MATERIALS:

The following materials are used for this investigation and properties of materials are shown in table 1.

Tab. 1 MECHANICAL PROPERTIES OF MATERIALS

Sl.No	Name of the material	Properties of material	Result
1	OPC – 53 Grade	Specific Gravity	3.07
		Initial setting time	60 min
		Final Setting time	489 min
		Fineness	4.00 %
		Normal consistency	33.50 %
2	Fine Aggregate passing 4.75mm sieve	Specific Gravity	2.60
		Fineness modulus	3.24
3	FA Aggregate passing 20 – 10 mm	Specific Gravity	1.70
		Fineness modulus	4.69
		Bulk density compacted	1056 Kg/m ³
4	Natural Aggregate passing 20 – 10 mm	Specific Gravity	2.68
		Fineness modulus	3.37
		Bulk density compacted	1620 Kg/m ³
5	Water	Locally available potable water which is free from concentration of acids and organic substances has been used in this work.	

The constituent materials are presented from plate 2 to 7.

IV. EXPERIMENTAL INVESTIGATION

An experimental study has been conducted on concrete with partial replacement of conventional coarse aggregate i.e., granite by light weight aggregate i.e., FA aggregate. The test program consists of carrying out compressive tests on cubes, split tensile tests on cylinders, modulus of elasticity tests on cylinders and flexural strength on beams. Analysis of the results has been done to investigate effect of FA aggregate on the properties such as compressive strength, split tensile strength, flexural strength and modulus of elasticity. Variations of various combinations have been studied.

V. CASTING OF SPECIMENS

The M₂₀ concrete mix is designed using ISI method which gives a mix proportion of 1:1.55:3.04 with water cement ratio of 0.50. Five different mixes have been studied which are designated as follows as presented in table 2:

Tab. 2 DESIGNATION DETAILS OF SPECIMENS

Sl. No	Name of the Mix	Percentage by volume of natural coarse aggregate and fly ash aggregate		No of specimens cast and tested		
		Natural aggregate	Pelletized Fly Ash Aggregate	Cubes	Cylinders	Flexure beams
1	FA-0	100	0	6	12	6
2	FA-25	75	25	6	12	6
3	FA-50	50	50	6	12	6
4	FA-75	25	75	6	12	6
5	FA-100	0	100	6	12	6
Total specimens				30	60	30

To proceed with the experimental program initially steel moulds of size 150x150x150 mm were cleaned brushed with machine oil on all inner faces to facilitate easy removal of specimens afterwards. First fine aggregate and cement were added and mixed thoroughly and then conventional coarse

aggregates with partially replaced FA aggregate was mixed with them. All of these were mixed thoroughly by hand mixing. Each time 3 no of cubes and 6 no of cylinders were cast. For all test specimens, moulds were kept on the plat form and the concrete was poured into the moulds in three layers each layer being compacted thoroughly with tamping rod to avoid honey combing. Finally all specimens were vibrated on the table vibrator after filling up the moulds up to the brim. The vibration was effected for 7 seconds and it was maintained constant for all specimens and all other castings. However the specimens were demoulded after 24 hours of casting and were kept immersed in a clean water tank for curing. After 28 and 90 days of curing the specimens were taken out of water and were allowed to dry under shade for few hours.

VI. TESTING OF SPECIMENS

The cube or cylindrical specimen was kept vertically between the platens of the testing machine. The load is applied uniformly until the specimens fails, and ultimate loads were recorded. The test results of cube and cylinder compressive strengths are furnished in table 3 and 4 respectively. The cylindrical specimen was kept horizontally for finding the split tensile strength and the test results are furnished in table 5. The density and the ratio of cylinder to cube compressive strength results are furnished in table 6 & 7 respectively. An attempt to find out the modulus of elasticity has been done by the 3000 KN automatic compression testing machine with 0.5 KN/sec rate of loading. The results of modulus of elasticity are furnished in table no 8. The loading arrangement to test the specimens for flexural strength is simply supported over the span of 500mm. The loading was applied on the specimen using 15 ton pre-calibrated proving ring at regular intervals. The load was transmitted to the element through I- section and two 16mm diameter rods were placed at 166.67mm from each support. For each increment of loading the deflection at the centre and at 1/3rd points of beam were recorded using dial gauge. Continuous observations were made. Before the ultimate stage the deflection meters were removed and the process of load application was continued. As the load was increased the cracks got widened and extended to top and finally the specimen collapsed in flexure. At this stage the load was recorded as the ultimate load. The results have been tabulated and graphical variations have been studied. The test results are tabulated in table 9 and test set up are represented in plate 8.

VII. DISCUSSION OF CRACK PATTERN AND TEST RESULTS:

In case of cubes under compression test initial cracks are developed at top and propagated to bottom with increase in load and then the cracks are widened at failure along the edge of the cube and more predominantly along the top side of casting. In case of cylinders under compression cracks are developed at top and bottom and with increase in load the cracks are widened at central height. In case of cylinders subjected to split tensile strength the cylinder is splitted into two pieces. In case of beams the first crack developed at bending zone on tension side of beam and propagates to compression side of beam and the major crack is developed at bending zone only.

VIII. INFLUENCE OF FA AGGREGATE ON CUBE COMPRESSIVE STRENGTH

The superimposed variation between compressive strength versus percentage of pelletized fly ash aggregate replacing natural aggregate for 28 and 90 days curing periods are shown in fig 1. It is observed that with the addition of FA aggregate the cube compressive strength decreases continuously up to 100% replacement of Granite by FA aggregate. More than the target mean strength of M₂₀ concrete i.e., 26.6 N/mm² has been achieved even when the natural granite aggregate is replaced with 75% of FA aggregate as tabulated in table 3 i.e. 31.87 N/mm² for 28 days curing period. With the increase in curing period from 28 days to 90 days the compressive strength is found to increase marginally.

IX. INFLUENCE OF FA AGGREGATE ON CYLINDER COMPRESSIVE STRENGTH

The superimposed variation between compressive strength versus percentage of pelletized fly ash aggregate replacing natural aggregate for 28 and 90 days curing periods are shown in fig 2. It is observed that with the addition of FA aggregate the cylinder compressive strength decreases continuously up to 100% replacement of Granite by FA aggregate. The values are tabulated in table 4. With the increase in curing period from 28 days to 90 days the cylinder compressive strength is found to increase marginally.

INFLUENCE OF FA AGGREGATE ON SPLIT TENSILE STRENGTH ON CYLINDER SPECIMENS:

With increase in percentage replacement of granite by FA aggregate, the split tensile strength is found to decrease continuously up to 100%. The superimposed variation between split tensile strength versus percentage of pelletized fly ash aggregate replacing natural aggregate for 28 and 90 days curing periods as

shown in fig 3, and the values are tabulated in table 5. With the increase in curing period from 28 days to 90 days the split tensile strength is found to increase marginally.

INFLUENCE OF FA AGGREGATE ON DENSITY : The superimposed variation of density and percentage of FA aggregate replacing natural aggregate is presented in fig 4. From the fig it is observed that with the addition of FA aggregate the density of the specimens decreases continuously up to 100% replacement. The corresponding values are tabulated in table no 6. With the increase in curing period from 28 days to 90 days the densities are found to increase marginally.

INFLUENCE OF FA AGGREGATE ON YOUNG'S MODULUS (E) : The young's modulus is calculated by two approaches. i.e. by I.S.Code method¹⁰ and using an empirical formula for light weight concrete¹¹.

As per I.S.Code formula

$$E_1 = 5000 \sqrt{f_{ck}} \text{ N/mm}^2$$

Where f_{ck} = Characteristic cube compressive strength of concrete at 28 days of curing.

Secondly another formula suggested by Takafumi Naguchi et.al¹¹ for light weight aggregate concrete, is given by

$$E_2 = k_1 \times k_2 (1.486 \times 10^{-3}) \times \sigma_b^{1/2} \times \gamma^2 \text{ N/mm}^2.$$

Where k_1 = correction factor for coarse aggregate i.e. 0.95

k_2 = correction factor for mineral admixture i.e. 1.026

σ_b = compressive strength of concrete in MPa.

γ = Density of concrete in kg/m³

The superimposed variation between young's modulus versus percentage of pelletized fly ash aggregate replacing natural aggregate for 28 and 90 days curing periods are shown in fig 6 & 7 respectively. With increase in percentage of replacement of granite by FA aggregate, the E values are found to decrease continuously up to 100% replacement. These values are tabulated in table 8. From these results it can be found that the E-values calculated using I.S.Code formula are higher than those calculated from the suggested empirical formula for light weight concrete.

INFLUENCE OF FA AGGREGATE ON FLEXURAL STRENGTH ON BEAMS: The flexural strength is also calculated by two approaches. In the first approach the flexural strength is calculated by using the following standard formula. i.e.

$$f_{th} = \frac{PL}{bd^2} \text{ in N/mm}^2$$

Where f_{th} = Flexural strength of the beam in N/mm²

P = Ultimate Load in N

L, b, d = Sectional dimensions of the beam

Another formula as per I.S.code method¹⁰ is

$$f = 0.7 \sqrt{f_{ck}}$$

Where f = Flexural strength of beam in N/mm²

f_{ck} = Characteristic cube compressive strength of concrete at 28 days of curing.

The superimposed variation between flexural strength versus percentage of pelletized fly ash aggregate replacing natural aggregate for 28 and 90 days curing periods are shown in fig 8 & 9 respectively. With increase in percentage of replacement of granite aggregate by FA aggregate, the flexural strength values are found to decrease continuously up to 100% replacement. Further by extending the curing period from 28 days to 90 days the flexural strength values are found to increase. These values are tabulated in table 9.

X. CONCLUSIONS

On the basis of limited experimental investigations conducted and the analysis of results, the following conclusions are drawn to be valid.

- [1] From the experimental investigation it is observed that the production of structural light weight aggregate concrete from cold bonded pelletized fly ash aggregate is possible.
- [2] The pelletized fly ash aggregates are lighter and porous in nature; having bulk density around 1056 kg/m³ which is less than that for conventional aggregate and hence it is light weight aggregate.
- [3] The cold bonded pelletized fly ash aggregates are spherical in shape and hence it improves the workability of content mixes with lesser water content when compared with conventional concrete.
- [4] From the study it is concluded that the compressive strength, split tensile strength, young's modulus, flexural strength and density are decreased continuously with the increasing FA aggregate concrete replacing the natural aggregate; and also increased with increasing curing period.
- [5] E_1 values calculated as per I.S.Code formula are higher when compared with E_2 values calculated using another empirical formula suggested for light weight aggregate concrete.
- [6] Flexural strengths calculated as per I.S.Code formula are lower when compared with those flexural strengths calculated experimentally.

Tab. 3 CUBE COMPRESSIVE STRENGTH RESULTS

Sl. No	Name of the mix	Percentage by volume of natural coarse aggregate and fly ash aggregate		Compressive strength N/mm ²	
		Natural aggregate	Pelletized Fly Ash Aggregate	28 days	90 days
1	FA-0	100	0	41.08	47.39
2	FA-25	75	25	34.80	34.96
3	FA-50	50	50	32.74	34.03
4	FA-75	25	75	31.87	32.47
5	FA-100	0	100	22.93	23.76

Tab. 4 CYLINDER COMPRESSIVE STRENGTH RESULTS

Sl. No	Name of the mix	Percentage by volume of natural coarse aggregate and fly ash aggregate		Compressive strength N/mm ²	
		Natural aggregate	Pelletized Fly Ash Aggregate	28 days	90 days
1	FA-0	100	0	28.01	28.04
2	FA-25	75	25	18.04	18.31
3	FA-50	50	50	16.48	17.72
4	FA-75	25	75	13.84	16.23
5	FA-100	0	100	12.99	15.84

Tab. 5 SPLIT TENSILE STRENGTH RESULTS

Sl. No	Name of the mix	Percentage by volume of natural coarse aggregate and fly ash aggregate		Split Tensile strength N/mm ²	
		Natural aggregate	Pelletized Fly Ash Aggregate	28 days	90 days
1	FA-0	100	0	3.58	4.00
2	FA-25	75	25	2.84	3.40
3	FA-50	50	50	2.65	3.12
4	FA-75	25	75	2.52	3.30
5	FA-100	0	100	2.00	2.65

Tab. 6 DENSITY RESULTS

Sl. No	Name of the mix	Percentage by volume of natural coarse aggregate and fly ash aggregate		Density in Kg/m ³	
		Natural aggregate	Pelletized Fly Ash Aggregate	28 days	90 days
1	FA-0	100	0	2309	2396
2	FA-25	75	25	2280	2350
3	FA-50	50	50	2230	2241
4	FA-75	25	75	2134	2138
5	FA-100	0	100	2007	2123

Tab. 7 RATIO OF CYLINDER TO CUBE COMPRESSIVE STRENGTH

Sl.No	Name of the mix	Percentage by volume of natural coarse aggregate and fly ash aggregate		Compressive strength N/mm ²				Ratio of cube to cylinder compressive	
		Natural aggregate	Pelletized Fly Ash Aggregate	Cylinder		Cube		28 days	90 days
				28 days	90 days	28 days	90 days		
1	FA-0	100	0	28.01	28.04	41.08	47.39	0.68	0.59
2	FA-25	75	25	18.04	18.31	34.80	34.96	0.52	0.52
3	FA-50	50	50	16.48	17.72	32.74	34.03	0.50	0.52
4	FA-75	25	75	13.84	16.23	31.87	32.47	0.43	0.50
5	FA-100	0	100	12.99	15.84	22.93	23.76	0.57	0.67

Tab. 8 YOUNGS MODULUS

Sl. No	Name of the mix	Percentage by volume of natural coarse aggregate and fly ash aggregate		E ₁ =Young's modulus in KN/mm ² using I.S.Code formula		E ₂ = Young's modulus in KN/mm ² using Takafumi formula		E ₂ / E ₁	
		Natural aggregate	Pelletized Fly Ash Aggregate	28 days	90 days	28 days	90 days	28 days	90 days
1	FA-0	100	0	32.05	34.42	26.32	29.71	0.82	0.86
2	FA-25	75	25	29.50	29.56	24.29	25.85	0.82	0.87
3	FA-50	50	50	28.61	29.17	22.78	23.30	0.80	0.80
4	FA-75	25	75	28.23	28.49	20.67	20.88	0.73	0.73
5	FA-100	0	100	23.94	24.37	16.40	18.57	0.69	0.76

Tab. 9 FLEXURAL STRENGTH RESULTS

Sl. No	Name of the mix	Percentage by volume of natural coarse aggregate and fly ash aggregate		Flexural Strength (f_{ex}) in KN/mm ²		Flexural strength (f_{in}) in KN/mm ²		$(f_{ex})/(f_{in})$	
		Natural aggregate	Pelletized Fly Ash Aggregate	28 days	90 days	28 days	90 days	28 days	90 days
1	FA-0	100	0	6.83	7.35	4.49	4.82	1.52	1.53
2	FA-25	75	25	4.20	4.73	4.13	4.14	1.02	1.14
3	FA-50	50	50	3.15	3.68	4.01	4.08	0.79	0.90
4	FA-75	25	75	2.63	3.15	3.95	3.99	0.66	0.79
5	FA-100	0	100	2.10	2.63	3.35	3.41	0.63	0.77

REFERENCES

- [1] Harikrishnan KI, Ramamurthy (2006). Influence of Pelletization Process on the Properties of Fly Ash Aggregates. Waste Manag., 26: 846-852..
- [2] E I Gal'pern, L A Kotkina and I O Mnskin. 'porous aggregates from beneficiated thermal power plant ash (USSR).' Energ stroit, vol 2, 1990, pp 38-39.
- [3] H.Voortam, R Visser and B V Vastam. 'Light Weight Aggregate for advanced and Profitable Civil Engineering Production properties and Use.' Int conf on fly ash disposal and utilisation, CBIP, January 20-22, vol 1, 1998, New Delhi, pp IV-1-10.
- [4] H Watanable. 'Artificial stone from fly ash for building materials (Watanable Hikotoshi).' Jpn kokai Tokyo Koho JP02, 116, 653, [90, 116, 653], (C1.C04 B28/02).
- [5] Bomhard. "Light weight concrete structures, potentialities, limits and realities, in light weight concrete." Concrete society, The construction press Ltd, Lancaster, England, 1980, pp 277-307.
- [6] J E Roberts. "Light weight concrete bridges for California highway system" in "structural light weight aggregate concrete performance." Holm T A, Vaysburd, AM(Ed), ACI, SP-136 Detroit, 1992, pp 255-272.
- [7] V.Bhaskar desai, A.Sathyam. 'Basic properties of artificial light weight aggregate by using industrial by product (Silica fume)', RCEE, 2013, vol 1 (04), pp 195-201.
- [8] Owens, P.L. (1993). "Light weight aggregates for structural concrete," Structural Light weight Aggregate Concrete, Chapman & Hall, London, pp.1-18.
- [9] N. Siva lingaRao, G. VenkataRamana, V. Bhaskar Desai, B. L.P. Swamy, "Properties of lightweight aggregate concrete with cinder and silicafume admixture", International Journal of Earth Sciences and Engineering, Vol. 4, No. 6, October 2011, pp. 907-912.
- [10] I.S.Code 456-2000 "Code of practice for plain and reinforced concrete" Bureau of Indian Standards, New Delhi.
- [11] Takafumi Noguchi, et.al (2009) " A Practical Equation for Elastic Modulus of Concrete". ACI structural journal/Sept-Oct 2009, technical paper title no. 106-SXX.

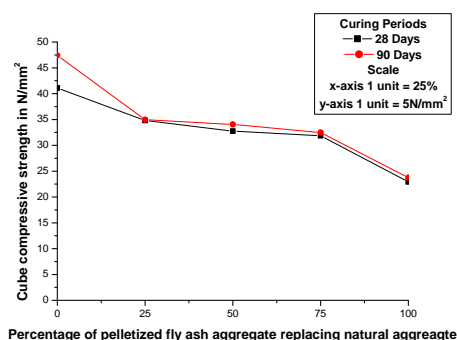


Fig 1. Superimposed Variation Between Cube Compressive Strength And Percentage Of Pelletized Fly Ash Aggregate Replacing Natural Aggregate

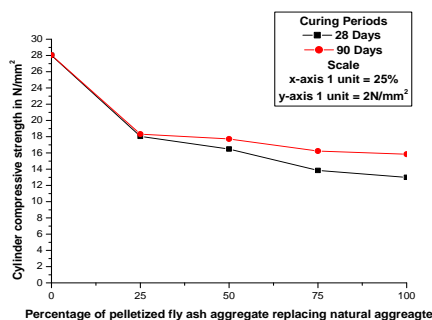


Fig 2. Superimposed Variation Between Cylinder Compressive Strength And Percentage Of Pelletized Fly Ash Aggregate Replacing Natural Aggregate

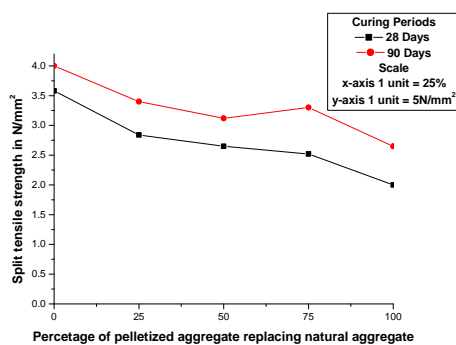


Fig 3. Superimposed Variation Between Split Tensile Strength And Percentage Of Pelletized Fly Ash Aggregate Replacing Natural Aggregate

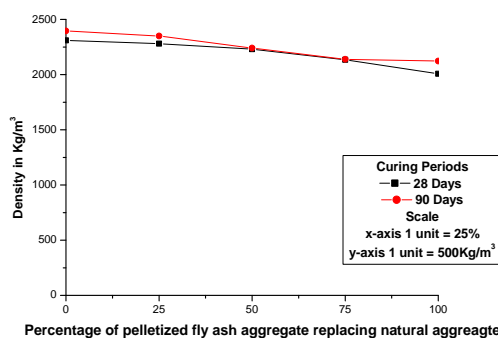


Fig 4. Superimposed Variation Between Density And Percentage Of Pelletized Fly Ash Aggregate Replacing Natural Aggregate

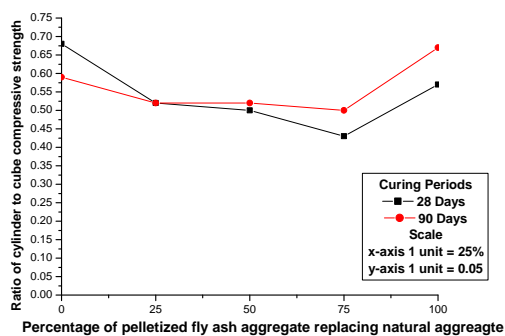


Fig 5. Superimposed Variation Between Ratio Of Cylinder To Cube Compressive Strength And Percentage Of Pelletized Fly Ash Aggregate Replacing Natural Aggregate

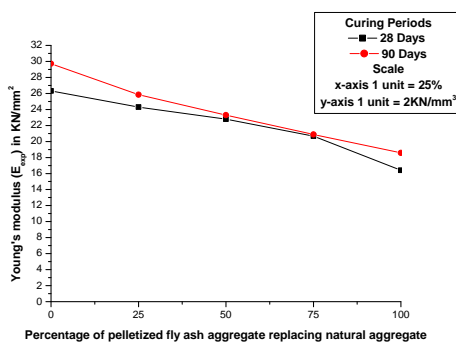


Fig 6. Superimposed Variation Between Young's Modulus (E_{exp}) And Percentage Of Pelletized Fly Ash Aggregate Replacing Natural Aggregate

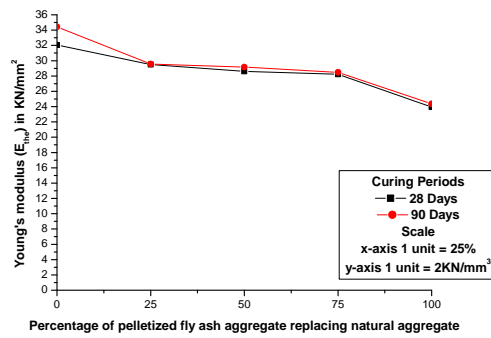


Fig 7. Superimposed Variation Between Young's Modulus (E_{the}) And Percentage Of Pelletized Fly Ash Aggregate Replacing Natural Aggregate

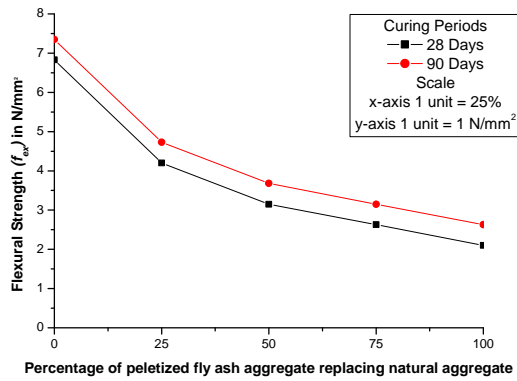


Fig 8. Superimposed Variation Between Fluxural Strength (F_{ex}) And Percentage Of Pelletized Fly Ash Aggregate Replacing Natural Aggregate

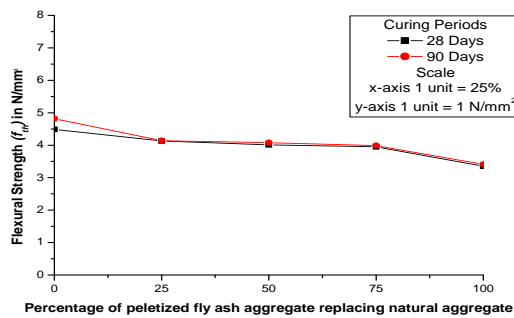


Fig 9. Superimposed Variation Between Fluxural Strength (F_{th}) And Percentage Of Pelletized Fly Ash Aggregate Replacing Natural Aggregate

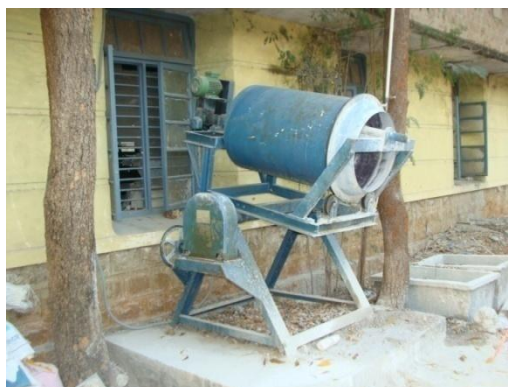


Plate 1. Pelletization Machine



Plate 2. Fly Ash Powder



Plate 3. Lime



PLATE 4. CEMENT



PLATE 5. PELLETIZED FLY ASH AGGREGATE



PLATE 6. FINE AGGREGATE



PLATE 7. NATURAL COARSE AGGREGATE



Plate 8: Test Set Up For Flexural Strength Before Testing

An Experimental Investigation to Optimize the Process Parameters of Surface Finish in Turning AISI 202 Stainless Steel Using Taguchi Approach

Anoop Pandey¹, Sandeep Garg², Payal Damle³, Mahindra Rautela⁴, Mohit Choudhary⁵, Harshit Bhalla⁶

^{1,2,3,4,5,6} ABES Engineering College, Ghaziabad,

ABSTRACT:

This paper aims at optimization of process parameters of surface finish for turning AISI 202 austenitic stainless steel using Taguchi approach. Nine cylindrical bars of AISI 202 of diameter 20mm are turned to a length of 20 mm in each experiment for a constant spindle speed of 73.5 rpm on conventional lathe machine. Coolant concentration, Feed rate, Depth of cut and rake angle of tool are taken as the process parameters. A Taguchi orthogonal array is designed with three levels of machining parameters and analysis of S/N ratios, response table and regression equations were made with the help of Minitab 16 software.

KEYWORDS: AISI 202, DOE, taguchi method, turning, S/N ratio.

I. INTRODUCTION

Attaining optimum surface finish in the presence of constraints like MRR and economics of machining is one of the challenging tasks encountered by many growing industries these days. Several factors influence surface finish and there is a need to optimize these parameters. Taguchi method can help in optimizing these parameters taking into consideration of economy. The Taguchi method is a well-known technique that provides an efficient and systematic methodology for optimization of process parameters and this is a powerful tool for the design of high quality systems with low development and manufacturing costs. Signal to noise ratio and orthogonal array are two major tools used in robust design. The S/N ratio characteristics can be divided into following three categories when the characteristic is continuous [1]:

- a) Nominal is the best
- b) Smaller the better
- c) Larger is better characteristics.

For surface roughness, the solution is “smaller is better” and S/N ratio is determined by the following equation:

$$n = -10 \log_{10} [1/n (\sum y_i^2)] \text{ ---Equation 1}$$

Where n = No. of Measurements, y = Measured Value which is in Ra.

In this experiment, 4 parameters are chosen having 3 levels. Without using Taguchi method total number of experiments should be $3^4=81$ experiments. But using taguchi L9 array as shown in figure 1, 9 experiments are proposed providing nearly same accuracy. Those nine experiments will give 96% accurate result. By using this method number of experiments reduced to 9 instead of 81 with almost same accuracy.

Experiment	P1	P2	P3	P4
1	1	1	1	1
2	1	2	2	2
3	1	3	3	3
4	2	1	2	3
5	2	2	3	1
6	2	3	1	2
7	3	1	3	2
8	3	2	1	3
9	3	3	2	1

Figure 1: Taguchi L9 orthogonal array

II. EXPERIMENTAL DETAILS”

Work material : AISI 202 is an austenitic stainless steel with relatively low nickel content as compared to 300 and 300L series. Martensitic stainless steels have better properties than austenitic stainless steels but nowadays due to the rising prices of nickel the use of austenitic stainless steel is increasing tremendously. AISI 202 austenitic stainless steel finds its application in general industrial and process-industry machinery and equipment, automotive industry, structural, bus body, electrical machinery etc [2]. Figure 2 is showing the chemical properties of AISI 202 and Figure 3 is showing the mechanical-thermal properties of AISI 202.

elements	Composition (percent)
C	< 0.15
Si	< 1.00
Mn	7.5-10.0
P	< 0.06
S	< 0.03
Cr	17.0-19.0
Ni	4-6
Mo	0

Figure 2: Chemical composition of AISI 202

Sr. no	Mechanical property	Value
1	Density(Kg/m ³)	7800
2	Poisson's ratio	0.27-0.30
3	Elastic modulus (GPa)	190-210
4	Tensile strength (MPa)	515
5	Yield strength (MPa)	275
6	Thermal expansion/(degree C)	0.0000175
7	Thermal conductivity(W/m-K)	16.2
8	Specific heat(J/kg-K)	500
9	Hardness(HRC)	38-43

Figure 3: Mechanical and thermal properties of AISI 202

As seen from the table because of high hardness & lower thermal conductivity, it becomes difficult to machine AISI 202 at higher speed and without the application of cutting fluid. Sometimes at higher temperatures without using cutting fluids chromium reacts with carbon to form carbides which get deposited on grain boundaries and depletes the properties of AISI 202. Proper set of parameters are to be chosen to obtain optimum surface finish without degrading the properties of the material.

Tool material : S-400(T-42) which is a high cobalt high speed steel tool having a hardness of 66-68 HRC was used in the experiment. There are two grades of HSS tools available, namely T series and M series. These two series differ mainly in the composition of tungsten, cobalt and molybdenum. T series has higher content of tungsten and cobalt while M series has higher molybdenum. Red hardness and tempering retention of T series is larger than M series due to the large cobalt and tungsten content as compared to M series but M series possesses good grindability and higher strength in tension, shear and bending .[3].

Element	Composition
C	1.25-1.40
Si	0-0.04
Mn	0-0.04
P	0.35
S	0.35
Cr	3.75-4.50
Mo	2.75-3.50
V	2.75-3.25
W	8.50-9.50
Co	9-10
Ni	0-0.04

Figure 4: Chemical Composition of AISI T-42 tool

All the six angles along with the appropriate nose radius were ground on the tool as shown in table 1. In the experiment, three HSS tools with top rake angle 8, 12 and 16 degrees were used to observe the effect of rake angles along with 3 other parameters on the surface finish.

Table 1: Geometry of AISI T-42 tool

S No	Angle	Value
1	Side rake angle	7°
2	Back rake angle	variable
3	Side cutting edge angle	13°
4	End cutting edge angle	12°
5	Side relief angle	6°
6	End relief angle	8°
7	Nose radius	0.2mm

Cutting fluid : Cutting fluid plays a major role in machining process. Emulsifier or emulsion is used as a cutting fluid in this experiment. Emulsions are the mixture of mineral oils and water. Water provides good cooling and oil provides good lubrication. Therefore both serve the function of removing heat from the cutting zone as well as reducing wear-tear and friction. It is a brown color, paraffinic oil soluble, bio-stable semi-synthetic product which turns into white color on adding water. It is particularly recommended for all machining operations. In this study, ratio of water and oil in the emulsion is varied between 20:1 and 40:1 to optimize between cooling property and lubricating property of the emulsion used.

III. EXPERIMENTAL PROCEDURE

Nine round bars of equal diameter 20mm and equal length 30mm are prepared from a long rod of AISI 202. Feed, depth of cut, rake angle and coolant concentration are the variables of the process with following the levels given in table 2

Table 2: Machining parameters and levels

	Coolant Concentration (V/V)	Feed (mm/rev)	Depth of cut (mm)	Rake angle (degrees)
Level 1	20	0.1701	0.5	8°
Level 2	30	0.3868	0.7	12°
Level 3	40	0.6939	1.0	16°

Using taguchi L9 array and DOE, the experiments are designed as shown in the Table 3 below

Table 3: Design of Experiment

	Concentration of coolant (V/V)	Feed (mm/rev)	Depth of cut(mm)	Rake angle(degrees)
1	20	0.1701	0.5	8°
2	20	0.3868	0.7	12°
3	20	0.6939	1.0	16°
4	30	0.1701	0.7	16°
5	30	0.3868	1.0	8°
6	30	0.6939	0.5	12°
7	40	0.1701	1.0	12°
8	40	0.3868	0.5	16°
9	40	0.6939	0.7	8°

The Workpiece is turned to a length of 20 mm in each experiment for a constant spindle speed of 73.5 rpm and their surface finish is measured on surface testing machine and following results were obtained as shown in table 4

Table 4: Experimental values of surface roughness

	Concentration (V/V)	Feed (mm/rev)	Depth of cut(mm)	Rake (deg)	Surface roughness Ra
1	20	0.1701	0.5	8°	16.367
2	20	0.3868	0.7	12°	6.260
3	20	0.6939	1.0	16°	3.342
4	30	0.1701	0.7	16	8.810
5	30	0.3868	1.0	8°	2.560
6	30	0.6939	0.5	12°	9.200
7	40	0.1701	1.0	12°	24.061
8	40	0.3868	0.5	16°	12.687
9	40	0.6939	0.7	8°	3.888



Figure 5: Machined samples

IV. DATA ANALYSIS”

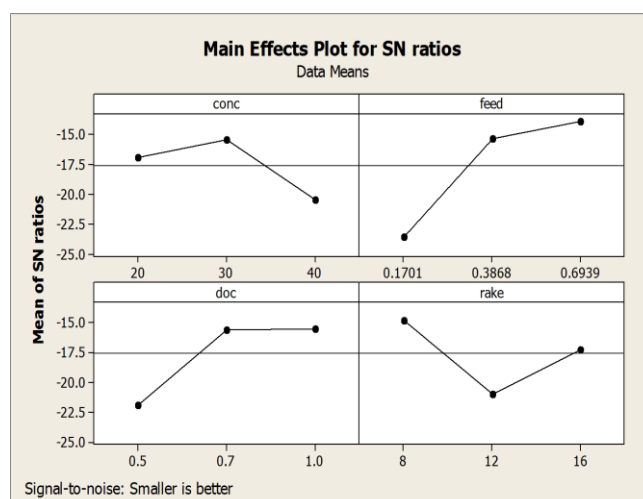
After performing experiments, parameters are optimized by using Minitab 16 software. The calculation, results and graphs of S/N ratio, response table and regression equation are provided by Minitab 16 software.

S/N ratios:

Table 5: S/N ratios @ Minitab 16

Experiment no	S/N ratios
1	-24.279
2	-15.932
3	-10.480
4	-18.899
5	-8.1648
6	-19.276
7	-27.626
8	-22.067
9	-11.795

4.2. S/N plots:



Plot 1: S/N plot @ Minitab 16

It is seen from the above graph that:

- a. S/N ratios increases as coolant concentration increases, reaches maximum at 30:1 V/V and then decreases.
- b. S/N ratio increases as the feed increases; maximum S/N ratio is obtained at a feed of 0.6939.
- c. S/N ratio increases as the depth of cut increases achieves maximum value at a depth of cut of 0.7mm and then becomes almost constant.
- d. S/N ratio reduces as rake angle increases, achieves minimum value and then increases with concentration. Maximum S/N ratio is obtained at a rake angle of 8°.

Response table:

Table 6: Response table obtained @ Minitab 16

Level	Concentration	Feed	Depth of cut	Rake angle
1	-16.90	-23.60	-21.87	-14.75
2	-15.45	-15.39	-15.54	-20.94
3	-20.50	-13.85	-15.42	-17.15
Delta	5.05	9.75	6.45	6.20
Rank	4	1	2	3

The response table has provided feed has rank 1, depth of cut rank 2, rake angle rank 3 and coolant concentration rank 4.

V. REGRESSION ANALYSIS

Regression equation was implemented to obtain the correlation between the machining parameters and the measured surface roughness.

The regression equation is:

$$\text{Surface Roughness } R_a = 12.6 + 0.244 \text{ concentration} - 19.9 \text{ feed} - 4.1 \text{ doc} + 0.084 \text{ rake.}$$

VI. RESULTS AND CONCLUSIONS

- [1] An experiment having feed of 0.6939 mm/rev, depth of cut of 0.7mm, rake angle of 8° and concentration of 30:1 V/V will give the optimum machining parameters.
- [2] The most prominent parameter is feed followed by depth of cut, rake angle and coolant concentration.

REFERENCES

- [1] Krishankant, Jatin Taneja, Mohit Bector and Rajesh Kumar “Application of Taguchi Method for Optimizing Turning Process by the effects of Machining Parameters”-International Journal of Engineering and Advanced Technology (IJEAT) ISSN: 2249 – 8958, Volume-2, Issue-1.
- [2] M. Kaladhar, K. V. Subbaiah, Ch. Srinivasa Rao and K. Narayana Rao “Application of Taguchi approach and Utility Concept in solving the Multi-objective Problem when turning AISI 202 Austenitic Stainless Steel” - Journal of Engineering Science and Technology, ISSN: 1791-2377.
- [3] U.K.Vates, N.K. Singh, R.V. Singh “ANN Modeling and Optimization of Ra with corresponding MRR on HSS T42 Steel using WEDM Process”- International Journal of Mechanical & Mechatronics Engineering IJMME-IJENS Vol:14 No:03.

New Hybrid Intrusion Detection System Based On Data Mining Technique to Enhance Performance

LUCKY SHARMA

Medicaps Institute Of Technology And Management, Indore(MP)
Ragiv Gandhi Technical University Bhopal(MP)

ABSTRACT:

Intrusion Detection Systems (IDSs) is an efficient defense technique against network attacks as well host attacks since they allow network/host administrator to detect any type policy violations. However, traditional IDS are vulnerable and they are not reliable to novel and original malicious attacks. Also, it is very inefficient to analyze from a big amount of data such as possibility logs. Moreover, there are high false positives and false negatives for the common OSs. There are many other techniques which can help to improve the quality and results of IDS in which data mining one of them where it has been popularly recognized/identify as an important way to mine useful information from big amount of data which is noisy, and random. Integration of various data mining techniques with IDS to improve efficiency is the motive of proposed research. Proposed research is combining three data mining technique to reduce over head and improve execution efficiency in intrusion detection system (IDS). The Proposed research that ensembles clustering (Hierarchical) and two classifications (C5.0, CHAID) approaches. Proposed IDS execute on the standard KDD'99 (knowledge Discovery and Data Mining) Data set; this data set is used for measuring the performance of intrusion detection systems. Proposed system can detect the intrusions and classify them into four categories: Probe, Denial of Service (DoS), U2R (User to Root), and R2L (Remote to Local). A presented experiment results is carried out to the performance of the proposed IDS using KDD 99' dataset. Its shows that the proposed IDS performed better in term of accuracy, and efficiency.

KEYWORDS- Internet; intrusion detection; data mining; Clustering, Classification, data

I. INTRODUCTION

Information security technology is an essential component for protecting public and private computing infrastructures. With the widespread utilization of information technology applications, organizations are becoming more aware of the security threats to their resources. No matter how strict the security policies and mechanisms are, more organizations are becoming susceptible to a wide range of security breaches against their electronic resources. Network-intrusion detection is an essential defense mechanism against security threats, which have been increasing in rate lately. It is defined as a special form of cyber threat analysis to identify malicious actions that could affect the integrity, confidentiality, and availability of information resources. Data mining-based intrusion-detection mechanisms are extremely useful in discovering security breaches. An intrusion detection system (IDS) is a component of the computer and information security framework. Its main goal is to differentiate between normal activities of the system and behavior that can be classified as suspicious or intrusive [11].

IDS's are needed because of the large number of incidents reported increases every year and the attack techniques are always improving. IDS approaches can be divided into two main categories: misuse or anomaly detection [12]. The misuse detection approach assumes that an intrusion can be detected by matching the current activity with a set of intrusive patterns. Examples of misuse detection include expert systems, keystroke monitoring, and state transition analysis. Anomaly detection systems assume that an intrusion should deviate the system behavior from its normal pattern. This approach can be implemented using statistical methods, neural networks, predictive pattern generation and association rules among others techniques. In this research using naïve byes classification with clustering data mining techniques to extract patterns that represent normal behavior for intrusion detection. This research is describing a variety of modifications that will have made to the data mining algorithms in order to improve accuracy and efficiency. Using sets of naïve byes classification rules that are mined from network audit data as models of "normal behavior."

To detect anomalous behavior, it will generate naïve byes classification probability with clustering followed from new audit data and compute the similarity with sets mined from “normal” data. If the similarity values are below a threshold value it will show abnormality or normality [12].

II. PROPOSED WORK

This Chapter is going to be present general idea on a new proposed concept for intrusion detection system which will enhance efficiency as compare existing intrusion detection system. The proposed concept is using data mining techniques. Data mining techniques have been successfully applied in many different fields including marketing, manufacturing, process control, fraud detection, and network management. Over the past five years, a growing number of research techniques have applied data mining to various problems in intrusion detection. In this will apply to data mining for anomaly detection field of intrusion detection. Presently, it is unfeasible for several computer systems to affirm security to network intrusions with computers increasingly getting connected to public accessible networks (e.g., the Internet). In view of the fact that there is no ideal solution to avoid intrusions from event, it is very significant to detect them at the initial moment of happening and take necessary actions for reducing the likely damage. One approach to handle suspicious behaviors inside a network is an intrusion detection system (IDS). For intrusion detection, a wide variety of techniques have been applied specifically, data mining techniques, artificial intelligence technique and soft computing techniques. Most of the data mining techniques like association rule mining, clustering and classification have been applied on intrusion detection, where classification and pattern mining is an important technique.

Proposed Concept: Here proposed concept are going to be present general idea as showing in figure 1 for intrusion detection system which will enhance efficiency as compare existing intrusion detection system. The proposed concept is using data mining techniques. In this clustering and classification data mining technique has applied for anomaly detection field of intrusion detection. Anomaly learning approaches are able to detect attacks with high accuracy and to achieve high detection rates. However, the rate of false alarm using anomaly approach is equally high. In order to maintain the high accuracy and detection rate while at the same time to lower down the false alarm rate, the proposed technique is the combination of three learning techniques. For the first stage in the proposed technique, this grouped similar data instances based on their behaviors by utilizing a hierarchical clustering as a pre-classification component. Next, using C5.0 classifier this classified the resulting clusters into attack classes as a final classification task. This found that data that has been misclassified during the earlier stage may be correctly classified in the subsequent classification stage. At last CHAID classification is applied. Following is the proposed IDS which divided into following module:

1. Database Creation (Suggested Technique)
 - Download and Rearranged KDD 99'
 - Data Formation and Re-Processing of KDD 99'(Training and Testing Data Set Preparation)
2. Data mining Techniques
 - Cluster Technique
 - Hierarchical Clustering
 - Classification
 - C5.0
 - CHAID
3. Proposed System
 - K-Mean Clustering
 - K-Mean Clustering with Naïve Bayse classification
 - K-Mean with Naïve Bayse classification and Decision Table Majority Rule Based Approach
 - Hierarchical Clustering
 - Hierarchical Clustering with C5.0 classification
 - Hierarchical Clustering with C5.0 classification and CHAID Classification
4. Performance
 - Time Analysis
 - Memory Analysis
 - CUP Analysis

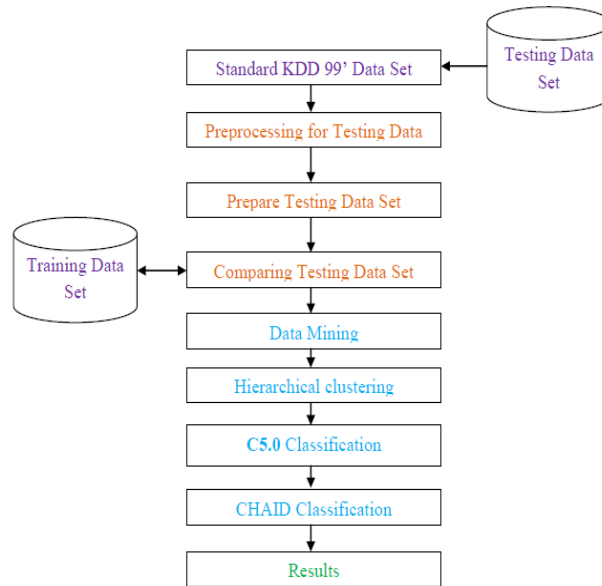


Figure 1: Block Diagram of Proposed Concept

Proposed Architecture: In the proposed work, outline a data mining approaches for designing intrusion detection models. The Basic idea behind this is that apply various data mining technique in single to audit data to compute intrusion detection models, as per the observation of the behavior in the data. In the proposed work are the combining three most useable data mining techniques into single concept and presenting architecture shown in figure 4.2. In proposed technique, use Hierarchical clustering, C5.0 algorithm and CHAID approach. First apply the hierarchical algorithm to the given dataset to split the data records into normal cluster and anomalous clusters. It specifies the number of clusters as five to the hierarchical and clusters the records in the dataset into normal cluster and anomalous clusters. The anomalous clusters are U2R, R2L, PROBE, and DoS. The records are labeled with the cluster indices. Then, divide the data set into two parts. One part is used for training and the other one is used for evaluation. In training phase, apply the labeled records to the C5.0 for training purpose. The C5.0 classifier is trained with the labeled records. Then, apply the rest of unlabeled records to the C5.0 for classification. The C5.0 classifier will classify the unlabelled record into normal and anomalous clusters. Finally apply CHAID which is also the classifier that is doing exact match of each attribute values all to gather and thus removes the strong independence assumption. The Proposed work consists of clustering, classification where proposed architecture as shown in figure 2.

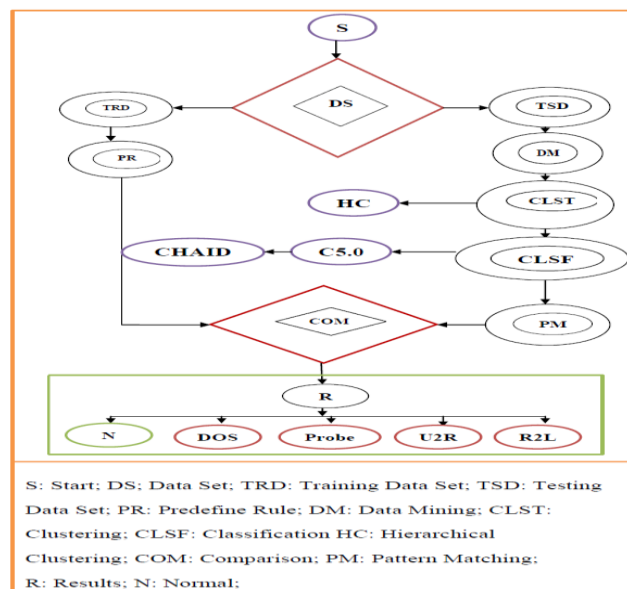


Figure 2: Architecture of the Proposed IDS

Proposed Algorithm : Input: Dataset KDD, a sample K, Normal Cluster NC, Abnormal cluster AC, c is the number of clusters and d is the distance between them, ch1,ch2,ch3,ch4,ch5 are Nodes i1,i2,i3,i4 are the category

Output: K is abnormal or normal

Algorithm Hybrid

A) First apply Hierarchical clustering

- 1) Firstly load data into a root cluster and we start with one cluster and successively split clusters to produce others, more and more samples are clustered together in a hierarchical manner.
- 2) For Every data point:
- 3) Find out the distance from the data point to every cluster.

Begin

Initialize c; c' = n; $D_i = \{x_i\}; i = 1, \dots, n$

Do

c' = c' - 1

- 4) Find nearest clusters D_i and D_j
- 5) Merge D_i and D_j

Until c = c'

Return c clusters

End

- 6) To find the nearest clusters in step 4, the following clustering criterion function is used:
 $d_{\min}(D_i, D_j) = \min \|x - x'\|$, where $x \in D_i$ and $x' \in D_j$
- 7) The merging of the two clusters in step 6 simply corresponds to adding an edge between the nearest pair of nodes in D_i and D_j . Also, if instead of terminating after a predetermined number of clusters have been obtained; it is possible to set the termination criteria to stop when the distance between nearest clusters exceeds a predetermined threshold.

B) Apply C5.0 Classification

- 1) For each Clusters C in KKD_i in test data do
 - If C is i1
Ch1=c
 - Else
If C is i2
Ch2=c
 - Else
If C is i3
Ch3=c
 - Else
If C is i4
Ch4=c
 - Else
Ch5=c
 - until end of deta set
- 2) Collect data from dataset in the form of Normal/Abnormal and apply those data to the CHAID Decision Table Majority rule based approach and build condition for the action like training/testing normal data set D.

C) CHAID

- 1) Preparing predictors. The first step is to create categorical predictors out of any continuous predictors by dividing the respective continuous distributions into a number of categories with an approximately equal number of observations. For categorical predictors, the categories (classes) are "naturally" defined.
 - If (c is not equal to ch1,ch2,ch3,ch4)
 - Then
c is Normal
 - Otherwise

c is abnormal

III. RESULTS ANALYSIS

Result Analysis: we are using java implementation to present an evaluation system. For timing evaluation of the suggested technique, it is necessary to describe the detailed evaluation method. Here we are taking only one evaluating modes to find Intrusion Detection system impact on time consuming of selected technique. For experiment use a laptop Pentium® Dual-Core CPU T4400 @2.20Ghz and 32-bit operating system, in which performance data is collected. In the experiments, the laptop executes fixed record data sets (182679). Several performance metrics are collected:

- Execution time
- CPU Utilization time
- Memory Utilization

The execution time is measured the time that an technique takes to produce results. Throughput is calculated through execution time the It proved the speed of technique. The memory deals with the quantity of required memory storage space for the whole process of IDS. The CPU Utilization can be calculated that a CPU is dedicated only to the meticulous method of calculations. It calculates the load of the CPU. During Results evolution we have use the KDD99 cup data set [22, 23 & 24] for training and testing [1] which is shown in table 1 and 2. In 1998 DARPA intrusion detection evaluation program was set up to acquire raw TCP/IP dump data [21 & 22] for a LAN by MIT Lincoln lab to compare the performance of various intrusion detection methods [5 & 6]. In KDD-99 data set each record is consists of a set of features, some of which are either discrete or continuous. The qualitative values are labels without an order which could be symbolic or numeric values e.g. the value of feature protocol type is one among the symbols {icmp, tcp, udp}. The numeric value of the feature logged in is 0 or 1 to represent whether the user has successfully logged in or not. For the quantitative attributes, the data are characterized by numeric values within a finite interval. Example can be the duration. Since the feature selection is applicable only to the discrete attributes, not to the continuous ones, the continuous features need be converted to discrete ones prior to the feature selection analysis. In order to evaluate the performance of this method we have used KDD99 data set [27].

First apply K-means clustering hierarchical clustering algorithm on the features selected. After that, we classify the obtained data into Normal or Anomalous clusters by using the Hybrid classifier which is the combination of (C5.0 Classification and CHAID). In these experimental results compare packet performance, time-consuming, memory utilization and CPU utilization of known algorithm on fixed size of record sets. During processing, the record sets are coming from data base, table 1 is producing training data set and table 2 is producing testing data set. For evaluation mode, there are two parameters: the number of evaluated record set and the size of evaluated record set, where the number of evaluated record sets is the number of record set that are generated randomly and the size of evaluated record sets can be chosen from database. In this mode, n cycles (that is, the number of the evaluated record sets) executed. In each cycle, record sets are respectively executed by proposed technique. Finally, the outputs of the Proposed evaluation system are packet performance, execution time, and the execution time is measured in seconds. Actually, for an algorithm, the time-consuming of execution not only depends on the algorithm's complexity, but also the size of record sets. The evaluated results are illustrated as in Table 3 – 5.

Table 1: Number of Example used in Training Data Taken from KDD99 Data Set

Attacks Type	Training Example
Normal	170737
Remote to User	2331
Probe	7301
Denial of service	2065
User to Root	245
Total examples	182679

Table 2: Number of Example used in Testing Data Taken from KDD99 Data Set

Attacks Type	Testing Example
Normal	78932
Remote to User	1015
Probe	4154
Denial of service	885
User to Root	145
Total examples	85131

The execution time is considered the time that an algorithm takes to produce results. Execution time is used to calculate the throughput of an algorithm. It indicates the speed of algorithm. Table 3 is showing the execution time of proposed technique on 85131 testing data set.

Table 3: Comparison of Execution Time on 85131 Data Volume

Data Volume	Proposed Hybrid Technique(Hierarchical + C5.0+ CHAID)
	Execution Time in Millisecond (Approx)
85131	1217

The memory deals with the amount of memory space it takes for the whole process of Intrusion Detection System. Table 4 is showing the memory utilization of proposed technique on 85131 testing data set.

Table 4: Memory Utilization

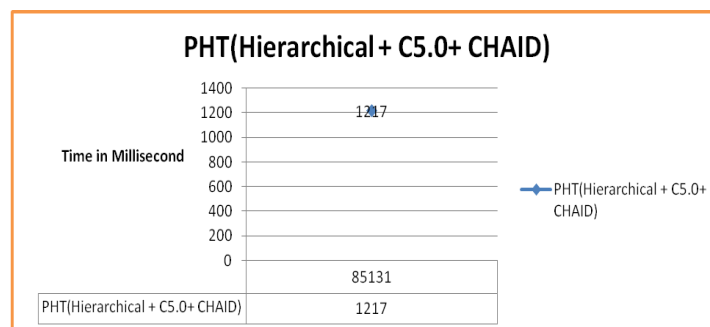
Name	Total Available Memory	Total Memory Consumption	Memory Utilization in %
Proposed Hybrid Technique(Hierarchical + C5.0+ CHAID)	173265	1322	57

The CPU Utilization is the time that a CPU is committed only to the particular process of calculations. It reflects the load of the CPU. The more CPU time is used in the execution process, the higher is the load of the CPU. Table 5 is showing the CPU utilization of proposed technique on 85131 testing data set.

Table 5: of CPU Utilization

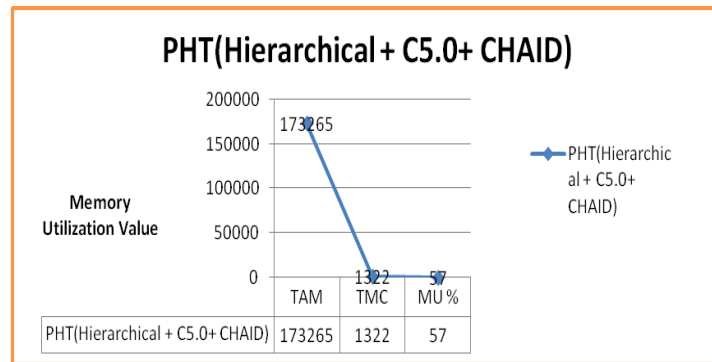
Name	CPU Utilization in %
	(Approx)
Proposed Hybrid Technique(Hierarchical + C5.0+ CHAID)	6%

Here graph-1 is drawing form Table-3 to reveal it. In this graph, execution time is showing where the evaluated mode is fixed size of record sets ranging from 85131 approx testing record sets.



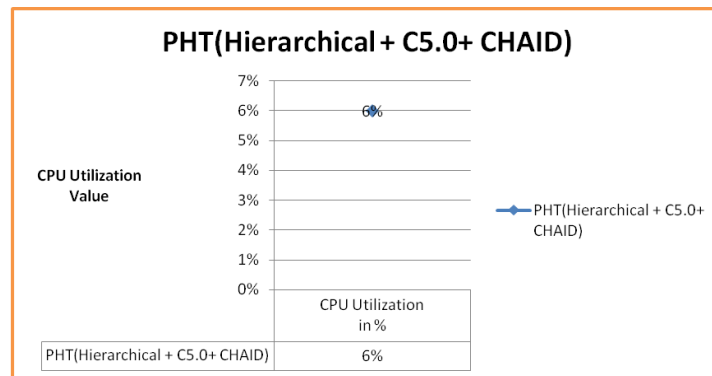
Graph 1:- Execution Time vs User Load of proposed technique on 85131 testing data set

Here graph-2 is drawing forms Table-4 to reveal it. In this graph memory utilization is showing where the evaluated mode is fixed size of record sets (85131). TAM: Total Available Memory, Total Memory Consumption, MU: Memory Utilization, PHT: Proposed Hybrid Technique



Graph 2:- Memory Utilization of proposed technique and on 85131 testing data set

Here graph-3 is drawing forms Table-5 to reveal it. In this graph CPU utilization is showing where the evaluated mode is fixed size of record sets (85131).



Graph 3: CPU Utilization of proposed technique and existing technique on 85131 testing data set

Experimental results for this comparison point are shown Table 3 to 5 at execution stage. The results show the superiority of proposed technique in terms of the processing time, Memory Utilization and CPU Utilization. Some typical results obtained by the evaluation system can be found in Tables (3, 4 & 5) and Graphs (1, 2 & 3). The results illustrated in Table 3 shows that proposed technique is in different/fixed record sets. Finally, it is not difficult to find that, in contrast with these Tables, the larger the data record sets, the bigger execution time is. Besides, in contrast with these Tables, it is not difficult to find that the increasing data length can lead to the significant increment of execution time as well as memory utilization and CPU Utilization. Generally speaking, the time-consuming of known algorithm usually depends on the size of record sets of.

- Proposed Hybrid technique is producing good performance then comparing technique to find normal packet performance.
- Proposed hybrid technique having low response time than comparing technique.
- Proposed hybrid technique using low memory space during execution than the compared technique and easy to understand and implement.
- Proposed hybrid technique used simple structure, control flow is well defined and looping structure is also minimized. Due to the following facts it take very less time for execution.

IV. CONCLUSION

The proposed research have improved detecting speed and accuracy which is the prime concern of the proposed work, and presents more efficient cluster rules mining method with classification method to abnormal detecting experiment based on network. Presented Approach is a hybrid approach which is the combination of K-mean clustering, K-nearest and Decision Table Majority rule based approach. The proposed approach was compared and evaluated on KDD'99 dataset. Considering the dependent relations between alerts, it proposed an

improved cluster Algorithm with k-nearest classification; this hybrid approach can find more accurate probability of normal and abnormal packets. Compared with other method, proposed method can find the probability from the training data as well as testing data with high efficiency. Usually when an attack performed, it is very possible that there exist attack cluster transitions. Based on this it use the cluster sequences to filter false alarms generated by IDS, experimental results proved this method is effective and feasible. Future research work should pay closer concentration or attention to the data mining process that do not fall into the categories feature selection and anomaly detection. To deal with some of the general challenges in data mining, it might be best to develop special-purpose solutions that are tailored to intrusion detection

REFERENCES

- [1] Om, H. and Kundu, A. "A hybrid system for reducing the false alarm rate of anomaly intrusion detection system" Recent Advances in Information Technology (RAIT), 1st IEEE International Conference on 15-17 March 2012 Page(s):131 - 136 Print ISBN:978-1-4577-0694-3.
- [2] P.R Subramanian and J.W. Robinson "Alert over the attacks of data packet and detect the intruders" Computing, Electronics and Electrical Technologies (ICCEET), IEEE International Conference on 21-22 March 2012 Page(s):1028 - 1031 Print ISBN:978-1-4673-0211-1
- [3] V. S. Ananthanarayana and V. Pathak "A novel Multi-Threaded K-Means clustering approach for intrusion detection" Software Engineering and Service Science (ICSESS), IEEE 3rd International Conference on 22-24 June 2012 Page(s): 757 - 760 Print ISBN: 978-1-4673-2007-8
- [4] N.S Chandolikor and V.D.Nandavadekar, "Efficient algorithm for intrusion attack classification by analyzing KDD Cup 99" Wireless and Optical Communications Networks (WOCN), 2012 Ninth International Conference on 20-22 Sept. 2012 Page(s):1 - 5 ISSN :2151-7681
- [5] Virendra Barot and Durga Toshniwal "A New Data Mining Based Hybrid Network Intrusion Detection Model" IEEE 2012.
- [6] Wang Pu and Wang Jun-qing "Intrusion Detection System with the Data Mining Technologies" IEEE 2011.
- [7] Z. Muda, W. Yassin, M.N. Sulaiman and N.I. Udzir "Intrusion Detection based on K-Means Clustering and Naïve Bayes Classification" 7th IEEE International Conference on IT in Asia (CITA) 2011.
- [8] Dewan M.D. Ferid, Nouria Harbi, "Combining Naïve Bayes and Decision Tree for Adaptive Intrusion detection" International Journal of Network Security and application(IJNSA),vol 2, pp. 189-196, April 2010.
- [9] Joseph Derrick,Richard W. Tibbs, Larry Lee Reynolds "Investigating new approaches to data collection,management and analysis for network intrusion detection". In Proceeding of the 45th annual southesast regional conference, 2007. DOI = <http://dl.acm.org/citation.cfm?doid=1233341.1233392>
- [10] M.Panda, M. Patra, "Ensemble rule based classifiers for detecting network intrusion detection", in Int. Conference on Advances in Recent Technology in Communication and Computing, pp 19- 22,2009.
- [11] KDD. (1999). Available at <http://kdd.ics.uci.edu/databases/-kddcup99/kddcup99.html>
- [12] L. Breiman, J.H. Friedman, R.A. Olshen, and C.J. Stone, Classification and regression trees. Monterey, CA: Wadsworth & Books/Cole Advanced Boks & Software, 1984.
- [13] Dewan M.D. Ferid, Nouria Harbi, "Combining Naïve Bayes and Decision Tree for Adaptive Intrusion detection" International Journal of Network Security and application(IJNSA),vol 2, pp.189-196, April 2010.
- [14] Eric Bloedorn, Alan D. Christiansen, William Hill "Data Mining for Network Intrusion Detection: How to Get Started" 2001.
- [15] Fayyad, Piatetsky-Shapiro, Smyth: From Data Mining to Knowledge Discovery in Databases. AI Magazine, 1996.
- [16] Roiger, Richard J.; Geatz, Michael W.: Data Mining: A Tutorial- Based Primer. Addison Wesley, 2003
- [17] MIT linconin labs, 1999 ACM Conference on Knowledge Discovery and Data Mining (KDD) Cup dataset, <http://www.acm.org/sigs/sigkdd/kddcup/index.php?section=1999>

Implementation of a plus shaped fractal antennas for multi-band applications

Maisarla.Chinnayya¹ Valluri.Dhana Raj² Dr.A.Mallikarjuna
Prasad³ Dr.M.Satyanarayana⁴ Dr.G.M.V.Prasad⁵

1, 2,3,4,5 Department of Electronics and Communication Engineering,
1,2 B.V.C.E.C,3 JNTUK,4 MVGR,5 BVCITS

ABSTRACT

Radical changes are taking position in wireless communications technology at a rapid pace to satisfy the current day requirements. Nevertheless the demand for lavishness and mitigated tautness is very much active. An antenna with broader bandwidth, multiband operations, and low profile characteristics are the underlying root of all the modern day demands. Fractal antenna fills this rareness with its unusual attributes of self-similarity and multi-band behavior besides possessing the qualities the features of an ideal antenna. A multi-band antenna can remain applied for operating in more than a single set of frequencies. This singular feature is reinforced using plus shape fractal antenna. This is engaged to supply the needs of the world with its bankable features. Since of its savory properties, it is felt that this report should deal with this fractal type and its cornucopia applications. The main ascendancy of fractal antennas over conventional antennas is shortened the size then multi-band nature. In this paper, the claims and advantages of plus shaped slotted fractal antenna were presented along with their design and radiation properties. It gets its applications in the areas of medicine, military, geology and nevertheless wireless communication. The simulation results are presented using HFSS 13 and verified with a network analyzer.

KEYWORDS: Fractal, HFSS, self-similarity

I. INTRODUCTION

In the modern era, man is the alter ego of luxury. A device supporting WLAN, GPS, GPRS, NFC and many more is the demand for the day. If the antenna is applied for each lineament, the size of the desired device wanted be a perpetuity. Also, the hindrances are single band performances of conventional antenna and dependence between size and functioning frequency. Fractal antenna appeared to be the solution aimed at this requirement. A fractal antenna is an antenna with a self-similar figure to enhance the perimeter of the cloth below the issue of electromagnetic radiations within a given total surface area or bulk is named as fractal antenna. The term fractal, derived from “fractals”, coined by Mandelbrot, entails breaking or irregular fragments. Radiation characteristics are importantly leveraged by the antenna size about the wavelength. For useful results, the size should be in the order of $\lambda/2$ or larger. However, designing with these parameters would deteriorate the bandwidth, efficiency, and profit. Multiband antenna plays a vibrant part.

II. ADVANCEMENTS & USES

Advantages of fractal antennas are more numerous than those of conventional antennas. The main benefit of the former is its multiband behavior at reduced size. On performing iterations on the basic form, one can obtain increased bandwidth and multi-band nature, contributing to improved VSWR and return losses. The simulated and experimental effects are found to be in full accord. The iteration results obtained are very abundant involved in cellular communications. The self-similarity feature would enhance multi-band and ultra-wide band properties of the transmitting aerial. Shrinking of antenna is possible with space-filling property of the fractal antenna. The generous variety of this antenna spreads from the design of MIC components to contemporary day cellular antennas. It can replace the duck antennas in cellular communication. These antennas are also applied to locate oil, identify geologic faults, and possibly predicting earthquakes. Acid rain and erosion can be established by these antennas. The Spring manufacturing uses the fractal geometry to abate the testing period of strings from 3 days to 3 minutes.

III. FRACTAL CONCEPT

Fractal antenna theory, is an allowance of Euclidian geometry, stems from the classical electromagnetic theory. The main properties of this antenna are self-similarity and space-filling. This self-similar nature enables similar surface current distributions for different frequencies, i.e. multiband behavior is got. By way of space filling property increases the electrical length, slenderized size can be obtained at a desired resonant frequency. In conventional microstrip patch antennas, multiband behavior is accomplished by using multiple radiating elements or reactively loaded patch antennas and the same is possible with self-similarity property in case of fractal antennas. These antennas are basically self-loading as inductance and capacitance are added without the utilization of any external components and as a result they consist of various resonant frequencies.

Mathematically a fractal is defined based on a fractal dimension given by

$$D_s = \frac{\ln(N)}{-\ln(\gamma)}$$

, where N is the number of copies of entire object and γ is the scaling factor of each copy

IV. TYPES OF FRACTAL ANTENNAS

The various types of fractal antennas are

Hilbert Curve fractal Dipole: Its chief distinctive is the show of lower resonant frequency than any other antenna of the same proportions.

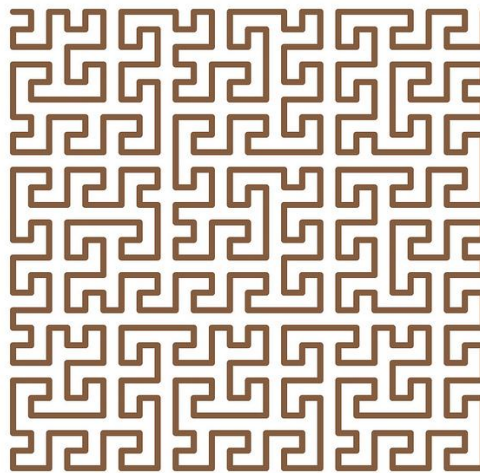


Fig.4.1.Hilber curve Fractal Antenna

4.2 Koch Fractal Monopole: It is a small antenna offering characteristics which no other antenna with the same dimensions could achieve. The fractal dimension of this antenna is $\log 4/\log 3 \approx 1.26$ which is heavier than the dimension of a line but less than Peano's space-filling curve.

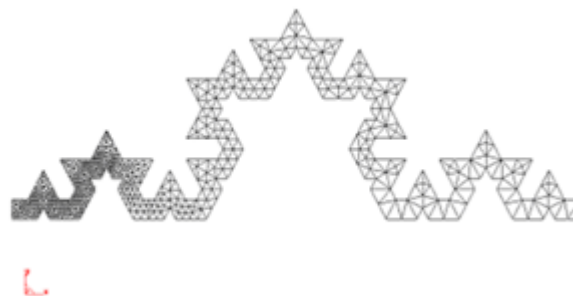


Fig.4.2. Koch Fractal Monopole Antenna

There are also a few other cases like a triangular fractal antenna, plus shape slotted fractal antenna that we are dealing in detail.

TRIANGULAR FRACTAL ANTENNA: The triangular fractal antenna is a good example of a self-similar antenna that shows multi-band behavior. It shows several resonance bands. It has a log-periodic behavior with bands specified by a factor $s=2$ and with a moderate bandwidth of 21%. The antenna is matched at frequencies: $f_n = 0.26 \frac{c}{h} S^n$, where $S=2$ is log-periodic constant, n is a natural number, c is the speed of light in vacuum and h is the height of largest TFA. The stages of expression of a fractal antenna are as indicated in the image. Initially an equilateral triangle and in the next step the center triangle with vertices located at center of the positions of the former triangle are removed. The triangular fractal is generated by holding out this iterative process an infinite number of times.

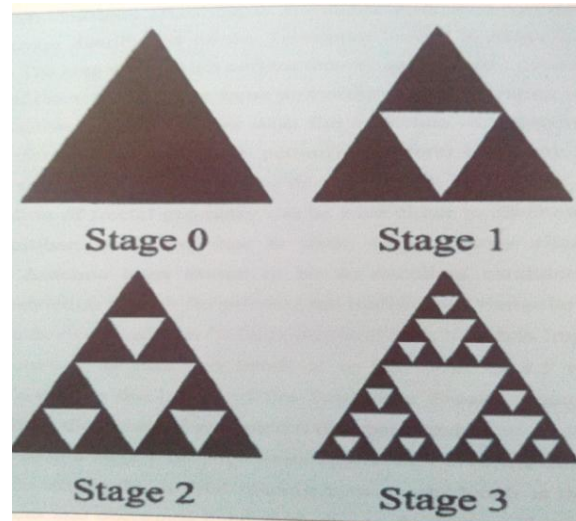


Fig4.3.Triangular fractal antenna

The fractal antenna is envisioned on the FR4 substrate with dielectric constant 4.4 and thickness 1.6 millimeter.

$$f_r = 0.3 \cos(\alpha) \sqrt{\frac{2.5 c}{\epsilon_r h}} S^n$$

Where f_r is a resonant frequency, α is flare angle, ϵ_r is a relative permittivity of the substrate, h is the height of gasket, S is a scale factor, n is iteration

$$l_x = 2h \tan((180-\alpha)/2) \quad \text{and} \quad l_1=l_2 = (h^2 + (a/2)^2)^{1/2}$$

Where l_x is length of the edge opposite the flare angle α and l_1, l_2 are the outer edges

In order to calculate the side of the triangular fractal antenna the following parameters are required

$$C = 3 \times 10^8$$

$$\epsilon_{r,dyn}^* = 4.2 \text{ (FR-4)}$$

$$L_{eff} = (\sqrt{3} \cdot a) / 2$$

$$f_r = 2.4 \text{ GHz}$$

From the above formulae aimed at resonant frequency, the position of the triangle is calculated as $a = 32 \text{ mm}$.

SLOTTED PLUS SHAPE FRACTAL ANTENNA: It is designed based on the fractal concepts for a multiband behavior. A plus shaped patch is removed and is subjected to iterations. Later on each iteration the dimensions decrease to 1/3rd of the base frame. Higher iterations show that the resonant frequencies become lower than those of zero iterations that represent a conventional plus shaped patch. The design specifications are $\epsilon_r = 4.4$ and thickness is 1.6mm. The base antenna is equally indicated in the image.

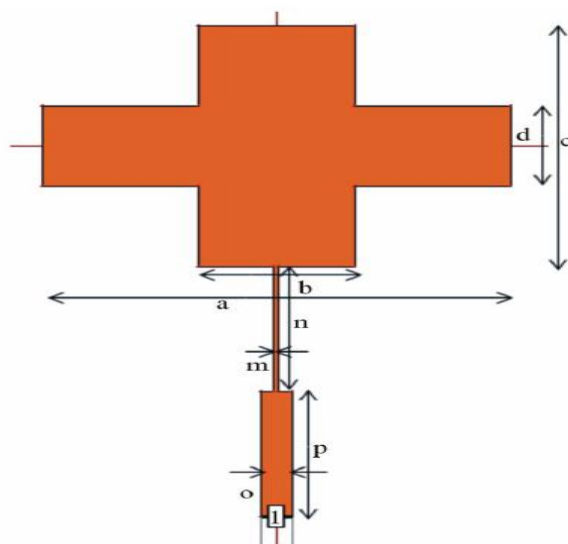


Fig.4. 4.1 1st iteration Plus shaped fractal antenna(PFA)

The first iteration patch is deliberate by four plus shapes of order (1/3) of the improper form are placed touching the foot frame. The same routine is realistic for the iteration 2 where the dimensions are changed as

$$e = (1/9) a \ \& \ g = (1/9) c \ \text{also} \ f = (1/9) b \ \& \ h = (1/9) d. \quad i = (1/9) e \ \& \ k = (1/9) g \ \text{also} \ j = (1/9) f \ \& \ l = (1/9) h$$

Where a, b, c and d are the distances and widths of plus shape in base antenna and e, f, g and h are the distances and widths of plus shapes added to the base antenna and my, j, k and l are the distances and breadths of the plus shapes added to the antenna in the second iteration. So with optimized design the dimensions obtained are a = 45.3 mm, b = 15.1 mm, c = 35.4 mm, d = 11.8 mm. The duration of the slot is $L_s = 21.675$ mm and width of the slot Wise. e. r = 2 mm. The proportion of the ground plan is 55 mm × 85 mm. A 50 ohm SMA connector is utilized to feed the antenna by using microstrip feed technique. Optimized microstrip line with following dimension, m = 0.5 mm, n = 18.55 mm, o = 3.05 mm, p = 18.4 mm. The suitable feed location is received through the optimization process by using the HFSS software.

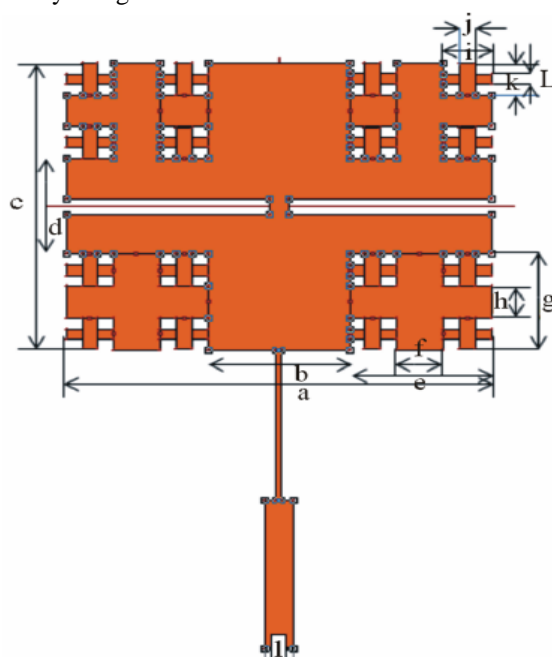


Fig.4.4.2 2nd Iteration PFA

During the first iteration the resonant frequency obtained is 1.27 GHz, which is lower compared to that of 2.199 GHz of the base antenna and when the same antenna is slotted the resonant frequency obtained is 0.99GHz with a phenomenal size reduction of 79.88% and on the second iteration of the same antenna multiple bands are held. It is found that with increasing the slot length starting from the sharpness of the patch, resonant frequency decreases.

V. GENERAL PROCEDURE FOR DESIGN OF MICROSTRIP FED COPLANAR ANTENNA:

Step1: Take any substrate with thickness h and relative dielectric constant ϵ_r and calculate the width (w_1) of the microstrip transmission line for 50Ω characteristic impedance.

Step2: The width of the center strip (w) calculated using the following equation

$$w = \frac{c}{2f_2\sqrt{\epsilon_{reff}}}$$

Where

c is the velocity of light and

f_2 is the second resonant frequency.

So the field components are not restricted to the substrate alone the effective dielectric constant) has to be applied instead of relative permittivity of the substratum substrate.

$$\epsilon_{reff} = \frac{\epsilon_r + 1}{2}$$

Step3:

The distance of the three rectangular strips is then counted as

$$l = \frac{0.15c}{f_1\sqrt{\epsilon_{reff}}}$$

Where $f_1 = 1^{\text{st}}$ resonant frequency

Step4:

Width of the lateral conductors (C) is obtained using the equation given below.

$$C = \frac{c}{f_1\sqrt{\epsilon_{reff}}} - \left(\frac{4l + 2h + w}{2}\right)$$

When h = thickness of the dielectric substrate.

Step5:

Gap separating center strip from the lateral strips is then computed

$$g = \frac{0.014c}{f_1\sqrt{\epsilon_{reff}}}$$

Where c = velocity of the electromagnetic signal in the free place

Step6:

Ground plane dimensions are calculated using the following equations.

$$w = \frac{0.98c}{f_1\sqrt{\epsilon_{reff}}}$$

$$L = \frac{0.12c}{f_1\sqrt{\epsilon_{reff}}}$$

0.12 And 0.98 are the constants that are derived empirically after studying the issue of the ground plane on the two resonant frequencies.

Step7: The two extreme corners of the lateral conductors are connected to the ground plane of the microstrip line using visas or conducting pins.

VI. SIMULATION OF PLUS SHAPED SLOTTED FRACTALLY ANTENNA

Plus shaped slotted fractal antenna (1st iteration) the simulation results obtained on the first iteration are

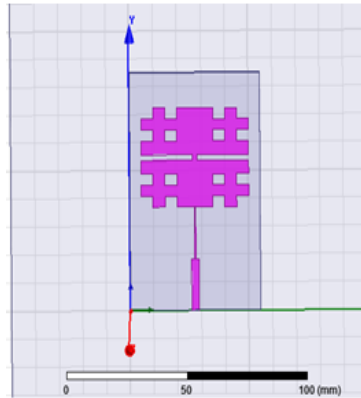


Figure 6.1.1: HFSS pattern of 1st iteration on plotting its response the following graphs are obtained

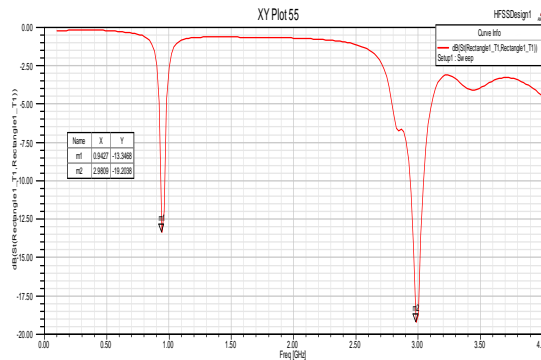


Figure 6.1.2: the Return Loss curve of 1st iteration

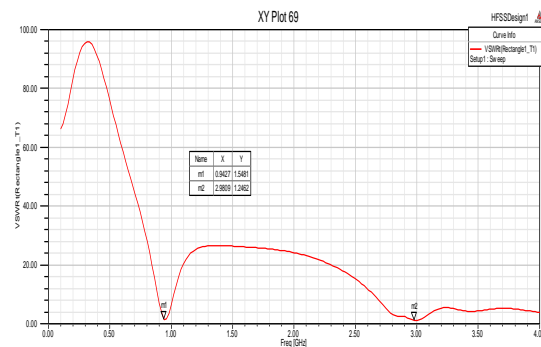


Figure 6.1.3: VSWR curve of 1st iteration

The antenna has resonating frequencies at 0.94GHz and 3GHz, and the return losses are -13.5 and -19 at these frequencies respectively, where the VSWR obtained is between 1 and 2 at both frequencies.

Simulated Plus shaped slotted fractal antenna (2nd iteration). The simulation results obtained on 2nd iteration are

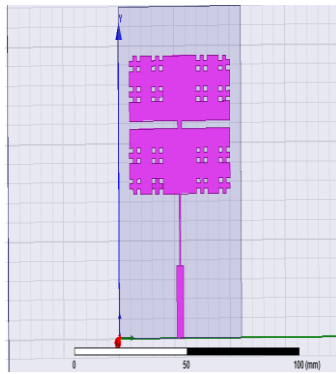


Figure 6.2.1: HFSS pattern of 2nd iteration PFA

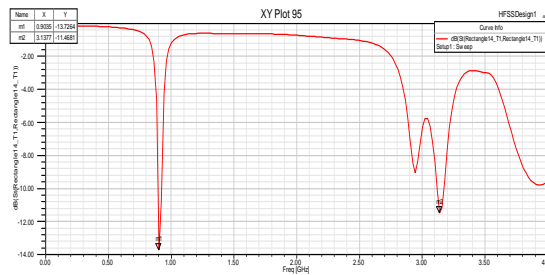


Figure 6.2.2: the Return Loss curve of 2nd iteration

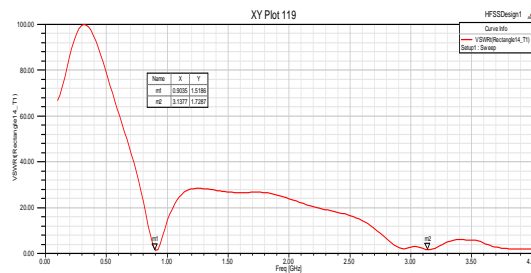


Figure 6.2.3: VSWR curve of 2nd iteration

The antenna resonates at frequencies 0.9GHz and 3.13GHz, which is dual band and the VSWR obtained at these frequencies is found to be between 1 and 2 and the return losses are -13.76 and -11.46 respectively.

The outcomes found when physically tested on a vector network analyzer are



Figure 6.2.4: Fabricated antenna on 2nd iteration

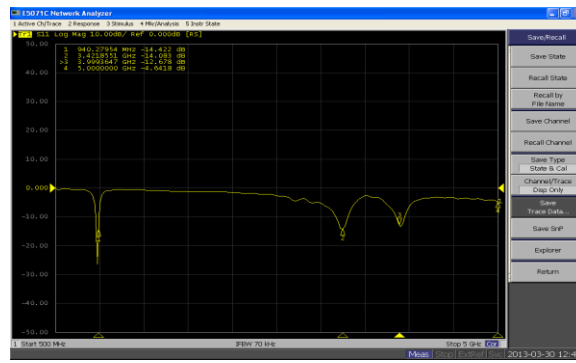


Figure 6.2.5: Return loss curve of the 2nd iteration



Figure 6.2.6: VSWR curve of the 2nd iteration

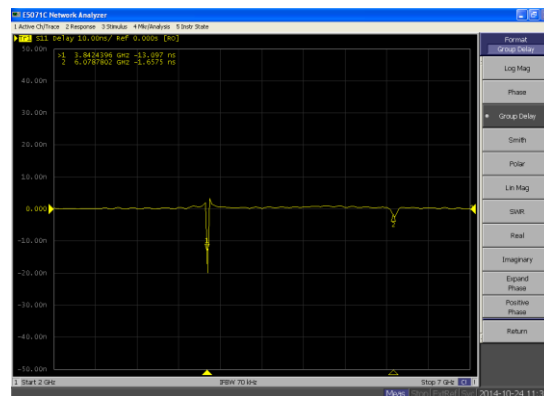


Figure 6.2.7: Group delay curve of the 2nd iteration



Figure 6.2.8: Phase plot of the 2nd iteration

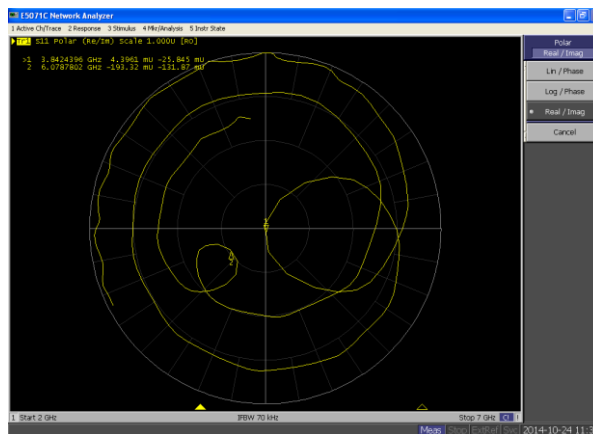


Figure 6.2.9: polar plot of the 2nd iteration

VII. RESULT ANALYSIS

Plus shaped slotted fractal antenna: The PFA acts as a dual band antenna resonated at two different groups 0.94GHz and 3GHz and the experimentation results of 1GHz, 2.94GHz and 3.12GHz. Details of the simulated and experimental results were exhibited below:

Table 9.1: Results obtained for the antennas

S.no	Parameter	Plus the shaped fractal antenna	
		1 st iteration	2 nd iteration
1.	Return losses at 1 st resonant frequency	-13.5db at 0.94GHz	-13.6db at 0.9GHz
2.	Return losses at 2 nd resonant frequency	-19db at 3GHz	-11.6db at 3.13GHz
3.	VSWR at 1 st resonant frequency	1-2 at 0.94GHz	1-2 at 0.94GHz
4.	VSWR at 2 nd resonant frequency	1-2 at 3GHz	1-2 at 3.13GHz
5.	% Bandwidth At 1 st resonant frequency	3.53%	3.7%
6.	% Bandwidth at 2 nd resonant frequency	3.69%	1.7%

VIII. CONCLUSIONS

As per the simulation and experimental results obtained the proposed plus shaped antenna exhibited the multiband nature, The plus shaped slotted fractal antenna resonated at 0.94 GHz, 3.43GHz and 4GHz on 2nd iteration. Hence, the proposed antennas can find the application in wireless communication systems where size reduction is one of the key factors. Further, the number of iterations are increased to meet the wireless standard requirements. Fractal antennas also decrease the area of a resonant antenna, which could lower the radar cross-section (RCS). These benefits can be exploited in military applications where the RCS of the antenna is a very crucial parameter.

REFERENCES

- [1] Hary Breed, 2009, "The Fundamentals of Patch Antenna Design and Performance", High Frequency Electronics, Summit Technical Media, LLC
- [2] Douglas H. Werner and Suman Ganguly, "An Overview of Fractal Antenna Engineering Research," IEEE, Antennas and Propagation Magazine, Vol.45, No.1, 2003, 38-57
- [3] K. Sing, V. Grewal and R. Saxena, "Fractal Antennas: A Novel Miniaturization Technique for Wireless Communications," International Journal of Recent Trends in Engineering, Vol. 2, No. 5, 2009, pp. 172-176.
- [4] F. J. Jibrael and M. H. Hammed, "A New Multiband Patch Microstrip Pluses Fractal Antenna for Wireless Applications," ARPN Journal of Engineering and Applied Sciences, Vol. 5, No. 8, 2010, pp. 155-158.
- [5] Vinay. K J., "Fractal shaped antenna elements for wide and multi-band wireless applications Thesis, Pennsylvania, Aug. 2002.
- [6] Greg. Bhatia, Bahl, Ittipiboon, "Microstrip Antenna Design Handbook", ArtechHouse, London, 2000.
- [7] R. Kumar and P. Malathi, "Design of CPW –Fed Ultra-wideband Fractal Antenna and Backscattering Reduction", Journal of Microwaves, Optoelectronics and Electromagnetic Applications, Vol. 9, No. 1, pp. 10-19, June 2010

Facial Expression Recognition System: A Digital Printing Application

Mahasweta Mandal¹, Somnath Banerjee²

¹ Department of Printing Engineering, Jadavpur University, India

² Department of Computer Science and Engineering, Jadavpur University, India

ABSTRACT:

Human Computer Interaction (HCI), an emerging field of research in science and engineering, is aimed at providing natural ways for humans to use computers as aids. Humans prefer to interact with each other mainly through speech, but also through facial expressions and body gestures, to emphasize a certain part of that speech and display of emotions. The identity, age, gender, as well as the emotional state of a human being can be acquired from his/her faces. The impression that we receive from a reflected expression on face affects our interpretation of the spoken word and even our attitude towards the speaker himself. Although emotion recognition is seemingly an easy task for humans, it still proves to be a tough task for computers to recognize the user's state of emotion. Progress in this field promises to equip our technical environment with means for more effective interaction with humans and hopefully, in the days ahead, the influence of facial expression on emotion recognition will grow rapidly. The application of digital printing has rapidly grown over the past few years with substantial developments in quality. Digital printing has brought about fast turnaround times and printing on demand in terms of cost. In this paper, we describe the empirical study of the state-of-the-art classifier combination approaches, namely ensemble, stacking and voting. Each of these three approaches was tested with Naïve Bayes (NB), Kernel Naïve Bayes (k-NB), Neural Network (NN), auto Multi-Layer Perceptron (auto MLP) and Decision Tree (DT). The main contributions of this paper is the enhancement of classification accuracy of the emotion recognition task on facial expressions. Our person-dependent and person-independent experiments show that using these classifier combination methodologies provide significantly better results than using individual classifiers. It has been observed from the experiments that overall voting technique with majority voting achieved best classification accuracy.

KEYWORDS: Human Computer Interaction, facial emotion recognition, facial expressions, facial action coding system, classifier combination, facial features, AU-Coded facial expression, CK+ database, digital printing.

I. INTRODUCTION

Human beings can express their emotion through voice, body gestures and facial expression. But the most expressive way a human being displays his/her emotional state is through facial expressions. Facial expressions are the facial changes in response to a human being's internal emotional states, intentions, or social communications. Face is the primary signal system to show the emotion of a person. Face recognition and automatic analysis of facial expressions are one of the most challenging research areas in the field of Human-Computer Interaction (HCI) and have received a special importance. In the 1990s, there has been growing interest to construct automatic methods of recognizing emotions from facial expressions in images or video. Emotion as a private state is not open to any objective observation or verification. So, the recognition of the emotional state of a person is really a challenging issue. Relativity, categorization and identification of emotion are three crucial factors in emotion analysis. The relativity factor of emotion depends on the person's facial expression or state of mood whereas other two factors are comprehensible but require high technical affluence of computer intelligence. In recent years, computers and automated processing have had a considerable influence on prepress. The integration of prepress and press, as well as automation in printing and the integration of related processes, have also reached a certain maturity. The use of digital printing applications such as advertising, photos, architectural design etc. and integration of these applications into traditional print markets is rapidly expanding.

Emotion is the realm where thought and physiology are inextricably entwined, and where the self is inseparable from individual perceptions of value and judgment toward others and us. In the last few years, automatic emotion recognition through facial expression analysis has been used in developing various real life applications such as security systems, computer graphics, interactive computer simulations/designs, psychology and computer vision. In psychology, emotion is often defined as a complex state of feeling that results in physical and psychological changes that influence thought and behavior. Our emotions are composed of three critical components: a subjective component (how we experience the emotion), a physiological component (how our bodies react to the emotion), and an expressive component (how we behave in response to the emotion). These different elements can play a role in the function and purpose of our emotional responses.

There are a lot of words for the message persons get from the face (afraid, terrified, horrified, apprehensive, worried, to mention a few of those related to fear), but few to describe the source of those messages. Human beings do have the terms smile, grin, frown, squint, but there are relatively few such words that identify particular facial configurations, distinctive wrinkle patterns, or temporary shapes of the facial features. Without terms to refer to the face human beings are incapable in comparing or correcting their interpretations of facial expression. According to Ekman and Friesen [21], the face gives more than one kind of signal to convey more than one kind of message. Sometimes the people can't differentiate the emotion messages from the other messages conveyed by the face. The face provides three types of signals: static (such as skin color), slow (such as permanent wrinkles), and rapid (such as raising the eyebrows). The static signals include many more or less permanent aspects of the face like skin pigmentation, coloration, the shape of the face, bone structure and the size, shape and location of the facial features (brows, eyes, nose, mouth). The slow signals include changes in the facial appearance which occur gradually with time and in addition to the development of permanent wrinkles, changes in muscle tone, skin texture and even skin, coloration occur with age. The rapid signals are produced by the movements of the facial muscles, resulting in temporary changes in facial appearance, shifts in the location and shape of the facial features and temporary wrinkles. These changes have been occurred on the face for a matter of seconds or fractions of a seconds. All three types of facial signals can be modified or disguised by personal choice, although it is hardest to modify the static and slow signals. So one can be misled, intentionally or accidentally, by rapid, slow or static signals. The face is not just a multi-signal system (rapid, slow, static) but also a multi-message system. In order to describe the emotion, it is referred to transitory feelings such as fear, anger, surprise, happiness etc. When these feelings occur, the facial muscles contract and visible changes are appeared on the face. Scientists have found that accurate judgments of emotion can be made from the rapid facial signals. It is important to note that the emotion messages are not transmitted by either the slow or the static facial signals; however these may affect the implications of an emotion message. Sometimes the facial expression analysis has been confused with emotion analysis in the computer vision domain. For emotion analysis, higher level knowledge is required. For example, although facial expressions can convey emotion, they can also express intention, cognitive processes, physical effort, or other intra- or interpersonal meanings. Computer facial expression analysis systems need to analyze the facial actions regardless of context, culture, gender, and so on. In regard to facial expressions of emotion we should have a higher knowledge on rapid facial signals and their distinctive messages.

II. MOTIVATION AND RELATED WORK

Facial expression is one of the most significant ways for human beings to communicate their emotions and intentions. The face can express sooner than people verbalize or even realize their feelings. Since the mid of 1980s a remarkable novelty has been brought to build computer system to understand and use the natural form of human communication. There are lot of praiseworthy researches have been carried out in this Human-Computer Interaction (HCI) field during last decades. In recent years, the developments in HCI have abetted the user to interact with the computer in novel ways beyond the traditional boundaries of the keyboard and mouse. This emerging field includes areas, such as computer science, engineering, psychology and neuroscience. As facial expressions provide important clues about emotions, several approaches have been *envisaged* to classify human affective states. Facial expressions are visually observable, conversational, and interactive signals that regulate our interactions with the environment and other human beings in our vicinity [3]. Therefore, behavioural research, bimodal speech processing, videoconferencing, face/visual speech synthesis, affective computing and perceptual man-machine interfaces are those principle driving applications that have lent a special impetus to the research problem of automatic facial expression analysis and produced a great number of interests in this research topic. In 1872, Darwin [1] took attention by firstly demonstrating the universality of facial expressions and their continuity in human beings and animals. He claimed that there are specific inborn emotions, which originated in serviceable associated habits. He also explained that emotional expressions are closely related to survival. In 1971, Ekman and Friesen [4] classified human emotion into six archetypal emotions: surprise, fear, disgust, anger,

Happiness, and sadness. These prototypic emotional displays are also referred to as basic emotions. Ekman and Friesen [2,13] also developed the *Facial Action Coding System* (FACS) for describing facial expressions by *action units* (AUs). Their work helped to attract the attention of many researchers to analyze facial expressions by means of image and video processing. By tracking facial features and measuring the amount of facial movement, they tried to categorize different facial expressions. Recent works on facial expression analysis and recognition [9, 15, 17, 18, 19,20] used these universal “*basic expressions*” or a subset of them. Suwa et al. [5] presented a preliminary investigation on automatic facial expression analysis from an image sequence. Being motivated by some psychological studies,

De Silva et al.[6] carried out experiments on 18 people to recognize emotion using visual and acoustic information separately from an audio-visual database recorded from two subjects. They claimed that sadness and fear emotions are being better identified with audio, and some emotions, e.g., anger and happiness, are better identified with video. Furthermore, Chen et al.[7] cited the use of audio visual information in a multimodal HCI scenario for computers to recognize the user’s emotional expressions. He concluded that the performance of the system increased when both modalities were considered together. The features are taken typically based on local spatial position or displacement of specific points and regions of the face, unlike the approaches based on audio, which use global statistics of the acoustic features. Pantic [8] explored the complete review of recent emotion recognition systems based on facial expressions. He strongly argued to include the essence of emotional intelligence into HCI design in the near future so that the system could be able to recognize a user’s affective states—in order to become more human-like, more effective, and more efficient. Moreover, he provided new techniques for developing the initial phase of an intelligent multimodal HCI—an automatic personalized analyser of a user’s nonverbal affective feedback.

Mase [9] developed an emotion recognition system based on the major directions of specific facial muscles. He was one of the first to introduce image processing techniques to recognize facial expressions. He used optical flow to estimate facial muscle actions which can then be recognized as facial expressions in both a top-down and bottom-up approach. In both approaches, the objective was on computing the motion of facial muscles rather than of facial features. Facial expressions are the result of facial muscle actions which are triggered by the nerve impulses generated by emotions. The muscle actions cause the movement and deformation of facial skin and facial features such as eyes, mouth and nose. As the texture of a fine-grained organ of facial skin has helped in extracting the optical flow, muscle actions has been extracted from external appearance. By the use of K-nearest neighbor for classification, four emotions, namely: happiness, anger, disgust and surprise have been recognized with an accuracy of 80%. Yacoob et al. [10] proposed a similar approach for analyzing and classifying facial expressions from optical flow based on qualitative tracking of principle regions of the face and flow computation at high intensity gradients points. Instead of using facial muscle actions, they constructed a dictionary to convert local directional motions associated with edge of the mouth, eyes and eyebrows into a linguistic, per-frame, mid-level representation. The main goal of this approach was to develop computational methods that relate such motions as cues for action recovery. Face region motion refers to the changes in images of facial features caused by facial actions corresponding to physical feature deformations on the 3-D surface of the face.

Rosenblum et al. [19] also computed optical flow of regions on the face, then applied a radial basis function network architecture that learned the correlation between facial feature motion patterns and human emotions. This architecture was specially invented to classify expressions. Besides, Lanitis et al. [20] invented a flexible shape and appearance model for image coding, person identification, pose recovery and facial expression recognition. Black et al. [15] developed a mid-level and high-level representation of facial actions using parametric models to extract the shape and movements of the mouth, eye and eyebrows. This approach is also recommended in [10] with 89% of accuracy. Tian et al. [16] obtained 96% accuracy using permanent and transient facial features such as lip, nasolabial furrow and wrinkles. They also used geometrical models to locate the shapes and appearances of those features. In this study the objective was to recognize the AU, developed by Ekman and Friesen [2]. Essa et al. [17] introduced a system that quantified facial movements based on parametric models of independent facial muscle groups and achieved 98% accuracy. They invented spatial-temporal templates that were used for emotion recognition. In this study, the face was being modelled by the use of an optical flow method coupled with geometric, physical and motion-based dynamic models. Matsuno et al. [22] described an approach for recognizing facial expressions from static images focusing on a pre-computed parameterization of facial expressions. Their approach plotted a grid over the face and warped it based on the gradient magnitude using a physical model. In that model, the amount of wrapping was represented by a multi-variate vector which was different than a learned vector of four facial expressions (i.e., happiness, sadness, anger and surprise)

Sebe et al. [11] recommended a method introducing the Cauchy Naive Bayes classifier which used the Cauchy distribution as the model distribution for recognizing emotion through facial expressions displayed in video sequence. Their person-dependent and person-independent experiments showed that the Cauchy distribution assumption typically produced better results than Gaussian distribution assumption. They used the simplified model proposed by Tao and Huang [12] which took an explicit 3D wireframe model of the face. The face model consisted of 16 surface patches embedded in Bezier volumes. The wireframe model and the 12 facial motion measurements were being measured for facial expression recognition. The 12 features have been used to measure the facial motion in the face model and using these features the 7 basic classes of facial expression have been defined for classification.

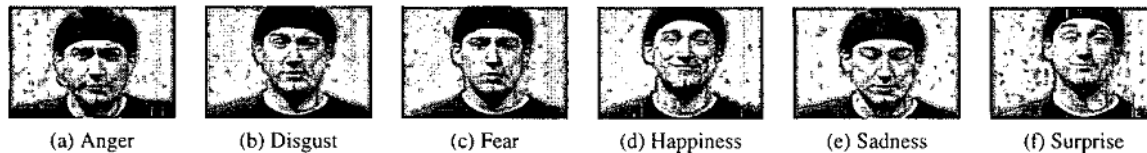


Figure 1.1: Examples of images from the video sequences used in the experiment

Sebe et al. [11] also demonstrated that reduction of the emotion recognition problem to a mood recognition problem might increase the classification results significantly higher. After proposing Cauchy Naive Bayes classifier, Ira Cohen et al. [14] approached a Tree-Augmented-Naive Bayes (TAN) classifier for recognizing emotions through facial expressions displayed in video sequences. The reason behind the introduction of TAN classifier was to learn the dependencies between the facial features. It has been observed from the person-dependent and person-independent experiments that TAN structure provided significantly better outcome than that of simpler NB-classifier.

In the last few years, automatic emotion recognition through facial expression analysis has been used in developing various real life applications such as security systems, computer graphics, interactive computer simulations/designs, psychology and computer vision. Though many researchers employed machine learning classifiers (e.g., Cauchy-Gaussian assumption and support vector machine) independently to recognize emotion state on facial expression analysis, but the proposed method adopted classifier combination methodology. To the best of our knowledge, classifier combination methods were not used yet by any researcher in emotion classification task. So, we employed the classifier combination methodology to enhance the accuracy of emotion classification task.

III. FEATURES SET

Features are basically function or properties of some variable. Feature classification is to classify the features into classes for our purpose that may be our target class or noisy class. Efficient measurement of facial expression is necessary to understand the functionality of face-to-face communication. Most of the studies on automated expression analysis focus on classification of basic expressions (i.e., joy, fear, sadness, disgust, surprise, and anger) [23]. Suitable features selection is necessary to accomplish this classification task. We have used action unit, landmark, intensity and their combination as features in our experiment.

Action Unit

Action Units (AUs) are the fundamental actions of individual muscles or groups of muscles. AUs represent the muscular activity that produces facial appearance changes defined in Facial Coding System by Ekman and Friesen [2]. The reason behind in using the term AU is that more than one action have been separated from what most anatomists described as one muscle.

Landmark and Intensity :Landmark is one of the important features used in this experiment. It has been used in CK+ database invented by Cohn et al. [25]. The similarity normalized shape, denoted by s_n , refers to the 68 vertex points for both the x and y coordinates. The 68 vertices produce a raw 136 dimensional feature vector. These points are the vertex locations after removing all the rigid geometric variation (translation, rotation and scale), relative to the base shape. The similarity normalized shape s_n can be obtained by synthesizing a shape instance of s , that ignores the similarity parameters p . FACS provides a description of all possible and visually detectable facial variations in terms of 44 Action Units (AUs). Usually, a trained human FACS coder identifies the occurrence of an action unit and codes its intensity in a given facial image. Although the FACS coding is a precise tool for studying facial expressions, it is labor intensive. Therefore, automating the FACS coding and measuring the intensity of AUs would make it easier and widely accessible as a research tool in behavioral science. Generally intensities of AUs are measured from absent to maximal appearance using a six-point intensity metric (i.e., 0 to 5).

IV. DATASET

The *Cohn-Kanade*¹AU-Coded Facial Expression Database is publicly available from Carnegie Mellon University. CK database was invented for the purpose of promoting research into automatically detecting individual facial expressions in 2000. Since then, the CK database has become one of the most widely preferred test-beds for algorithm development and evaluation. During this period, three following limitations have been clearly seen:

- While AU codes are well validated, emotion labels are not, as they refer to what was requested rather than what was actually performed,
- The lack of a common performance metric against which to evaluate new algorithms, and
- Standard protocols for common databases have not emerged.

The cumulative effect of these factors has made benchmarking various systems very difficult or impossible. This is highlighted in the use of the CK database [24], which is among the most widely preferred corpus for developing and evaluating algorithms for facial expression analysis. It contains image sequences of facial expressions from men and women of varying ethnic backgrounds. Each subject (resolution 640 X 480) was instructed to perform a series of 23 facial displays that include single action units and combinations of action units. A total of 504 sequences are available for distribution in this database. After development of *Extended Cohn-Kanade database* (CK+) the number of sequences and the number of subjects are increased by 22% and 27% respectively. Emotion expressions included happy, surprise, anger, disgust, fear, and sadness. Examples of the expressions are shown in Fig. 4.3.



Fig.4.3. Cohn-Kanade AU-Coded Facial Expression database. Examples of emotion-specified expressions from image sequences.

In the present work, CK+ image database used as corpus. In CK+ database each set consists of sequences of image of a subject (i.e., man/woman). During person dependent experiment, each of the sets was used separately. However in person independent experiment, the image database was divided into two parts: the first part, which was used as training, contains the 70% of the entire dataset and the second part, which was used as testing, contains 30% of the entire dataset.

V. PREPARING TRAINING MODELS

Many researchers investigated the technique of combining the predictions of multiple classifiers to produce a single classifier (Breiman, 1996c; Clemen, 1989; Perrone, 1993; Wolpert, 1992). The resulting classifier is generally more accurate than any of the individual classifiers making up the ensemble. Both theoretical (Hansen and Salamon, 1990; Krogh and Vedelsby, 1995) and empirical (Hashem, 1997; Opitz and Shavlik, 1996a, 1996b) researches have been carried out successfully. Two sets of experimentation were carried out: person dependent and person independent facial emotion recognition. Thus two different sets of training models were prepared and tested. Altogether sixty three classifier combination models, namely ensemble,

¹ http://vasc.ri.cmu.edu/idb/html/face/facial_expression/index.html

stacking and voting were prepared for the identification of person independent facial emotions. During experimentations, the features were added in incremental fashion. First AU feature was used to train model. Then intensity and landmark features were added gradually to train. The training models preparation for person dependent and person independent task is same except the size of the training data. So the following four sub-sections describe the training models preparation for both cases.

Models using Individual Classifiers : Initially the five classifiers- NB, k-NB, NN, auto MLP and DT were trained individually with the gradually incremented feature set, i.e., first they were trained with AU feature only; then they were trained with AU and intensity features; and finally they were trained with AU, intensity and landmark feature set.

Models using Classifiers Combination : This section describes the empirical study of the state-of-the-art classifier combination approaches, namely ensemble, stacking and voting. Each of these three approaches was tested with Naïve Bayes (NB), Kernel Naïve Bayes (k-NB), Neural Network (NN), auto Multi-Layer Perceptron (auto MLP) and Decision Tree (DT). The previous work [11][14][19] on facial emotion identification used these classifiers independently. In this work, the five classifiers were used to establish the effect of combining models. The following sections report the experimentations and obtained results.

Training Ensemble Models : Two popular methods for creating accurate ensembles are- bagging (Breiman, 1996c) and boosting (Freund and Schapire, 1996; Schapire, 1990). These methods rely on resampling techniques to obtain different training sets for each of the classifiers. Bagging approach was applied separately to five base learners, namely NB, k-NB, NN, auto MLP and DT. Initially the size (number of iteration) of the each base learner is set to 2. Then the experiments were performed with gradually increased size (size > 2). It has been observed that initially the classification accuracy is increased with increasing in size parameter, but after a certain size value, the accuracy is almost stable. Cross validation technique was used to set the suitable size for base learners. Table-5.1 reported the suitable size of the base learners, i.e., NB, k-NB, NN, auto MLP and DT. It can be noticed from Table 5.1 that bagging using NN and auto MLP classifiers require less iterations than that of other classifiers, i.e., NB, kNB and DT.

Table –5.1: Size variation in Bagging

Base Learners	Size		
	AU	AU+INT	AU+INT+LM
NB	18	15	13
kNB	20	17	15
DT	15	12	10
Auto MLP	12	10	8
NN	12	9	7

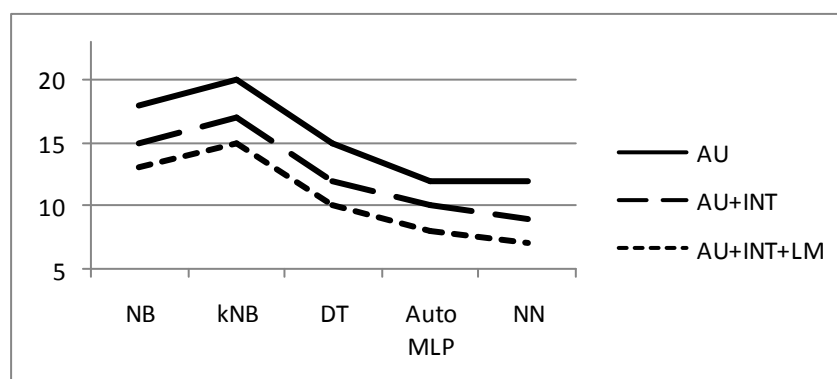


Fig. 5.1: Size variation in Bagging

Like Bagging, Boosting (AdaBoost.M1) approach was also applied separately to five base learners, namely NB, k-NB, NN, auto MLP and DT. The size (i.e., number of iterations) parameter of boosting was fixed empirically for each base learner because if the value of $1/\beta_t$ in boosting is less than 1 for some iteration value, then the weight of the classifier model may be less than zero for that iteration which is not valid. Table-5.2 reports the obtained size parameter of the base learners for boosting.

Table –5.2: Size variation in Boosting

Base Learners	Size		
	AU	AU+INT	AU+INT+LM
NB	21	18	14
kNB	24	20	17
DT	18	15	14
Auto MLP	16	14	11
NN	15	13	9

If we compare the size requirement of two state-of-the-art ensemble technique, it is clearly observed from Table-5.1 and Table-5.2 that boosting ensemble requires little extra iteration than that of bagging ensemble for each of the classifiers. Like bagging, NN classifiers needs less iterations to give maximum performance among the five classifiers.

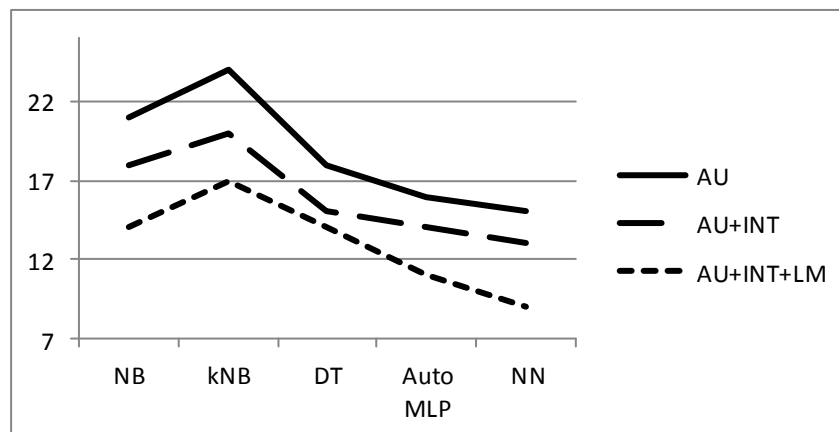


Fig. 5.2: Size variation in Boosting

Training Stacking Models : In stacking, one classifier is used as model learner whereas the others as base learners. In this work, out of five classifiers four classifiers were used as the base learners and the remaining classifier was used as model learner. So, five training models were prepared where each classifier got a chance to be the model learner.

Table –5.3: Model setup in Stacking

Base Learners	Model Learner
kNB, NN, Auto MLP, DT	NB
NB, NN, Auto MLP, DT	kNB
NB, kNB, Auto MLP, DT	NN
NB, kNB, NN, DT	Auto MLP
NB, kNB, NN, Auto MLP	DT

Training Voting Models : Though in stacking five different models were obtained using five classifiers (i.e., NB, k-NB, NN, auto MLP and DT), but in voting the scenario is different. In voting, only one model was obtained. In this case, four classifiers altogether were used as the base learners and majority vote was used as voting approach.

VI. MODEL TESTING AND RESULTS

Evaluation : The actual impacts of the proposals or the predicted results are interpreted by the evaluation. The proposed facial emotion model was evaluated using standard *precision*, *recall* and *F-measure* matrices.

In a classification task, the precision for a class is the number of true positives (i.e. the number of items correctly labeled as belonging to the positive class) divided by the total number of elements labeled as belonging to the positive class (i.e. the sum of true positives and false positives, which are items incorrectly labeled as belonging to the class).

$$Precision (P) = \frac{TP}{TP+FP}$$

where, TP = true positive, FP = false positive

Recall in the classification context is defined as the number of true positives divided by the total number of elements that actually belong to the positive class (i.e. the sum of true positives and false negatives, which are items which were not labeled as belonging to the positive class but should have been).

$$Recall (R) = \frac{TP}{TP+FN}$$

where, TP = true positive, FN = false negative

In a classification task, a precision score of 1.0 for a class C means that every item labeled as belonging to class C does indeed belong to class C but it states nothing about the number of items from class C that were not labeled correctly; whereas, a recall of 1.0 means that every item from class C was labeled as belonging to class C but it states nothing about how many other items were incorrectly also labeled as belonging to class C).

Often, there is an inverse relationship between precision and recall, where it is possible to increase one at the cost of reducing the other. In this context, F-measure is the harmonic mean of precision and recall that combines precision and recall.

$$Precision (P) = 2 \times \frac{Precision \cdot Recall}{Precision + Recall}$$

Testing Models : As discussed in the training section, the training of models is categorized into two sets of experiments, namely person dependent test and person independent test. The following subsections details the outcome obtained for those experiments.

Person dependent Testing : In Person dependent testing, we used the leave-one-out strategy, i.e., one sequence of each testemotion was left out, and the rest were used as the training sequences. Table-5.4 shows the recognition rate for each person for the five classifiers, and the total recognition rate averaged over the five people. Notice that the fifth person has the worst recognition rate. The fact that subject-5 was poorly classified can be attributed to the inaccurate tracking result and lack of sufficient variability in displaying the emotions. It can be noticed that the any of the five classifiers does not significantly decrease the recognition rate (and improves it in some cases), even though the input is unsegmented continuous sequence. Among five classifiers, auto MLP and NN performs almost the same with high recognition rate. The performance of DT is slightly better than that of kNB.

Table –5.4: Results applying individual classifiers

		Subject→					Average
		1	2	3	4	5	
NB	Precision	81.65%	87.46%	85.47%	82.46%	55.59%	78.53%
	Recall	78.94%	83.87%	82.21%	80.53%	53.32%	75.77%
	F-measure	80.27%	85.63%	83.81%	81.48%	54.43%	77.12%
kNB	Precision	82.63%	88.56%	86.31%	83.79%	57.32%	79.72%
	Recall	79.89%	84.76%	83.82%	81.59%	54.41%	76.89%
	F-measure	81.24%	86.62%	85.05%	82.68%	55.83%	78.28%
DT	Precision	83.25%	90.01%	87.43%	85.05%	58.64%	80.88%
	Recall	79.82%	85.11%	83.71%	81.82%	55.28%	77.15%
	F-measure	81.50%	87.49%	85.53%	83.40%	56.91%	78.97%
auto MLP	Precision	84.62%	91.32%	89.03%	85.98%	60.21%	82.23%
	Recall	80.74%	86.27%	84.64%	82.59%	56.89%	78.23%
	F-measure	82.63%	88.72%	86.78%	84.25%	58.50%	80.18%
NN	Precision	84.79%	91.36%	89.22%	86.03%	60.53%	82.39%
	Recall	80.81%	86.21%	84.52%	82.51%	56.97%	78.20%
	F-measure	82.75%	88.71%	86.81%	84.23%	58.70%	80.24%

The results of person dependent testing using classifier combination methods are given in the following tables. It is noticed from the Table-5.5 and Table-5.6 that bagging and boosting performs almost same in facial emotion classification. Again, ensemble with NN classifier outperforms the auto MLP with slight margin and others three (i.e., NB, kNB and DT) with satisfactory margin. It is also noted that ensemble technique improves the classification accuracy than that obtained using individual classifiers.

Table –5.5: Results applying ensemble-Bagging

		Subject→					
		1	2	3	4	5	Average
NB	Precision	82.61%	88.56%	86.42%	83.61%	56.63%	79.57%
	Recall	80.01%	84.79%	83.26%	81.63%	54.29%	76.80%
	F-measure	81.29%	86.63%	84.81%	82.61%	55.44%	78.16%
kNB	Precision	83.53%	89.61%	87.43%	84.72%	58.35%	80.73%
	Recall	80.84%	85.68%	84.78%	82.63%	55.34%	77.85%
	F-measure	82.16%	87.60%	86.08%	83.66%	56.81%	79.26%
DT	Precision	84.21%	90.98%	88.51%	85.99%	59.62%	81.86%
	Recall	80.79%	86.23%	84.79%	82.87%	56.26%	78.19%
	F-measure	82.46%	88.54%	86.61%	84.40%	57.89%	79.98%
auto MLP	Precision	85.57%	92.53%	90.08%	87.01%	61.31%	83.30%
	Recall	81.69%	87.21%	85.56%	83.61%	57.91%	79.20%
	F-measure	83.58%	89.79%	87.76%	85.28%	59.56%	81.20%
NN	Precision	85.82%	92.51%	90.15%	87.05%	61.43%	83.39%
	Recall	81.73%	87.33%	85.49%	83.69%	58.02%	79.25%
	F-measure	83.73%	89.85%	87.76%	85.34%	59.68%	81.27%

Table –5.6: Results applying ensemble-Boosting

		Subject→					
		1	2	3	4	5	Average
NB	Precision	82.73%	88.61%	86.54%	83.58%	56.71%	79.63%
	Recall	79.98%	84.72%	83.32%	81.68%	54.21%	76.78%
	F-measure	81.33%	86.62%	84.90%	82.62%	55.43%	78.18%
kNB	Precision	83.49%	89.68%	87.51%	84.68%	58.41%	80.75%
	Recall	80.97%	85.70%	84.72%	82.67%	55.31%	77.87%
	F-measure	82.21%	87.64%	86.09%	83.66%	56.82%	79.29%
DT	Precision	84.25%	90.91%	88.61%	86.00%	59.72%	81.90%
	Recall	80.83%	86.28%	84.71%	82.84%	56.27%	78.19%
	F-measure	82.50%	88.53%	86.62%	84.39%	57.94%	80.00%
auto MLP	Precision	85.61%	92.49%	90.05%	86.98%	61.38%	83.30%
	Recall	81.70%	87.23%	85.59%	83.67%	57.96%	79.23%
	F-measure	83.61%	89.78%	87.76%	85.29%	59.62%	81.21%
NN	Precision	85.86%	92.48%	90.13%	87.10%	61.48%	83.41%
	Recall	81.75%	87.32%	85.53%	83.65%	58.04%	79.26%
	F-measure	83.75%	89.83%	87.77%	85.34%	59.71%	81.28%

The results obtained using stacking and voting are depicted in Table-5.7 and Table-5.8. In stacking, maximum performance is achieved using NB, kNB, DT and auto MLP as base learner (BL) and NN as model learner (ML). However, from Table-5.7 it is clear that voting technique with majority voting achieved maximum classification accuracy.

Table –5.7: Results applying Stacking

		Subject→						
BL	ML	1	2	3	4	5	Average	
kNB, DT, auto MLP, NN	NB	Precision	83.81%	89.69%	87.61%	84.52%	58.08%	80.74%
		Recall	81.02%	85.69%	84.47%	82.86%	55.29%	77.87%
		F-measure	82.39%	87.64%	86.01%	83.68%	56.65%	79.28%
NB, DT, auto MLP, NN	kNB	Precision	84.66%	90.73%	88.65%	85.81%	59.57%	81.88%
		Recall	81.94%	86.78%	85.84%	83.72%	56.28%	78.91%
		F-measure	83.28%	88.71%	87.22%	84.75%	57.88%	80.37%
NB, kNB, auto MLP, NN	DT	Precision	85.19%	92.08%	89.53%	87.13%	61.02%	82.99%
		Recall	81.89%	87.31%	85.76%	83.97%	57.32%	79.25%
		F-measure	83.51%	89.63%	87.60%	85.52%	59.11%	81.08%
NB, kNB, DT, NN	auto MLP	Precision	86.71%	93.51%	90.98%	88.07%	62.45%	84.34%
		Recall	82.70%	88.26%	86.63%	84.70%	59.05%	80.27%
		F-measure	84.66%	90.81%	88.75%	86.35%	60.70%	82.25%
NB, kNB, DT, auto MLP	NN	Precision	86.78%	93.53%	91.24%	88.05%	62.78%	84.48%
		Recall	82.74%	88.42%	86.49%	84.71%	59.14%	80.30%
		F-measure	84.71%	90.90%	88.80%	86.35%	60.91%	82.33%

Table –5.8: Results applying Voting

		Subject→					Average
		1	2	3	4	5	
NB, kNB, DT, auto MLP, NN	Precision	87.82%	95.08%	92.31%	89.13%	63.86%	85.64%
	Recall	83.81%	89.47%	87.53%	85.74%	61.23%	81.56%
	F-measure	85.77%	92.19%	89.86%	87.40%	62.52%	83.55%

Person independent Testing : In the previous section, it is seen that a good recognition has achieved when the training sequences are taken from the same subject as the test sequences. However, the main challenge is to see if this can be generalized to a person independent recognition. Like person dependent test, first five classifiers were tested independently. The results of the test are shown in Table-5.9. It is observed that if classifiers are applied individually then NN achieved best performance for all cases (80.88%, 83.89% 86.33% with AU, AU + Intensity and AU + Intensity + Landmark respectively).

Table –5.9: Results applying individual classifiers

		Features→								
		AU			AU + INT			AU+ INT+ Landmark		
		P (%)	R (%)	F (%)	P (%)	R (%)	F (%)	P (%)	R (%)	F (%)
Classifier→	NB	75.35	73.53	74.43	78.35	76.33	77.33	80.13	78.47	79.29
	kNB	77.36	75.77	76.56	80.36	78.87	79.61	82.45	81.32	81.88
	DT	78.98	75.82	77.37	81.98	78.52	80.21	84.02	80.38	82.16
	Auto MLP	81.03	78.93	79.97	84.03	81.73	82.86	86.23	84.76	85.49
	NN	82.11	79.69	80.88	85.11	82.71	83.89	87.49	85.21	86.33

The results obtained using classifier ensemble methods are given in Table-5.10 and Table-5.11. It is noticed from the Table-5.10 and Table-5.11 that bagging and boosting performs almost same (the difference between classification accuracy is almost 0.02% for all cases) in facial emotion classification for person independent testing. Again, ensemble with NN classifier outperforms the auto MLP with slight margin (0.01% and 0.03% for bagging and boosting respectively) and others three (i.e., NB, kNB and DT) with satisfactory margin. It is also noted that ensemble technique improves the classification accuracy than that obtained using individual classifiers.

Table –5.10: Results applying Ensemble-Bagging

		Features→								
		AU			AU + INT			AU+ INT+ Landmark		
		P (%)	R (%)	F (%)	P (%)	R (%)	F (%)	P (%)	R (%)	F (%)
Classifier→	NB	77.21	74.97	76.07	80.23	78.33	79.27	81.98	80.31	81.14
	kNB	79.04	77.48	78.25	82.04	80.57	81.30	84.24	83.47	83.85
	DT	80.87	77.79	79.30	83.59	80.65	82.09	85.89	82.29	84.05
	Auto MLP	82.97	80.76	81.85	85.89	83.71	84.79	88.03	86.79	87.41
	NN	83.95	81.82	82.87	87.01	84.59	85.78	89.51	87.36	88.42

Table –5.11: Results applying Ensemble-Boosting

		Features→								
		AU			AU + INT			AU+ INT+ Landmark		
		P (%)	R (%)	F (%)	P (%)	R (%)	F (%)	P (%)	R (%)	F (%)
Classifier→	NB	77.19	75.02	76.09	80.29	78.27	79.27	82.01	80.32	81.16
	kNB	78.98	77.58	78.27	81.97	80.65	81.30	84.17	83.61	83.89
	DT	80.95	77.68	79.28	83.68	80.59	82.11	85.97	82.21	84.05
	Auto MLP	83.02	80.84	81.92	85.93	83.74	84.82	88.06	86.77	87.41
	NN	83.87	81.93	82.89	86.93	84.67	85.79	89.45	87.46	88.44

Table-5.12 and Table-5.13 show the results obtained using stacking and voting techniques. In person dependent testing, stacking technique achieved maximum performance when NB, kNB, DT and auto MLP were used as BL and NN was used as ML. However, in person independent testing the stacking technique performed best when NB, kNB, DT and NN were used as BL and auto MLP was used as ML. ML with auto MLP outperforms the ML with NB, kNB, DT and NN with 8.21%, 5.47%, 5.33% and 0.37% respectively. Table-X confirms that voting technique with majority voting achieved maximum classification accuracy (90.04%).

Table –5.12: Results applying Stacking

		Features→								
		AU			AU + INT			AU+ INT+ Landmark		
BL	ML	P (%)	R (%)	F (%)	P (%)	R (%)	F (%)	P (%)	R (%)	F (%)
kNB, DT, auto MLP, NN	NB	78.25	76.09	77.15	81.29	78.27	79.75	83.01	80.32	81.64
NB,DT, auto MLP, NN	kNB	80.01	78.41	79.20	82.89	81.58	82.23	85.17	83.61	84.38
NB, kNB, auto MLP, NN	DT	82.05	78.51	80.24	84.51	81.43	82.94	86.97	82.21	84.52
NB, kNB, DT, NN	Auto MLP	85.02	82.69	83.84	88.11	85.61	86.84	90.68	89.03	89.85
NB, kNB, DT, auto MLP	NN	84.59	82.84	83.71	88.03	85.59	86.79	90.61	88.37	89.48

Table –5.13: Results applying Voting

		Features→								
		AU			AU + INT			AU+ INT+ Landmark		
BL	ML	P (%)	R (%)	F (%)	P (%)	R (%)	F (%)	P (%)	R (%)	F (%)
NB, kNB, DT, auto MLP, NN		85.23	82.74	83.97	88.23	85.65	86.92	91.03	89.07	90.04

Conclusion and future work

In this work, the proposed methodology for recognizing emotions through facial expressions displayed in video sequences using the state-of-the-art classifier combination approaches, namely ensemble, stacking and voting.

The main contributions of this work are-

- introduction of classifier combination methodologies in the emotion recognition on facial expressions task.
- enhancement of classification accuracy of emotion recognition on facial expressions task.
- Classification accuracy is increased for both the person dependent and independent emotion identification.

Overall voting technique with majority voting achieved best classification accuracy.

The emotion recognition from just the facial expressions is probably not accurate enough. Therefore, other measurements probably have to be employed to interact the emotional state of a human with a computer properly. This work is just another step on the way toward achieving the goal of building more effective computers that can serve us better. For future research, we shall focus on facial expressions and body gestures in individual framework as well as multimodal framework because body movements and gestures have recently started attracting the attention of the HCI community. We will have an approach of skin color segmentation on HSV (Hue, saturation and value) space for facial and body feature extraction to recognise emotion.

One of the future directions of this work may be incorporated the color model (e.g., HSV) into emotion recognition on facial expressions task. The image may be represented to a color model. The color values may be used to compute AU, intensity etc. This may be applied to process facial expression of images in digital printing.

Moreover, the integration of multiple modalities such as voice analysis and context would be expected to improve the recognition rates and eventually improve the computer's understanding of human emotional states. This research will be continued to find better methods to fuse audio-visual information that model the dynamics of facial expressions and speech.

REFERENCES

- [1] C. Darwin, *The Expression of the Emotions in Man and Animals*, J. Murray, London, 1872.
- [2] P. Ekman and W. Friesen. *The Facial Action Coding System: A Technique For The Measurement of Facial Movement*. Consulting Psychologists Press, Inc., San Francisco, CA, 1978.
- [3] J. Russell and J. Fernandez-Dols, *The Psychology of Facial Expression*. New York: Cambridge Univ. Press, 1997.
- [4] P. Ekman, W.V. Friesen, Constants across cultures in the face and emotion, *J. Personality Social Psychol.* 17 (2) (1971) 124–129.
- [5] M. Suwa, N. Sugie, K. Fujimora, A preliminary note on pattern recognition of human emotional expression, *Proceedings of the Fourth International Joint Conference on Pattern Recognition*, Kyoto, Japan, 1978, pp. 408–410
- [6] De Silva, L. C., Miyasato, T., and Nakatsu, R. Facial Emotion Recognition Using Multimodal Information. In *Proc. IEEE Int. Conf. on Information, Communications and Signal Processing (ICICS'97)*, Singapore, pp. 397–401, Sept. 1997.
- [7] Chen, L.S., Huang, T. S., Miyasato T., and Nakatsu R. Multimodal human emotion / expression recognition, in *Proc. of Int. Conf. on Automatic Face and Gesture Recognition*, (Nara, Japan), IEEE Computer Soc., April 1998
- [8] Pantic, M., Rothkrantz, L.J.M. Toward an affect-sensitive multimodal human-computer interaction. *Proceedings of the IEEE*, Volume: 91 Issue: 9 Sept. 2003. Page(s): 1370 –1390.
- [9] Mase K. Recognition of facial expression from optical flow. *IEICE Transc.*, E. 74(10):3474–3483, October 1991.
- [10] Yacoob, Y., Davis, L. Computing spatio-temporal representations of human faces. *Computer Vision and Pattern Recognition*, 1994. *Proceedings CVPR '94.*, 1994 IEEE Computer Society Conference on , 21-23 June 1994 Page(s): 70–75.
- [11] N. Sebe, I. Cohen, A. Garg, M. Lew, and T. Huang. Emotion recognition using a Cauchy Naive Bayes classifier. In *ICPR*, 2002, to appear.
- [12] H. Tao and T. S. Huang. Connected vibrations: A modal analysis approach to non-rigid motion tracking. In *CVPR*, pages 735–750, 1998.
- [13] Ekman, P., Friesen, W. V., & Tomkins, S. S. Facial affect scoring technique (FAST): A first validity study. *Semiotica*~ 1971,3 (1), 37–58.
- [14] N. Sebe, I. Cohen, A. Garg, M. Lew, and T. Huang. Emotion recognition using a Cauchy Naive Bayes classifier.
- [15] Black, M. J. and Yacoob, Y. Tracking and recognizing rigid and non-rigid facial motions using local parametric model of image motion. In *Proceedings of the International Conference on Computer Vision*, pages 374–381. IEEE Computer Society, Cambridge, MA, 1995.
- [16] Tian, Ying-li, Kanade, T. and Cohn, J. Recognizing Lower Face Action Units for Facial Expression Analysis. *Proceedings of the 4th IEEE International Conference on Automatic Face and Gesture Recognition (FG'00)*, March, 2000, pp. 484 – 490.
- [17] I. A. Essa and A. P. Pentland, “Coding, analysis, interpretation, and recognition of facial expressions,” *IEEE Transactions on Pattern Analysis and Machine Intelligence*, vol. 19, pp. 757–763, July 1997.
- [18] G. Faigin, *The Artist's Complete Guide To Facial Expression*. New York, NY: Watson-Guption Publications, 1990.
- [19] M. Rosenblum, Y. Yacoob, and L. Davis, “Human expression recognition from motion using a radial basis function network architecture,” *IEEE Transactions on Neural Network*, vol. 7, pp. 1121–1138, September 1996.
- [20] R. Aris. *Discrete Dynamic Programming*. Blaisdel, 1964. A. Lanitis, C. J. Taylor, and T. F. Cootes, “A unified approach to coding and interpreting face images,” in *Proc. 5th International Conference on Computer Vision (ICCV)*, Cambridge, USA, 1995, pp. 368–373.
- [21] Hager, J., Ekman~ P., & Friesen, W. V. A comparison of facial measurement procedures. In P. Ekman & W. V. Friesen (Eds.), *An atlas of Facial action*. Book in preparation.
- [22] K. Matsuno, C. Lee, and S. Tsuji, “Recognition of human facial expressions without feature extraction”, *Proceedings of the European Conference on Computer Vision*, 513–520, 1994.
- [23] Y.-L. Tian, T. Kanade, and J. Cohn. Facial expression analysis. In S. L. . A. Jain, editor, *Handbook of face recognition*, pages 247–276. Springer, New York, New York, 2005.
- [24] T. Kanade, J. Cohn, and Y. Tian. Comprehensive database for facial expression analysis. In *Proceedings of the International Conference on Automatic Face and Gesture Recognition*, pages 46–53, 2000. 1,2[15] S.
- [25] Lucey et al. The Extended Cohn-Kanade Dataset (CK+): A complete dataset for action unit and emotion-specified expression

A Survey on Rendezvous Based Techniques for Power Conservation in Wireless Sensor Networks

Ruthvic S D¹, Ravi B², Dr. Uday Kumar Shenoy³

¹ PG Scholar, Dept. of Computer Science and Engineering, NMAM Institute of Technology, Nitte, India.

² Asst. Professor, Dept. of Computer Science and Engineering, NMAM Institute of Technology, Nitte, India.

³ Professor, Dept. of Information Science and Engineering, NMAM Institute of Technology, Nitte, India.

ABSTRACT:

Power conservation is a vibrant research area in wireless sensor networks. Several research works have demonstrated that energy can be conserved significantly using mobile sink in the sensor field, which will collect the data from the sensor nodes via single or multi hop communication. But, the mobility speed of the sink is low, due to which latency will be increased in sensor network especially in delay sensitive applications. To address this issue, various rendezvous based techniques have been described according to which a subset of sensor nodes from the field will be selected as rendezvous points (RPs). Remaining nodes will forward the sensed data to its nearest RP where data will be buffered. A path is then constructed using the RPs through which mobile sink will make a tour and collects the buffered data. This paper explains different rendezvous based techniques and analysis of their advantages and deficiencies with respect to power conservation.

KEYWORDS: Data sensing, Mobile Sink, Power conservation, Rendezvous points, Sensor nodes, Steiner Minimum Tree (SMT), Wireless sensor networks.

I. INTRODUCTION

Wireless sensor network is an environment built of several sensors to monitor the environmental conditions. These sensor nodes will sense the data from the surrounding environment and forwards it to the central location known as base station (sink) through wireless communication. Today many industrial and consumer applications such as waste water detection, smart home etc. are using sensor networks. The major drawback of the WSN is the battery life of sensor nodes which may not be replaced or recharged. This leads to vital research area in the field of sensor networks. Usually the sensed data will be transferred to the base station for processing using ad-hoc multi-hop network formed by the sensor nodes. Though this technique is feasible, it creates a bottleneck in the network.

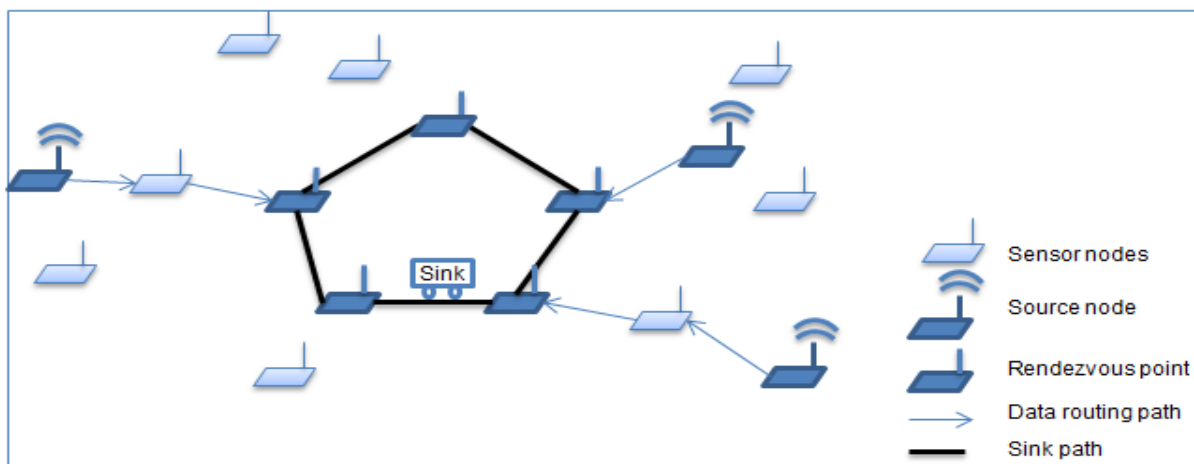


Figure 1: An example of rendezvous based technique. Source node will forward the sensed data to its nearest RP. Mobile sink will make a tour and collects the data buffered at the RP.

The nodes near to the sink are overburdened due to the data from the farther nodes and the battery of those nodes will drain very quickly which leads to non-uniform energy level of the nodes which ultimately results in network partition [1]. Various research works have shown that the mobile sink will resolve the problem by collecting the data directly from the sensor nodes via single or limited multi hop communication. This can be formulated as Travelling Sales Man problem (TSP) which is well known problem in graph theory. The aim of TSP is to find the shortest path using which the sink must visit all the sensor nodes exactly once and return back to its original position. However, as the number of nodes increases, this problem becomes impractical [2]. Moreover typical speed of mobile sink is low such that it takes long time to complete a tour in large network area. Due to this drawback of sink mobility, latency will get increase in delay sensitive applications [3], such as fire- detection system. Hence, researchers have proposed rendezvous based technique in which the subset of sensor nodes are selected as RP and non-RPs will just forwards the sensed data to its nearest RP where data will get buffered. For these selected RP, a tour is computed through which mobile sink will travel and gather the buffered data as shown in figure1. In This paper we discuss the different rendezvous based techniques to bind the tour length. Each of the techniques RP-CP, RP-UG, RD-VT, CB and WRP proposed in [2] [3] [4] [5] follow different ways to solve the problem. They have their own benefits and shortcomings in terms of energy consumption in sensor networks.

II. RELATED WORK

Many existing methods which uses mobile sink in sensor network have proved that the energy can be efficiently utilized and overall network lifetime can be improved. According to the taxonomy provided in [6], WSN with mobile sink can be divided into two classes: 1) *Direct* and 2) *rendezvous*. In the former method mobile sink will collect the data via single hop and focus on minimizing the data collection delays. Whereas in the latter method, mobile sink only visits the RPs with the aim of minimizing the energy consumption. The pitfalls in *direct* method can be seen when sensor nodes exists in greater number which in turn increases the mobile sink tour length. This results in buffer overflow at the sensors due to data collection delays. To deal with this problem, rendezvous based technique has been proposed. Taxonomy given in [6] further divides the rendezvous method into 3 classes: 1) *Fixed* 2) *Tree based* and 3) *Clustering*. In *fixed* [7], sensor nodes are randomly deployed and the sink path is predefined. The nodes that exist within the communication range of mobile sink will acts as RP. In this method, the length of the sink path is independent on the sensor nodes buffer size or application deadline. Hence, the buffer of RPs may overflow or packets may expire before they are collected.

Xing et al. in [5] proposed a *tree based* algorithm known as RD-VT (rendezvous design with a variable BS track) to find the RP on SMT (Steiner minimum tree) where data will be efficiently buffered and in turn decreasing the sink tour length. A Steiner tree spans a given subset of vertices of a graph. Steiner minimal tree has three major properties. 1) No two edges will meet at an angle less than 120° . 2) Each Steiner point has degree of 3. 3) No crossing edges. It uses the equilateral triangle, a circle and a line principle to construct a Steiner point for a set containing three points on the minimum spanning tree [2]. There are two types of Steiner points, *terminals* and *non-terminals*. First type represents real sensor nodes and the second one represents a physical position without sensor nodes known as virtual Steiner points. The RD-VT starts with constructing a SMT by considering the sink as root. Then SMT is traversed in pre-order from, until the shortest distance between the visited nodes is equal to the required packet delivery time.

Xing et al. in [3] proposed two rendezvous planning algorithms known as RP-CP (Optimal Rendezvous Planning with Constrained ME Path) and RP-UG (rendezvous planning with utility based greedy heuristic). RP-CP deals with constrained mobile sink path. A tree is constructed which connects all the sensor nodes present in the field with sink node as the root. A weight is assigned to each of the edges present in the tree. The weight corresponds to the number of nodes uses that edge to transfer the data to the sink. To construct a path, RP-CP first sorts all the edges with respect to their weight. Then the highest weighted edge is selected until the length of the selected edges becomes less than or equal to the required packet delivery time.

RP-UG [3] is a greedy algorithm which is an improvised version of RP-CP and deals with non-constrained mobile sink path. As in RP-CP, RP-UG also constructs the rooted tree which is rooted to the sink node and all the edges constructed on the tree are divided into several short intervals L_0 . All the nodes that join two edges with length L_0 are selected as RP. Starting with the sink node, RP-UG operates in multiple iterations. In each of the iteration, the tour of the sink node is increased by adding new RP with greatest utility until the maximum tour length is reached. The utility of RP is defined as the ratio of the network energy saved by including it on the sink tour to the length increase of the tour. As the sink tour is expanded, the utility of the nodes will be dynamically updated which results in better selection of RP.

The hop count of each node to its nearest RP will be related to the power consumption of it imposes on peers. To decrease the number of hops from all the sensors to their nearest respective RP, Khaled Almi'ani et al. in [4] proposed *Cluster Based* algorithm which iteratively obtains the mobile sink tour and the routing trees. According to this algorithm, network is grouped into number of balanced size clusters. By selecting only one RP from each cluster, a sink path is constructed such that the sink visits maximum number of clusters and the tour length constraint is satisfied. In *rendezvous* based technique, the basic problem is to find the RP and computing an optimal sink tour path such that sink visits all the RPs and returns to its initial position. However, this is an NP-hard problem. Hence, Salarian et al. [2] proposed WRP (Weighted Rendezvous Planning algorithm). WRP is a heuristic approach based on hybrid unconstrained mobility pattern for sink. The problem is defined as follows:

- Let $G(V, E)$ be the graph that consists of n number of homogeneous sensor nodes, V and set of edges E between the nodes.
- Let $n_0, n_1, n_2, \dots, n_n$ be the set of sensor nodes where $n_i \in V$ and are randomly located in a field from where data need to be sensed.
- Let $M = m_0, m_1, m_2, \dots, m_n, m_0$, be the set of sensor nodes where $m_i \in V$ such that it comprises of high weight and considered as rendezvous points.

The objective is to find a tour using set of nodes present in M such that sink only visits the RP and the tour M is no longer than maximum allowed tour length (l_{max}) where,

$$l_{max} = D \times v \quad (1)$$

D is maximum allowed packet delay and v is the mobile sink speed. The sensor nodes other than RP, directly forwards the sensed data to their nearest RP. The RP will collect and buffer all the data sent by the sensors and forward it to the sink when it comes to RP's vicinity. WRP will assign a weight to each sensor nodes and computes a tour by selecting the highest weighted sensor nodes as rendezvous point. As per the paper [2], equation to calculate the weight of each sensor node is,

$$W_i = NFD(i) \times H(i, M) \quad (2)$$

Where, W_i is the weight of node i , $NFD(i)$ is the number of packets that the node i will forwards and $H(i, M)$ is the hop distance of node i from the closest RP in M . According to the equation, the nodes that are located farther away from the selected RP or the nodes that have more than one packet to be forwarded will have higher priority and it will be selected as RP. If the sensor node that is located only in one hop distance from the selected RP and have only one data packet buffered will get the minimum weight. Hence, by visiting the highest weighted sensor node, the number of multi-hop transmissions will be decreased and load will be balanced among the sensor nodes which ultimately results in power conservation.

III. ANALYSIS OF RD-VT, RP-CP, RP-UG, CB AND WRP

This section provides the analysis of different rendezvous based techniques in terms of their benefits and drawbacks towards power conservation.

RD-VT: SMT based approach Steiner point in RD-VT may not be position of sensor node, and algorithm will replaces the virtual RPs with the sensor node that is closer to them. This approach will provide the desired performance under certain range of settings. In addition, this algorithm will maintain the communication delay and also enables the sink to collect bulk of data at a time from the RP. However, SMT is traversed in pre-order to find RPs, it will results in long data transferring paths to the sensors which are located in different locations of SMT. Hence, RD-VT fails to balance the load among sensors and power consumption [5].

RP-CP: RP-CP operates on the SMT by considering the edges of the routed tree and its assigned weights. This technique significantly reduces the power consumption of the sensor network. But, the Sensor nodes on the selected edges will be visited twice by the mobile sink because of constrained sink mobility path on the edges of routing tree [3].

RP-UG: RP-UG is an improvised method of RP-CP and utility based greedy algorithm which will operates on the routed tree. As the sink tour is expanded, the utility of the nodes will be dynamically updated which results in better selection of RP. But, RP-UG appoints the sensor node as RP which are closer to the sink which many not have highest energy consumption rate [2]. Hence, the energy consumption rate of the sensor nodes cannot be balanced by the RP-UG which ultimately effects the lifetime of the network. Along with this deficiency, this

algorithm uses TSP solver N times in each iteration (N is the number of RPs) and hence, running complexity of this algorithm is $O(N^2 * O(TSP))$ [3].

CB: Cluster based algorithm uses binary search method to select the rendezvous points. Initially cluster is formed and algorithm traverses through all the clusters to select one node as RP from each cluster and sink path is constructed that satisfies the tour length constraint. CB will contribute more in terms of power conservation than RD-VT. In some scenario, the sink path does not pass through the dense parts of the network and results in long data transfer path from the sensors to the RP. Hence, the battery of sensor nodes will drain in non-uniform manner which ultimately decreases the WSN lifetime [4].

WRP: Weighted Rendezvous Planning heuristic algorithm also uses SMT and selects the set of RPs. When comparing with the RP-UG and RD-VT with WRP, the former two algorithms will replace the virtual RPs with the nearest sensor nodes whereas in the latter algorithm, virtual RP present in the Steiner tree will not be replaced by any nodes. Instead the virtual Steiner positions present in the tour will be visited by the sink and it will collect the data from the nearest sensor node which leads to fewer numbers of RPs and uniform energy consumption. Hence, WRP performs better than RD-VT and RP-UG. As mentioned in the previous paragraph, unlike CB, WRP will concentrate on hop count while selecting the RP. Hence, WRP minimizes the energy consumption when compared to CB. In addition to this, WRP reduces the occurrence of energy hole problem [6] in sensor networks because the mobile sink visits the congestion points that likely exists in the dense areas [2]. The performance of the sensor network can be further enhanced by using multiple mobile sinks in the field. A sensor network is divided into two or more groups such that each group consists of sensor nodes with similar features. Every group is assigned with a mobile sink and WRP is executed in each group to collect the data.

IV. CONCLUSIONS

Power conservation is a challenging task in WSN which depends on various parameters. In this paper, different rendezvous based algorithms and their analysis has been discussed. All of them focus on finding RPs and efficient tour for mobile sink path so that the sink only visits the RPs and collect the sensed readings within delay bound. Though there are merits and de-merits in each of the techniques, WRP performs better in terms of energy consumption. It will prevent the formation of energy holes in the sensor network and finally results in overall network power conservation.

REFERENCES

- [1] Arun A Somasundara, Aditya Ramamoorthy and Mani B Srivastava, "Mobile Element Scheduling for Efficient Data Collection in Wireless Sensor Networks with Dynamic Deadlines", Proceedings of the 25th IEEE International Real-Time Systems Symposium (RTSS), IEEE, 2004.
- [2] Hamidreza Salarian, Kwan-Wu Chin and Fazel Naghdy, "An Energy Efficient Mobile Sink Path Selection Strategy for Wireless Sensor Networks", IEEE Transactions on Vehicular Technology, Vol. 63, No. 5, June 2014.
- [3] Guoliang Xing, Tian Wang, Zhihui Xie and Weijia Jia, "Rendezvous Planning in Wireless Sensor Networks with Mobile Elements", IEEE Transaction on Mobile Computing, Vol. 7, No. 12, December 2008.
- [4] Khaled Almi'ani, Anastasios Viglas and Lavy Libman, "Energy-Efficient Data gathering with Tour Length-Constrained Mobile Elements in Wireless Sensor Networks", pp. 582-589, Proceedings of the 35th IEEE Conference, LCN, Denver, CO, USA, October 2004.
- [5] Guoliang Xing, Tian Wang, Weijia Jia and Minming Li, "Rendezvous Design Algorithms for Wireless Sensor Networks with a Mobile Base Station", ACM Press, Hong Kong, China, 2008.
- [6] X Li, A Nayak and Stojmenovic, "Sink Mobility in Wireless Sensor Networks", pp. 153-184, Wiley, Hoboken, NJ, USA, 2010.
- [7] Shuai Gao, Hongke Zhang and Sajal K Das, "Efficient Data Collection in Wireless Sensor Networks with Path-Constrained Mobile Sinks", IEEE Transaction on Mobile Computing, Vol. 10, No. 5, April 2011.

Factors Affecting the Discharge Capacity of Shahi Katta Drain, Peshawar City Pakistan

¹,Navid Ahmad , ²,Syed Salman A Shah , ³Gulfam Shahzad

¹ Assistant Professor, Civil Engg; Dept; Uet Peshawar, Pakistan

² Nuiip, Uet Peshawar, Khyber Pakhtunkhwa, Pakistan

³ Nuiip, Uet Peshawar, Khyber Pakhtunkhwa, Pakistan

ABSTRACT:

The research aim to study the hydrologic and hydraulic conditions of Shahi Katta, a case study for major drains in the Peshawar City. It is a major drain with a length of 4.1 Mile or 6.56 Km approximately. The growth pattern observed along the drain is complex and so the exact study of Shahi Katta becomes much more complicated. This study was performed for a section of Shahi Katta with using uniform flow technique for calculation of Peak Discharges in different months of the year for 30 years of data. A section for the study was selected which was flooded in the 2010 major storm event. It was found from analysis that even after hundreds of years, Shahi Katta still has the capacity to carry the present discharge including both sanitary and storm water, however, the presence utility lines, encroachment and solid dumps inside the drains offer resistance to the flow. The maximum capacity shown by the drain section was 57 cumecs. Shahi Katta has still the capacity to accommodate the present discharge, if maintained properly.

KEYWORDS: Hydrologic and Hydraulic, Shahi Katta, Peak Discharge, 30 years data, 2010 Storm event, Sanitary, Storm, Maximum capacity

I. INTRODUCTION

Major Cities in most of the third world countries face the problem of drainage and sewerage, due to rapid increase in the population and lack of planning of population distribution and infrastructure. The construction activities in such cities block the path of flow of drainage and sewage in some parts while divert in other parts. The illegal construction vanishes small drains and so the discharge of these small drains is diverted to the main channel or drain. Such abnormal activities of the drains cause overflow and prevents from any future intervention in the drainage system. Peshawar is an old and historic city of great geographical and administrative importance. Shahi Katta is one of the most important and major drain that conveys waste water including both storm and sanitary sewage across the most commercial and crowded part of the city. It originated from Saddar near Deans Trade Center and passed through Shuba Bazar, Qissa Khwani Bazar, Shabistan Cinema Chowk, Arbab Niaz Stadium and finally through Faqir Abad drops in Budni Nulla (Fig 01).It also passes under the irrigation Channel near Faqir Abad without any syphoned structure. Most of the drain is paved and channelized. About 52% of the drain is hidden under structures including shops, malls, hotels, worship places, culverts and slabs. The population censuses of 1998 is projected for the estimation of city's population on 3% annual growth rate ^[1]. The rain fall in most of the cases and specifically in the storm event 2010 showed abnormal behavior by overflowing in most of its parts. The survey of whole Shahi Katta was not possible due to the facts mentioned above, so a section was selected owing to the ease and possibility of physical survey and flooding of the reach in past few years. The section does not reflect the whole of Shahi Katta, however, it gives an idea of the overall behavior of the drain.

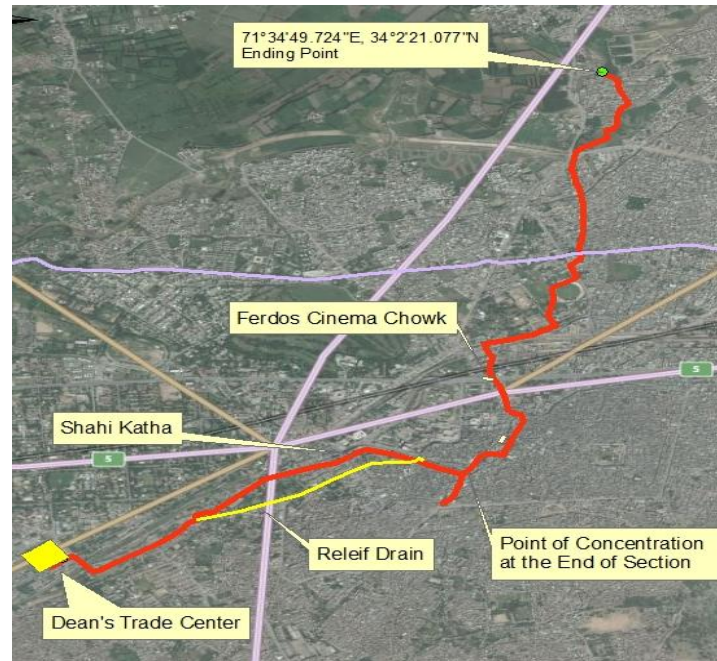


Fig 01: Location of Shahi Katta Drain

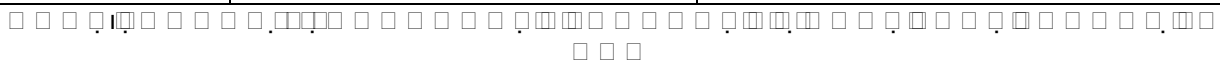
II. METHOD AND PROCEDURE

The topographic survey of the catchment area was carried out with GIS, using the SRTM Imagery and Arc Map Extension, to analyze the contours of the area and the surface type of the land parcel contributing to the flow^{[2][3][4][5][6][7]}. The reconnaissance survey was carried out for verification of ground information to be used as an input to the model which resulted in composite values of runoff coefficient and SCS runoff curve numbers. Different models were studied, selected and applied keeping in view the availability of source and input parameters. Two models including rational procedure was applied using the IDF curve developed for Peshawar^{[4][8]} and SCS Run-off curve number procedure^[9]. The rainfall data on daily basis was for 30 years storm period. The data on monthly basis was observed and SCS model was applied both for the peak value of discharge and the average flow. To apply the flow on Shahi Katta, a section was selected which was visible and survey could be carried out since the survey of whole of Shahi Katta was not possible because of the encroachment issues. The discharge values were applied using HEC-RAS 4.1 to find out hydraulic parameters of flow in the channel^{[10][11]}.

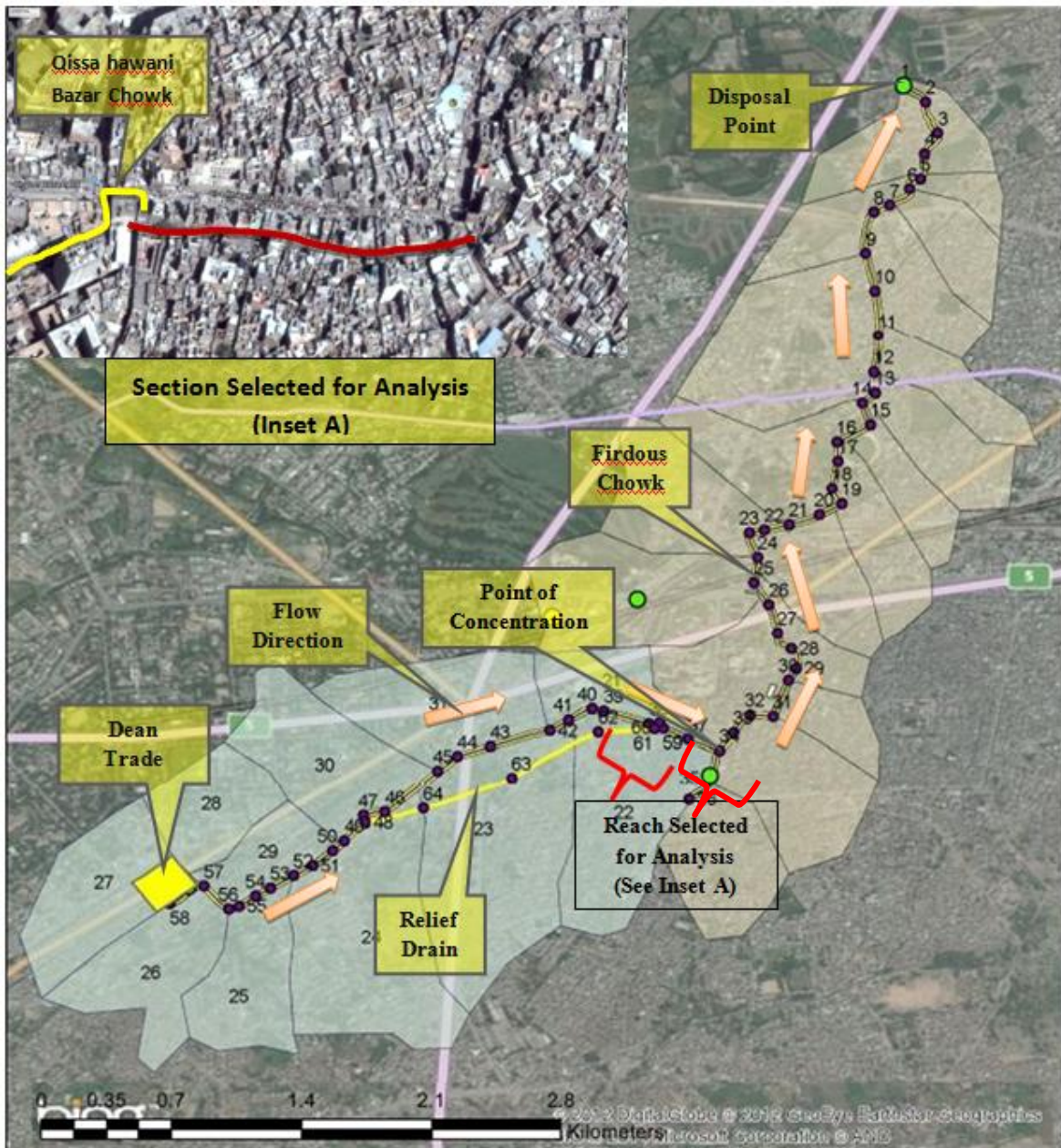
III. RESULTS AND DISCUSSION

The present demography and land parcels in Peshawar are changing rapidly due to unstable political, law and order situation. The lack of enforcement on existing and new urban infrastructure laws and regulations has made the future projection of the demography and infrastructure development cumbersome. This future projection of the city from present condition requires a complete study which was out of the scope of the research. The drainage area of Shahi Katta contributing was calculated. The discharge from the catchment area of Shahi Katta based on Rational and SCS Curve Number methods are given in Table 01 whereas Table 02 summarize the result of the analysis for Reach Section (RS1 and RS2) selected for analysis of the drain. The rational method resulted with a value of 2545.48 cusecs for the overall drainage area of Shahi Katta^[12] and a value of 1297 cusecs for the section. The SCS Runoff curve number procedures showed the values in table 01. The values of flow are shown in table 02 for the selected reach (section).

Rational Method	Discharge 2546.48 Cusecs	
SCS Curve Number Method	Discharge (Cusecs) based on Maximum rainfall values.	
	Minimum	Maximum
	446.4	1173.5



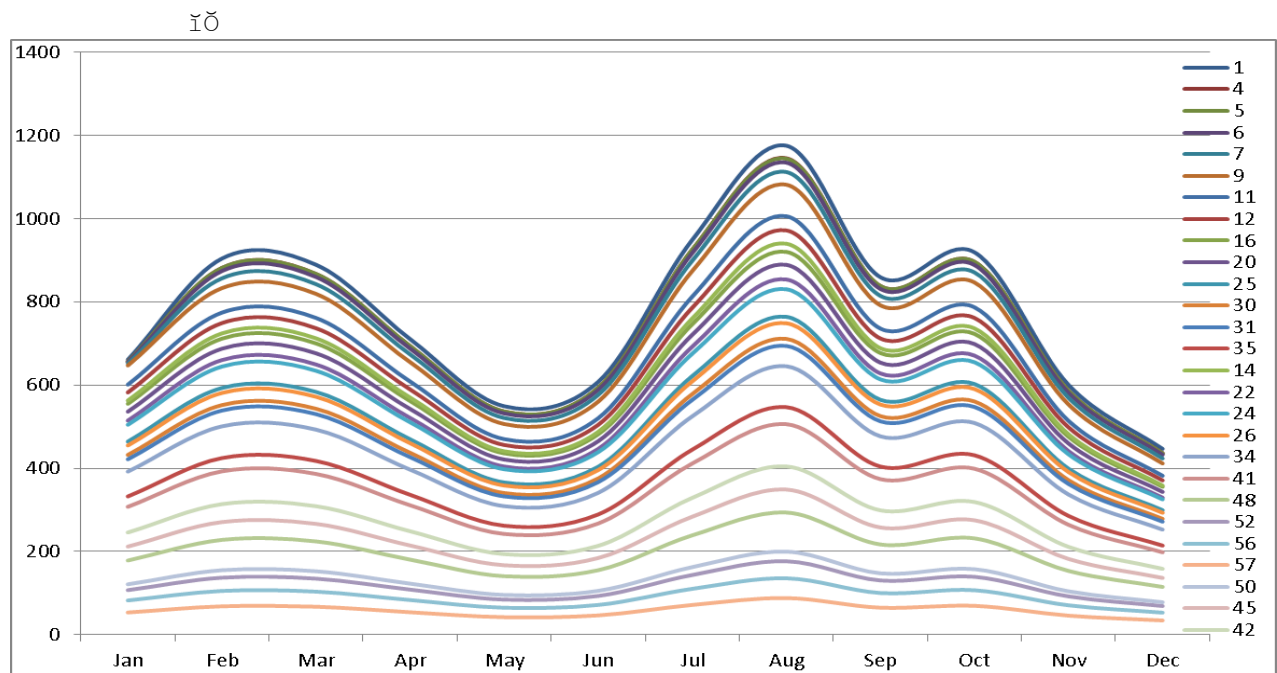
S #	Reach Section	Procedure	Discharges in Cusecs	Flow Velocity(ft/sec)	Flow Depth(ft)
01	Reach Section RS1	Rational	1297	13.41	5.54
		Maximum Rainfall Discharge (August)	645.55	10.63	3.48
02	Reach Section RS2	Rational	1297	13.41	5.54
		Maximum Rainfall Discharge (August)	645.55	10.63	3.48



* All the data are in SI Systems (metre) and the map is drawn in ArcMap 10

The behavior of rainfall directly impacts the discharge in the channels flow. The drainage area contributing to the Shahi Katta in Peshawar City shows its peak discharge in the month of August. This indicates that most of the chances of heavy discharges (Flooding) in Peshawar City occur in the month of August causing a peak flow of 1175 cusecs with a drop in the coming months as evident from the past 30 years

data from ranging from 1978 to 2007. The flow in the month of May drop to a value of 549 cusecs which then again rises to a value of 1175 cusecs in the month of August. The lowest discharge is observed in the month of December as 447 cusecs as shown in Fig 03. The flow variation show less intensity and remain inside the drain without overflowing.



The results make it evident that even after passing hundreds of years of Shahi Katta drain, it is still in the position to take the discharges that flow inside the drain in most of its sections. The variation of flow in the drain was changed with the Metrologic conditions of the area. The storm sewage in the section was quite less than the capacity at present. It was revealed from the flow values and the calculations that Shahi Katta can be better expressed by Rational method. The value of discharge from the rational method was about 1297 cusecs. The depth of flow during storm event, as derived from the personal interviews was about 6 ft, while that from the calculation was 5.4 ft. The discharge capacity in most of the sections was low. The obvious reason was no proper solid waste management system for Peshawar City. Most of the part of Shahi Katta drain is chocked by the waste generated by nearby area. In some places the small sections are followed by large sections which caused ponding effects thus causing sedimentation in the flow and the solid part to accumulate. The flow in most of the parts of drain is obstructed by the utility lines passing through the drain and the encroachment in the drain.

IV. CONCLUSION AND RECOMMENDATIONS:

No authentic drawings were found during the research. The authority may carry out the complete survey as it requires a lot of resources and is a difficult job. It will not only define the right of way for Shahi Katta but will also help in cleaning and maintenance plan.

Three different encroachments are present in and along Shahi Katta that are as follows:

- [1] The structures that are used to support the slabs of shops built over the drain (Fig 04) i.e. columns etc.
- [2] Construction of brick walls inside the drain thus reducing the sections size (Fig 05).
- [3] Shops and other market with their floors as slab over the drain thus converting the drain into a box culvert shape (Fig 06).

The concerned departments are advised to remove these encroachments to make able Shahi Katta to regain its capacity.

- a. It is recommended that the Curve Number for Peshawar should be made on current maps since the one developed for Peshawar was quite older and since lot of changes have occurred in the past two decades, so a fresh study should be carried out.
- b. The population censuses in Peshawar was carried out in 1998. All of the government departments use a standard of 3 percent increase in population for the projection of population for any project. This procedure

is used in areas where no major changes had occurred regarding demography and relocation of population. The native areas of Peshawar are undergoing stresses which lead to a major displacement inside the city, there is an enormous intake of population from country side. As such the projection of 1998 population censuses to 2014 and onward for the 20 years becomes unreliable and so there is a dire need to carry out censuses for present conditions study and future population project.

- c. Absence of complete manual for design, implementation and relocation of utilities has not been defined so far. It is recommended that such manuals be established and published specifying the codes for installation of the utilities. The utilities offering obstruction to the flow of Shahi Katta need to be relocated on emergency basis as soon as possible.
- d. A regular practice for cleaning of the drain needs to be carried out to keep the drain flowing smoothly.
- e. Building of a proper solid waste management system is a need of Peshawar City. It is not possible to keep Shahi Katta clean until and unless the solid waste management system is defined. Since there is no proper system of disposal of wastes, the inhabitants throw their wastes inside the drain as shown in Figure 07. Such practices makes problem in flow of drain, generates diseases and are drained off as water bodies causing a threat to the aquatic life. Proper education and rules enforcement will help to prevent the inhabitants from throwing wastes

REFERENCES:

- [1]. Population Density and Demographics from official website www.nwfp.gov.pk accessed on 23rd April 2013
- [2]. Drachal J., "Striking variety of the mountain chains appearance on satellite images provided by google earth", 2006.
- [3]. H.M. Ragunath, "Hydrology, Principal Analysis and Design", Revised 2nd Edition, 2006.
- [4]. Zubair K., "Intensity Frequency Duration curves for NWFP", 2007.
- [5]. Kirpich, Z.P., "Time of concentration of small agricultural watersheds: Civil Engineering, American Society of Civil Engineers", 1940
- [6]. Sailendra N. S., "Ancient Indian History and Civilization", January 1999
- [7]. Adornado, H. A. and Yoshida, M.: "GIS-based watershed analysis and surface run-off estimation using curve number (CN) value, J. Environ. Hydrol.", 2010
- [8]. Kousari, M.R.. "Sensitivity analysis and impact quantification of the main factors affecting peak discharge in the SCS curve number method: An analysis of Iranian watersheds", Quaternary International, October 15, 2014.
- [9]. USDA, Soil Conservation Services, "National Engineering Handbook, Section 4: Hydrology, Soil Conservation Service", 2004.
- [10]. Victor M. P. "Engineering Hydrology, Principal and Practices" 1989
- [11]. A. Osman Akan and Robert J. H., "Urban Hydrology, Hydraulics and Stormwater Quality", 3rd Edition, 2003.
- [12]. David B. Thompson, "The Rational Method", January 2007.

Study Of Strenth Charataristic Of Black Cotton Stablizing With Fly Ash And Rice Husk Ash

Anil Kumar Singhai¹, Sudhanshu Shekhar Singh²,

¹ Professor, Government Engineering College, Jabalpur MP

² ME Student, Government Engineering College, Jabalpur MP

ABSTRACT:

Expansive soils also known as swelling soils or shrink-swell soils are the terms applied to those soils, which have a tendency to swell and shrink with the variation in moisture content. As a result of which significant distress in the soil occurs, causing severe damage to the overlying structure. During monsoons, these soils imbibe water, swell, become soft and their capacity to bear water is reduced, while in drier seasons, these soils shrinks and become harder due to evaporation of water. These types of soils are generally found in arid and semi-arid regions of the world and are considered as a potential natural hazard, which if not treated well can cause extensive damages to not only to the structures built upon them but also can cause loss of human life. Soils containing the clay minerals montmorillonite generally exhibit these properties. The annual cost of damage to the civil engineering structures caused by these soils are estimated to be £ 150 million in the U.K., \$ 1,000 million in the U.S. and many billions of dollars worldwide. In this paper soil is treatd with different proportion of FA(5%,10%,15%,20%,25%) and RHA (,10%,15%,20%,25%,30%) and Optimum moisture content, Maximum dry density and california bearing capacity is evaluated. Test was conducted on BC soil and soil, Fly Ash, Rice husk ash mixtures prepared at optimum water content. Addition of Fly ash and Rice husk ash resulted in appreciable increases in CBR of soil. CBR value is used to reduce the thickness of pavement and increasing the bearing capacity of soil.

KEYWORDS: - CBR, OMC, MDD, Expansive soil, Fly ash, Rice husk ash, Stabilization

I. INTRODUCTION:

Stabilization is one of the methods of treating the expansive soils to make them fit for construction. Variety of stabilizers may be divided into three groups (Petry 2002): (a) traditional stabilizers (lime, cement etc.), (b) by-product stabilizers (fly ash, quarry dust, phosphor-gypsum, slag etc.) and (c) non-traditional stabilizers (sulfonated oils, potassium compounds, polymer, enzymes, ammonium chlorides etc.). Disposal of large quantities of industrial by products as fills on disposal sites adjacent to industries not only requires large space but also create a lot of geo-environment problems. Attempts are being made by various organizations and researchers to use them in bulk at suitable places. Stabilization of expansive soil is one way of utilization of these by products. Some of the research work conducted by earlier researchers on the above has been described. In recent times, with the increase in the demand for infrastructure, raw materials and fuel, soil stabilization has started to take a new shape. With the availability of better research, materials and equipment, it is emerging as a popular and cost-effective method for soil improvement. Soil improvement plays a vital role in geotechnical engineering because it is the only way to stabilize and enhance the properties of soils over the times, cement and lime are the two main materials used for stabilizing soils. These materials have rapidly increased in price due to the sharp increase in the cost of energy since 1970s (Neville, 2000). The over dependence on the utilization of industrially manufactured soil improving additives (cement, lime etc), have kept the cost of construction of stabilized road financially high.

Ravine M. Tailor¹, Dr. M. D. Desai² has already discussed in IGC 2009 utilization of rice husk ash and fly ash of sub grade having majority of black cotton soils the study shows average soaked CBR of west Gujarat is 2% the aim behind modified design was to reduce the annual maintenance expenditure for flexible pavement & standardized design for city roads. Typical pavement designs for different category of roads were developed by authors with Lime – Fly ash stabilization technique to improve the sub grade CBR. The design achieved the reduced annual maintenance expenditure with more durable road sub grade[1] Dr. Robert M. Brooks¹ has also discussed in December 2009 IJRRAS use of rice husk ash and fly ash is to upgrade expansive soil as construction material remolded expansive clay was blended with RHA and fly ash and strength tests were conducted.

The potential of RHA-fly ash blend as a swell reduction layer between the footing of a foundation and sub grade was studied. In order to examine the importance of the study, a cost comparison was made for the reparation of the sub-base of a highway project with and without the admixture stabilizations. Stress strain behavior of unconfined compressive strength showed that failure stress and strains increased by 106% and 50% respectively when the fly ash content was increased from 0 to 25%. When the RHA content was increased from 0 to 12%, Unconfined compressive stress increased by 97% while CBR improved by 47%.

Dr. S.M. prasanna Kumar¹ Indian geotechnical conference – 2010 has already discussed use of fly ash for soil stabilization attributes to the chemical composition and physical characteristics of fly ash, which Favor pozzolana reactions. The major chemical compounds present in fly ash contribute active role in chemical reactions with constituents of soil are calcium Ca +and Silica Si - ions. Black cotton soil (BC Soil) and non-Expansive type – Red Earth (RE) are stabilized using pozzolana fly ash – nyveli lignite fly (NFA) ash and non-Pozzolana fly ash – raichur fly ash (RFA) mixed at different doses along with supplementing additives like lime and cement. The maximum dry density of the BC soil increased from 3.6 to 15.2 KN/m³ for addition of 40% NFA. For Red earthed changed from 14.6 to 17.8 KN/m³ for NFA Addition. Pozzolana fly ash has shown considerable Earth, for addition of 30% of fly ash, NFA.

Saranjeet Rajesh Soni¹, P.P Dahale², R.M Doble³ has discussed IJAEST Vol-No-7, Issue-No-2 economical and effective way to achieve improvement in engineering performance of black cotton soils (B. C. soil). Attempts were made to increase the stability of soil using fly ash (FA) and rice husk powder (RHP). The UCS of natural soil is 198Kpa which is increased after the addition of FA (10%) and RHP (10%) with addition with10% of lime for the period of 28 days curing to 253 kpa. Plasticity Index was reduced to 15.74%, Liquid limit reduces to 35.85%, and Plastic limit reduces to 28.04% after addition of FA (10%) and RHP (10%) with addition with10% of lime for the period of 28 days curing.[4] Alhassan (2008) again carried out experiments to study the effect of stabilizing A-7-6lateritic soil (CH) with 2-12% RHA by weight of dry soil. CBR and UCS tests were conducted for the soil RHA composites. The results obtained indicate a general decrease in the maximum dry density and increase in optimum moisture content. There was also slight improvement in the CBR and UCS values with increase in RHA content. Peak UCS values were recorded at between 6-8% RHA content, indicating a little potential of using 6-08% RHA for strength improvement of A-7-6 lateritic soil.[5]

II. MATERIALS AND METHOLOGY:

Black Cotton Soil :It is collected from Patan Road District Jabalpur Madhya Pradesh from ground having coordinates 21.2191° N, 81.3065° E. soil sample is collected from location of Sukkha village, Power grid Office and near bypass of Jabalpur Patan road. Soil Sample is collected 1 meter below the original depth then collected into bag and send into the laboratory for examination

Rice husk ash : IT is collected from virat vidut limited rice husk ash based Bio-Mass Power Plant at Bilaspur (C.G.),

Fly ash : IT is collected from satpura thermal power station MPPGCL Sarni betul Madhya Pradesh. Properties of black cotton soil define as per BIS standards and properties of black cotton soil, Rice husk ash and fly ash are tabulated on table

Methodology : The soil is collected from patan road Jabalpur (MP) and collects into bags and sends in laboratory for examination. First Index property of soil is determined after then fly ash and rice husk ash mix in different proportions in soil and put Into 28 days for curing. Total five combinations are formed and california bearing ratio, Optimum moisture, Maxisimum dry density is evaluated.

Sr.No	Description of properties	Value
1.	Particle size distribution Sand (%), Silt + Clay (%)	8% 92%
2.	Liquid limits	40% - 100%.
3.	Plastic Limit	25(%)
4.	CBR	1.5-2(%)
5.	OMC (%)	26%
6.	MDD (Kn/m ³)	1.52
7.	Free Swell index	> 50%

Table No.2Oxide composition of RHA.

Sr. No.	Constituent	Composition (%)
1	SiO ₂	75.2
2	Al ₂ O ₃	5.2
3	Fe ₂ O ₃	1.02
4	CaO	1.4

Table No.1 Geotechnical properties of black cotton soil

Properties	Chemical composition of Fly Ash classes	
	FLY ASH CLASSES	
	Class F	Class C
Silicon dioxide (SiO ₂) plus aluminum oxide (Al ₂ O ₃) plus iron oxide (Fe ₂ O ₃), min, %	70.0	50.0
Sulfur trioxide (SO ₃), max, %	5.0	5.0
Moisture Content, max, %	3.0	3.0
Loss on ignition, max, %	6.0	6.0
* The use of class F fly ash containing up to 12% loss of ignition may be approved by the user if acceptable performance results are available		

Rice husk ash : Rice husk is an agricultural waste obtained from milling of rice. About 108 tones of rice husk is generated annually in the world. Meanwhile, the ash has been categorized under pozzolana, with about 67-70% silica and about 4.9% and 0.95%, Alumina and iron oxides, respectively(Oyetola and Abdullah, 2006). The silica is substantially contained in amorphous form, which can react with the CaOH librated during the hardening of cement to further form cementations compounds.

Fly ash : In India, about 76% of electrical energy is generated using coal as fuel in thermal power plants. Presently in India,170 millions of tones of fly is being produced by the of thermal power plants, out of which a vast majority is fly ash having low lime content. Fly ash is a solid waste generated by thermal power plants where coal is used as fuel. As the need of power is increasing with a very fast rate for development purpose, the production of fly ash is increasing rapidly while generating electrical energy by thermal power plant. Disposal of this enormous amount of fly ash faces problem of huge land requirement, transportation, and ash pond construction and maintenance, which can be reduced by utilizing fly ash as a construction material for civil engineering structures.

III. RESULTS:

Soil Sample	Optimum moisture content (%)	Maximum dry dencity (gm/cm3)	Soaked CBR
BC SOIL	13	1.70	1.96
S1(5%FA+10%RHA)	18	1.645	2.86
S2(5%FA+10%RHA)	14	1.70	3.4
S3(5%FA+10%RHA)	15	1.65	2.32
S4(5%FA+10%RHA)	15	1.69	2.66
S5(5%FA+10%RHA)	14	1.52	5.63

Table-3 OMC, MDD, and CBR Values for different soil samples

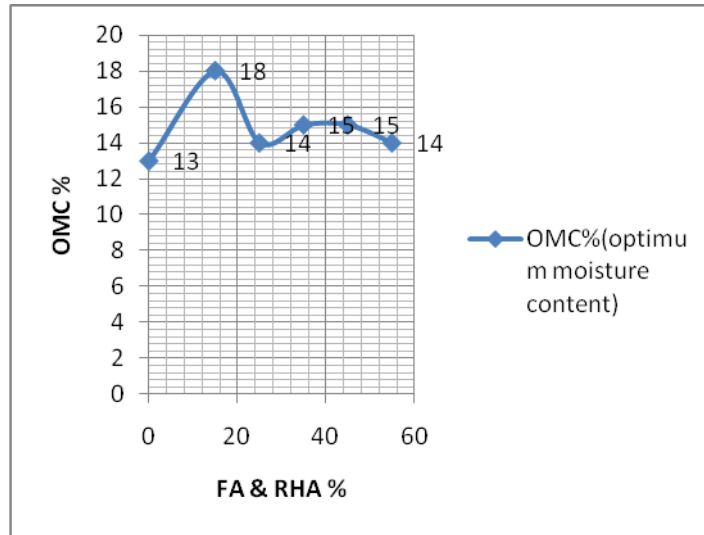


Fig-1 OMC value for BC Soil, Fly ash and Rice husk ash mix soil samples

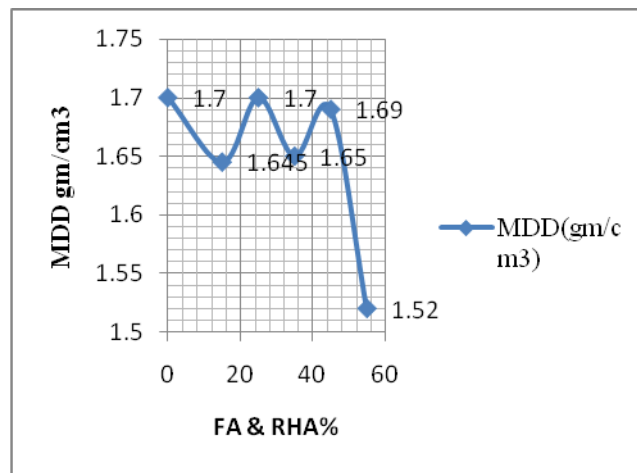


Fig-2 MDD value for BC Soil, Fly ash and Rice husk ash mix soil samples

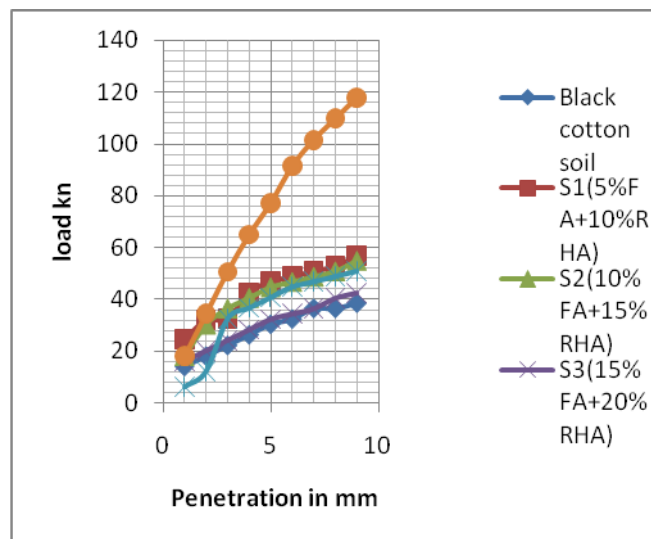


Fig-3 OMC value for BC Soil, Fly ash and Rice husk ash mix soil

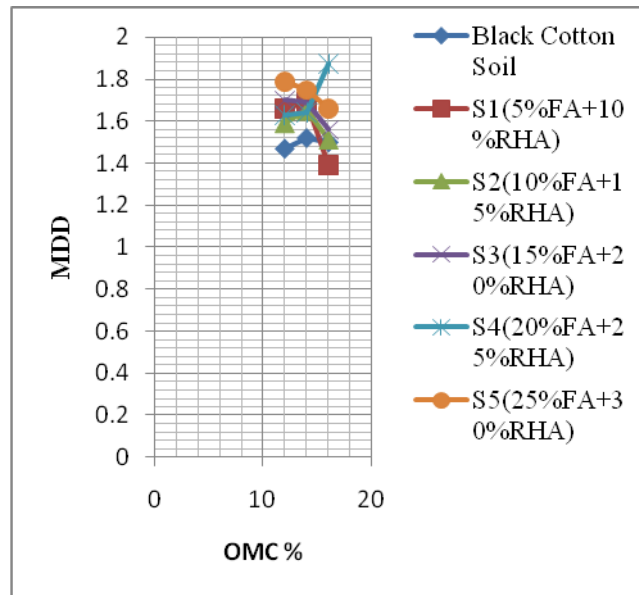


Fig-4 OMC, MDD value for BC Soil, Fly ash and Rice husk ash mix soil

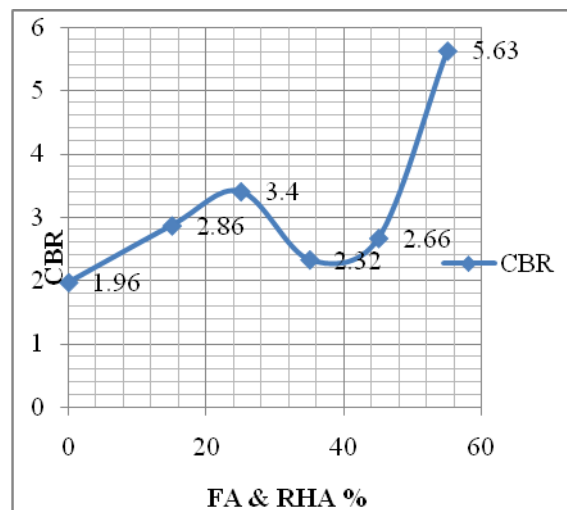


Fig-5 CBR value for BC Soil, Fly ash and Rice husk ash mix soil

IV. CONCLUSION

[1]

It is found that maximum dry density of black cotton soil was 1.70 kn/m^3 for first sample (5%FA+10%RHA) it is reduced to 3.34% for second sample (10%FA+15%RHA) it is increases to 3.2% for third sample (15%FA+20%RHA) it is reduces to 3.03% for fourth sample (20%FA+25%RHA) it is increases to 2.42% for fifth sample (25%FA+30%RHA) it is reduces to 11.18%

[2]

Optimum moisture content is reduces.

[3]

It is found that CBR of black cotton soil for 5mm penetration 1.96% when it replaced with first sample (5%FA+10%RHA) it is increases to 45%. In second sample (10%FA+15%RHA) it is increases to 73% for third sample (15%FA+20%RHA) again it is reduces to 18% for fourth sample (20%FA+25%RHA) it is increases to 35% for last sample (25%FA+30%RHA) it is increases to 287%.

REFERENCES

- [1] S.M. Prasanna Kumar (2012) "Silica and Calcium effect on Geo-Technical Properties of Expansive soil Extracted from Rice Husk Ash and Lime." Proceeding of 2012 International Conference on Environment Science and Engineering, vol.32, 119-123.
- [2] Kiran R. ¹ G Kiran². L² Analysis of Strength characteristics of Black Cotton Soil Using Bagasse Ash and Additives as Stabilizer In this study behavior of black cotton soil 9n IJERT July-2013 Volume 3, Issue 2, July- December (2012), pp. 347-352
- [3] Muntohar, S., and Hantoro, G., (2000), "Influence of Rice Husk Ash and Lime on Engineering Properties of a Clayey Sub-grade", Electronic Journal of Geotechnical Engineering, Vol. 5.

- [4] Brooks, R. M., (2009), "Soil Stabilization with Fly ash and Rice Husk Ash", International Journal of Research and Reviews in Applied Sciences, Volume 1, Issue 3, pp. 209-217.
- [5] Koteswara Rao, D., "Stabilization of Expansive Soil with Rice Husk Ash, Lime and gypsum", International Journal of Engineering Science and Technology (IJEST) ISSN: 0975-5462 Vol. 3, No. 11 November
- [6] A Srirama Rao et al (2008) "Swell-Shrink Behavior of Expansive Soils under Stabilized Flyash Cushions." Proceeding of 12th International Conference of International Association for
- [7] Computer Methods and Advances in Geomechanics (IACMAG), 1539-1546.
- [8] Ito, K. K, Singe, M., Adomako, J. T., and Afandi, (2008), "Amendment of Soil Physical and Biological Properties Using Rice Husk and Tapioca Wastes", Journal of Jpnanesese Society of Soil Physics, No. 108, pp. 81-90.
- [9] Erdal Cokca (2001) "Use Of Class C Fly Ashes for the Stabilization – of an Expansive Soil" Journal of Geotechnical and Geo environmental Engineering Vol. 127, July, pp. 568-5
- [10] Singh G., Singh J., (1991), "Highway Engineering", Standard Publishers Distributors, Nai, Sarak, India, p. 608-610.

Study of Velocity and Pressure Distribution Characteristics Inside Of Catalytic Converter Geometry With Fluent 2D – Modeling & Simulation

D. K. Sakhare¹, S.L.Sinha² and S.P.Singh¹

¹ CSIR-Central Institute of Mining & Fuel Research, Nagpur Unit-II, NAGPUR-440 001,

² Department of Mechanical Engg, National Institute of Technology, RAIPUR -492 010.

ABSTRACT:

Catalytic Converters used in modern days Automobiles play a very important role towards reducing the harmful pollutants entering into our local environment. The efficiency of Catalytic converter solely depends upon the Geometry & Catalyst elements used. This paper reports the investigation made on two designs of Catalytic converter geometry namely Cylindrical & Convergent-Divergent shape. The Velocity & Pressure drop characteristics inside the converter have been described by using FLUENT 2D-Modeling flow through Porous media. GAMBIT was used as pre-processing tool for geometry creation & meshing. The detail study shows that the Cylindrical Catalytic converter creates more pressure drop as compared to the Convergent-Divergent shape and the NO_x conversion efficiency is also high in the Cylindrical Catalytic converter. The simulation results of Velocity variation & Pressure drop characteristics in these two geometries are validated with the laboratory results.

KEYWORDS: Catalytic Converter, DeNO_x catalyst, Modeling & Simulation, Porous media, GAMBIT, FLUENT-CFD

I. INTRODUCTION

Air pollutants emitted from the Transport sector is the second largest source after the Industrial sector. Major pollutants emitted from Automobiles are CO, HC, NO_x and PM (Smoke). 3-Way Catalytic converters are being used in Petrol driven vehicles for reducing these pollutants from the exhaust stream. After the invention of Catalytic converter by Eugen Haudry in the year 1930, much advancement is being done worldwide in the area of Catalytic Converter geometry, Catalytic elements, Catalyst types, Substrate material & Catalytic elements loading process over the substrate materials. Catalytic converter poses certain problems like back pressure which reduces engine efficiency, nonuniform flow, which reduces the Catalytic converter efficiency. Also the Catalytic material must be sufficient to treat the pollutants to meet the emission norms. As per the investigation made by Pannone et al [1] an Engine may lose about 300 W of power per 1000 Pa drop in pressure. Therefore, a trade-off between pressure drop & amount of catalyst or total catalytic surface area required has become the main concern for the geometry of Catalytic converters. Design optimization studies of automotive exhaust systems are carried out by Lakshmikantha *et al.* They optimized exhaust system design parameters such as shape and profile of manifold, catalyst inlet tube, inlet cone, exit cone, and exit tube under a given exhaust gas conditions. Amirnodin *et al* [3] adapted sub-grid scale modeling to predict the pressure loss of square cell shape of the honeycomb monolith structure for Catalytic converter. This sub-grid scale modeling represents the actual variation of pressure drop between the inlet and outlet for various combinations of wall thickness and cell density. The comparison is being made to the experimental and numerical work established in the literature. The sub-grid scale modeling gives better agreement in pressure drop compared to the numerical work using single channel approach.

Subramanyeswararao (2014) has investigated the effect of geometric parameters on the performance of automotive catalytic converters. He has studied the effect of fluid flow due to geometry change by using FLUENT 6.0. The increase in inlet cone angle increases the vorticity of the flow, which leads to inactive zones and increase inlet cone length reduces the recirculation zones. Back pressure decreases as angle of the inlet cone decreases upto 300 and diameter of substrate increases. The exhaust emission decreases with the increase in catalyst diameter and increase in catalyst length [4]. Patil, *et al* (2013) has focused on reducing the back pressure in the exhaust system to increase the combustion efficiency by using FLUENT CFD. In CFD analysis various diffuser models with different angles were simulated by using appropriate boundary conditions and fluid properties [5]. Karuppuswamy *et al* (2013) in their study aimed for more filtration efficiency with limited back pressure. They have simulated various models with different wire mesh grid size using the appropriate boundary conditions and fluid properties. Through CFD analysis, the vorticity and back pressure of various models were studied. The increase in inlet cone angle increases vorticity of flow, which leads to inactive

zone and reduces the back pressure. They have also found that installation of catalytic converter reduces the back thermal efficiency and increases the brake specific fuel consumption and fuel flow rate [6]. K. Mohan Laxmi *et al* (2013) has studied the effect of change in inlet fluid (Nitrogen gas) velocity on the pressure & the velocity distribution inside the catalytic converter [7].

II. GEOMETRY

The two designs of Catalytic converter for the study are as shown below:

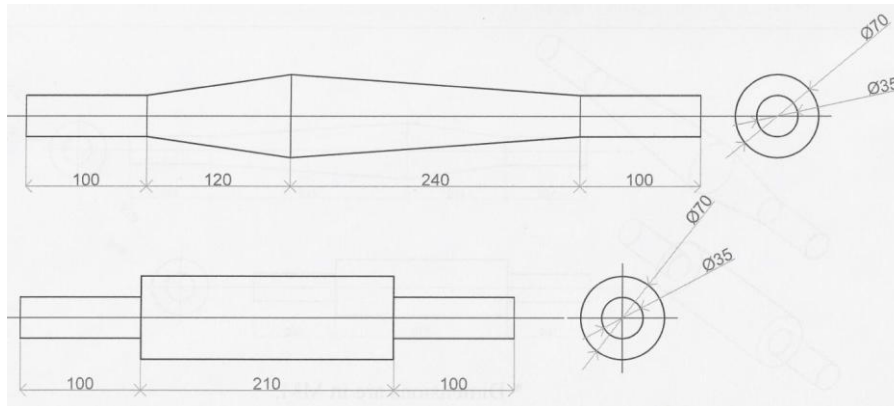


Fig 1 Catalytic converter drawing (All dimensions are in mm)



Fig 2 Actual Catalytic converters (Cylindrical & Convergent-Divergent shape)

III. CFD SIMULATION BY FLUENT

The 2D model of these catalytic converters is modeled by using GAMBIT which is a preprocessor for FLUENT. The quadrilateral mapped mesh is generated and the mesh is examined for its quality. After examining the mesh quality, the FLUENT 5/6 solvers are chosen and the boundary type conditions and continuum conditions are given. Then the boundary zone assigned model is exported as the 2D mesh file.

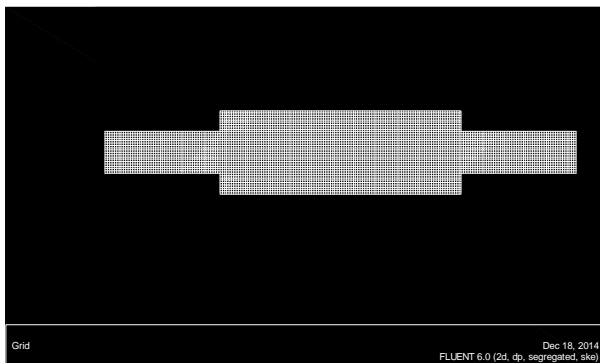


Fig 3 2D- Mesh file of Cylindrical Catalytic Converter

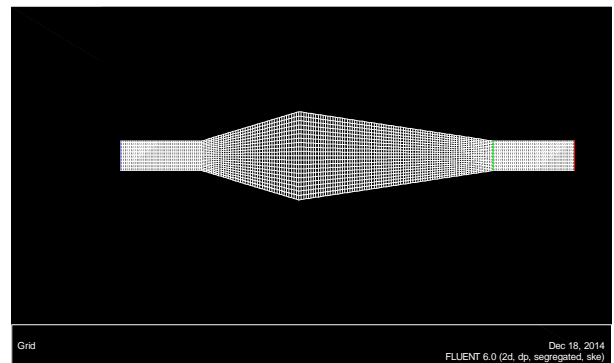


Fig 4 2D- Mesh file of Con-Div Catalytic Converter

A 2D segregated solution method, implicit solution formulation and a steady state flow is opted with absolute velocity formulation. The standard $k-\epsilon$ model is selected under the viscous model for the turbulent flow calculation with the standard wall function as the near wall treatment. The energy equation is enabled. The fluid medium is assumed as Nitrogen because it dominates in the vehicular exhaust. The properties of Nitrogen are given in table 1. The inlet velocity is set as 30 m/sec and temperature 300K. The intensity and hydraulic diameter are set for the turbulence specification method and the turbulence intensity is taken as 5. At the outlet the pressure is set as 0 gauge pressure. The substrate region is treated as the laminar and porous zone. The viscous & inertial resistance values of porous material are given as in table 2 and boundary conditions are given in table 3.

Convergence is being done using absolute criterion of $1e-5$. Solution methods-Spatial discretization, Gradient- least square cell based, Pressure-standard, Momentum. Turbulent kinetic energy and turbulent dissipation rate are taken at second order upwind, Surface monitors report with respect to mass flow rate at outlet and solution is initialized & computed from exhaust gas inlet. Solution is run for 200 iterations. It was seen that the solution converge at about 90-160 iterations. The porous region is first considered as empty and then filled (i.e. Porous not applied and applied). At 30 m/s fluid (Nitrogen) velocity simulation is done for these two cases. Velocity and Pressure contours are created as well as X-Y plots are generated at the axis.

Table 1 Fluid (Nitrogen) properties

Density	1.136 Kg/m ³
Viscosity	1.663 e- ⁰⁵ Kg/m-s

Table 2 Porous media properties

	Viscous resistance (1/m ³)	Inertial resistance (1/m)
Direction 1	3.846e ⁺⁰⁷	20.414
Direction 2	3.846e ⁺¹⁰	20414

Table 3 Boundary conditions

Boundary	Assigned as
Inlet	Velocity Inlet
Outlet	Pressure Outlet
Wall	Wall

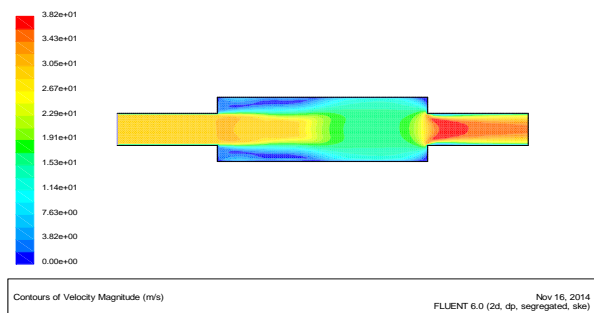


Fig 5 Velocity contour: Cylindrical Cat Con (Empty)

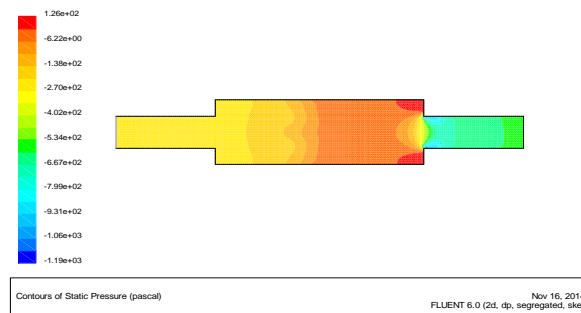


Fig 6 Pressure contour: Cylindrical Cat Con (Empty)

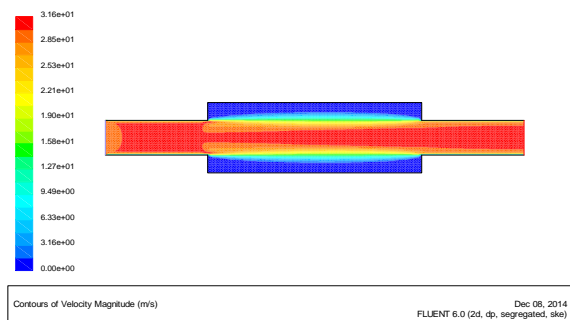


Fig 7 Velocity contour: Cylindrical Cat Con (Filled)

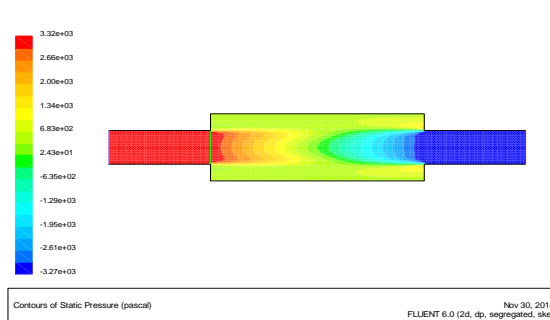


Fig 8 Pressure contour: Cylindrical Cat Con (Filled)

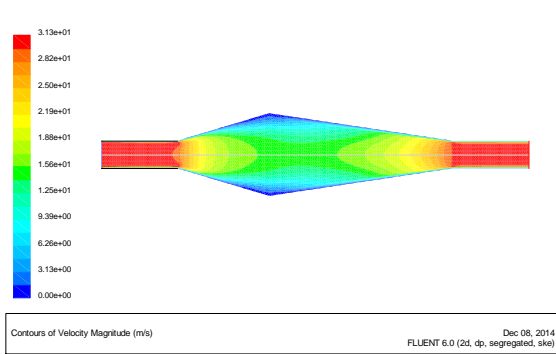


Fig 9 Velocity contour: Cov-Div Cat Con (Empty)

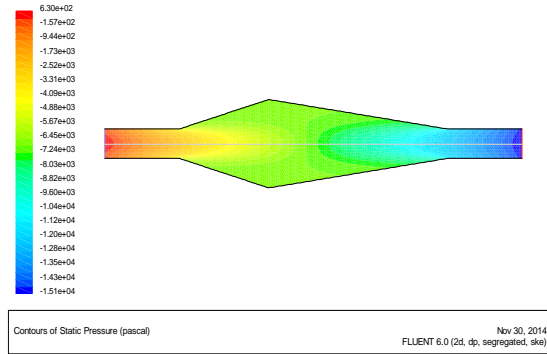


Fig 10 Pressure contour: Con- Div Cat Con (Empty)

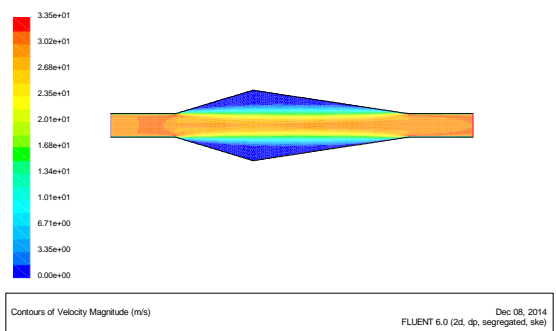


Fig 11 Velocity contour: Con-Div Con (Filled)

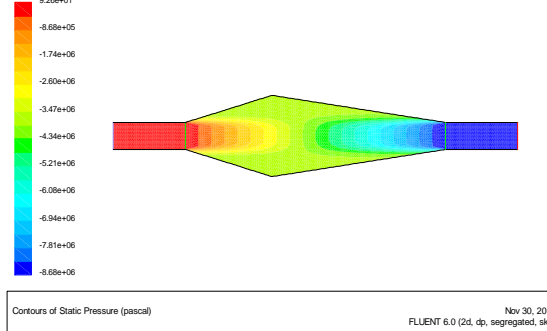


Fig 12 Pressure contour: Con-Div Cat Con (Filled)

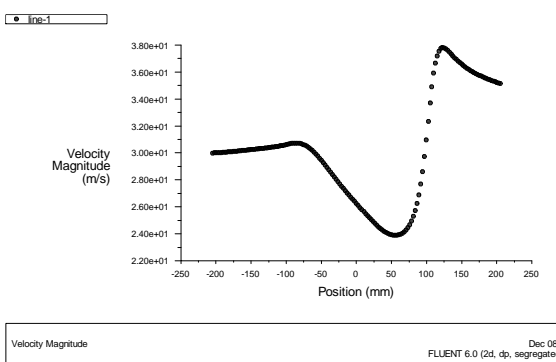


Fig 13 Velocity magnitude: Cylindrical (Empty)

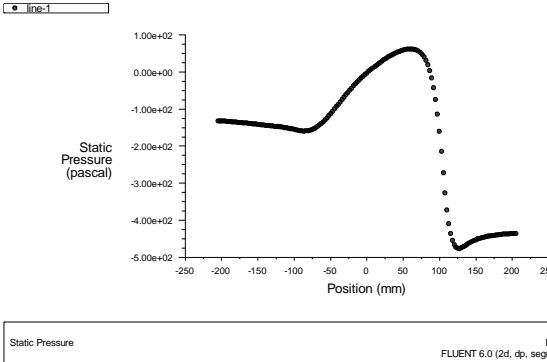


Fig 14 Static Pressure: Cylindrical (Empty)

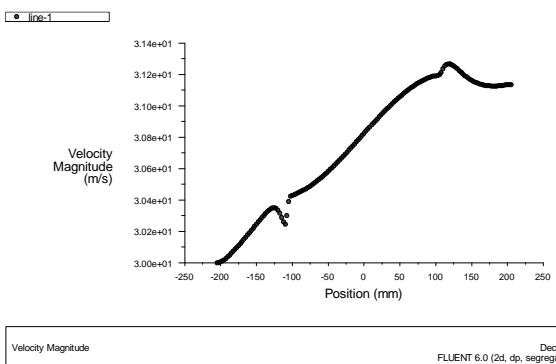


Fig 15 Velocity magnitude: Cylindrical (Porous)

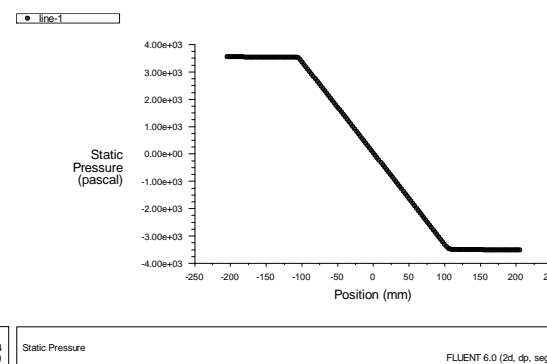
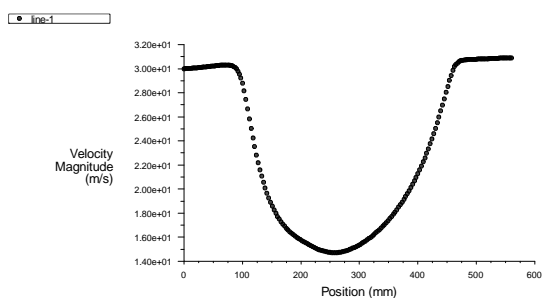
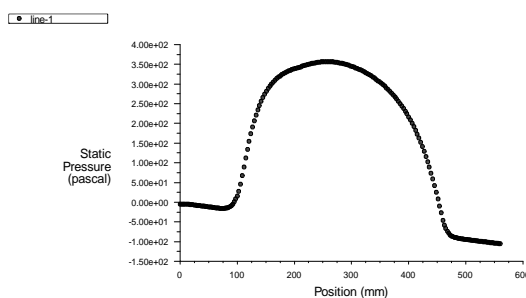


Fig 16 Static Pressure: Cylindrical (Porous)



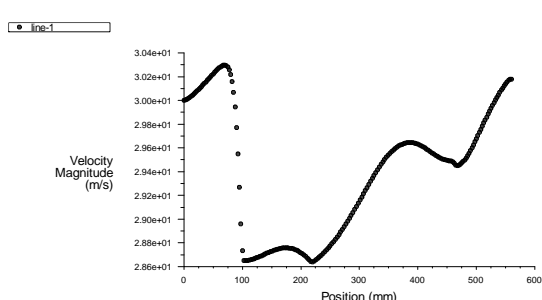
Velocity Magnitude Dec 08, 2014
FLUENT 6.0 (2d, dp, segregated, ske)



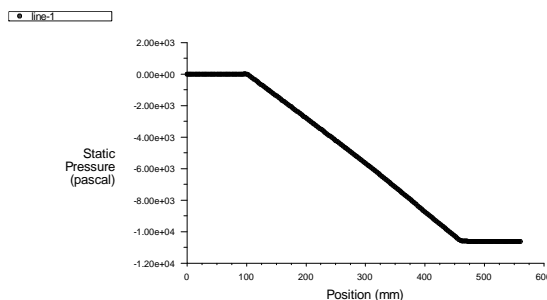
Static Pressure Dec 08, 2014
FLUENT 6.0 (2d, dp, segregated, ske)

Fig 17 Velocity magnitude: Con-Div (Empty)

Fig 18 Static Pressure: Con-Div (Empty)



Velocity Magnitude Dec 08, 2014
FLUENT 6.0 (2d, dp, segregated, ske)



Static Pressure Dec 08, 2014
FLUENT 6.0 (2d, dp, segregated, ske)

Fig 19 Velocity magnitude: Con-Div (Porous)

Fig 20 Static Pressure: Con-Div (Porous)

IV. EXPERIMENTAL VALIDATION

To validate experimentally, the pressure drop variation in these two designs of Catalytic converters, an experimental setup is created which has an air compressor. The Catalytic converter empty and filled with catalyst pellets were fitted alternately to the air outlet having a control valve. Air velocity was fixed to 30 m/s with the help of this control valve. Air velocity was measured by a vane type anemometer. 2" long and 1/4" diameter copper tubes were soldered at the three locations of the catalytic converter body; one at entry, one at the middle and another at the exit of porous zone. The pressure drop was measured with the help of a glass U-tube manometer in terms of mm of water column and thereafter the pressure drops were converted into Pascal. The Simulation & Experimental results are tabulated in table 4 and table 5.

Table 4: Simulation Result of Empty & Filled Catalytic Converter

	Empty				Porous				
	Cylindrical		Convergent-Div		In	Cylindrical		Convergent-Div	
	V (m/s)	Δp (Pa)	V (m/s)	Δp (Pa)		V (m/s)	Δp (Pa)	V (m/s)	Δp (Pa)
In	30	-150	31	-25	In	30.4	3500	30.3	0
Mid	26	50	15	350	Mid	30.7	0	29.0	-500
Out	38	-450	31	-100	Out	31.3	-3500	31.1	-1000

Table 5: Experimental Result of Empty & Filled Catalytic Converter

	Empty				Porous				
	Cylindrical		Convergent-Div		In	Cylindrical		Convergent-Div	
	V (m/s)	Δp (Pa)	V (m/s)	Δp (Pa)		V (m/s)	Δp (Pa)	V (m/s)	Δp (Pa)
In	30	-141	30	0	In	30.0	3360	30.0	0
Mid	-	-40	-	380	Mid	-	0	0	-410
Out	33	-410	27	-130	Out	29.5	-3410	28.4	-960

V. CONCLUSION

From the result Table 4 and Table 5; it is seen that the Simulation & Experimental results are validated within narrow limits. It can also be concluded that the cylindrical catalytic converter has more pressure drop as compared to the Convergent-Divergent Catalytic converter. Therefore, the residence time, i.e. reaction time for pollutant with the Catalyst will be more. Thereby, the cylindrical catalytic converter is more effective for pollutant reduction from the exhaust stream of any vehicle. The authors have also conducted experiments with their own prepared catalyst. We have prepared and tested 5% Silver & 5% Iron loaded catalysts over γ -Alumina support and tested in the exhaust stream of Jeep (M & M make). The converters were heated externally by an electrical heating tape at temperature of 280°C. The maximum NO conversion of 36.36% achieved under full acceleration with the cylindrical catalytic converter. When the experiment was conducted in Convergent-Divergent catalytic converter filled with 5% Silver catalyst the NO conversion slightly reduces to 31.41%. This is because the convergent-divergent shape gives less resistance in the flow of exhaust gases and consequently, the residence time is less for the reaction of nitric oxide gas with catalyst. Similarly, when 5% Iron catalyst was tested in cylindrical catalytic converter the NO conversion was 27.08% and with Convergent-Divergent catalytic converter it was 25.25%. Graphical representations of the NO conversion efficiency of 5% Silver & 5% Iron catalysts with Cylindrical & Convergent-Divergent catalytic converter is shown in Fig 21.

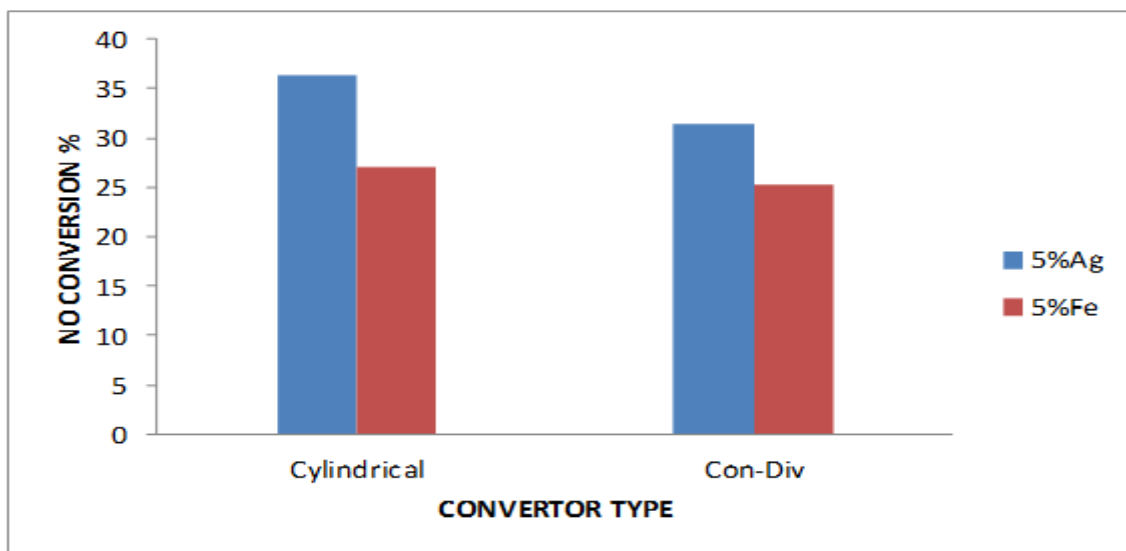


Fig 21: Type of catalytic converter V/s NO conversion%

VI. ACKNOWLEDGEMENTS

The Authors acknowledge the help of Sri Sanjiv B. Thool, Asstt. Professor, Department of Mechanical Engineering, Rungta College of Engineering & Technology, Bhilai (Chhattisgarh) for Computer Simulation of Catalytic Converters. Help of Sri Rahul Mehatre, Ms. Swati Singh, Sri Pravin Kotangle and Sri Pankaj Shahare is also acknowledged during various stages of the studies.

REFERENCES

- [1] G.M.Pannone and J.D.Muller, A comparison of conversion efficiency and flow restriction performance of ceramic and metallic catalyst substrate, SAE International, 2001-01-0926, 2001.
- [2] M.Lakshmikantha and M.Keck, Optimization of exhaust system, SAE International, 2002-01-0059, 2002.
- [3] S.H.Amirnordin, S.Seri, W.S.Salim, H.A.Rahman and K. Hasnan; Pressure drop prediction of Square cell Honeycomb Monolith structure; Int. Conference on Environmental Science and Engineering, IPCBEE, Vol 8 (2011).
- [4] P.K.V.S.Subramanyeswararao ,CFD studies in Catalytic Converter, International Journal of Applied Research and Studies, Vol-3, Issue 6, June 2014, pp1-15.
- [5] Atul A. Patil, L.G.Navale and V.S.Patil, Simulative analysis of single cylinder 4-stroke CI engine exhaust system, PRATIBHA: International journal of Science, Spirituality, Business & Technology, Vol 2, No 1, Nov 2013, pp79-82.
- [6] P. Karuppuswamy and R.Senthil; Design, Analysis of flow characteristics of catalytic converter and effects of back pressure on engine performance, International journal of Research in Engineering & Advanced technology, Vol 1, Issue 1, March 2013, pp 1-6.
- [7] K.Mohan Laxmi, V.Ranjith Kumar and Y.V.Hanumantha Rao, Modeling and Simulation of different gas flow, velocity and pressure in catalytic converter with porous, International Journal of computational Engineering research, Vol 03, Issue 4, April 2013, pp 28-41.

Audio Noise Removal – The State of the Art

Srinidhi S Shetty¹, Reeja S R²

¹ PG Scholar, Dept. of Computer Science and Engineering, NMAM Institute of Technology, Nitte, India

² Research Scholar, Dept. of Computer Science and Engineering, VTU, Belgaum, India

ABSTRACT:

In this paper different audio denoising techniques are discussed. Most of the audio denoising techniques reduce Gaussian white noise from audio signals. Diagonal estimation techniques and non diagonal estimation techniques are discussed. Different audio denoising techniques and noises are shown through the taxonomy.

KEYWORDS: audio denoising, diagonal estimation, Gaussian noise, musical noise, non diagonal estimation, thresholding, White noise

I. INTRODUCTION

Audio is corrupted by different types of noise during acquisition of audio. The aim of noise removal from audio is to attenuate the noise without modifying the original signal. Various applications of audio denoising are music and speech restoration. Diagonal estimation techniques and non diagonal estimation techniques are two types of audio denoising techniques. To attenuate the noise from audio signals diagonal time-frequency audio denoising algorithms process each spectrogram coefficient independently. The drawback of these algorithms are they have a limited performance, denoised signal contains musical noise, denoised sound is contaminated and the audio perception is degraded due to the superposition of musical noise. To overcome these drawbacks non diagonal estimation techniques are required [6], [7], [11].

II. AUDIO DENOISING - RELATED WORKS

Wavelet based algorithm for audio denoising is discussed in paper [1]. The authors focused on audio signals corrupted with white noise. White noise is especially hard to remove because it is located in all frequencies. The authors used Discrete Wavelet Transform (DWT) to transform noisy audio signal in wavelet domain. It was assumed that signal is represented by high amplitude DWT coefficients and noise is represented by low amplitude coefficients. To get audio signal with less noise, thresholding of coefficients are used and they are transformed back to time domain. The authors proposed modified universal thresholding of coefficients which results with better audio signal. Objective Degree Grade (ODG) was main criterion for evaluation of experimental results. The authors have also compared ODG with Mean Square Error (MSE) which is widespread used for estimating signal quality. Results show that MSE shows little enhancement or even loss while ODG and also informal listening tests prove significant enhancement of signal quality. This denoising algorithm worked better for lower noise signals but for higher noise signals higher threshold must be set, but except noise part of original signal is also removed by it causing audible artifacts in denoised signal.

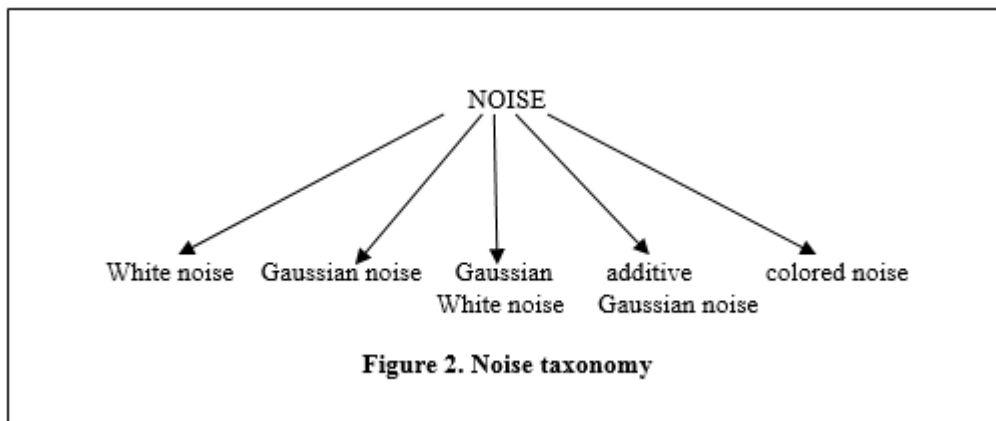
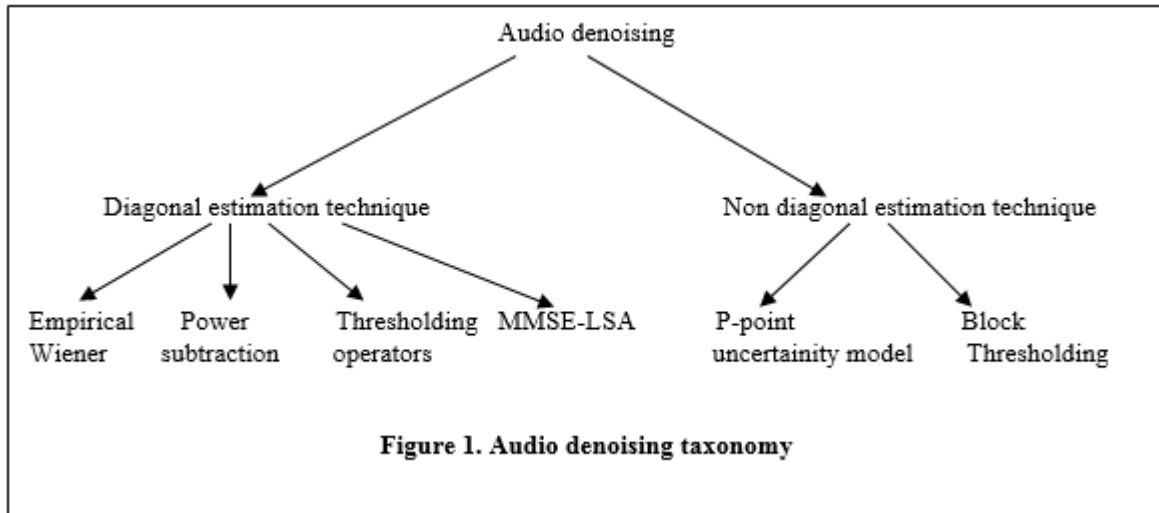
In paper [2], block attenuation methods that were initially applied in orthogonal wavelet signal representations [3] is investigated by authors. Block size as well as thresholding level in redundant time-frequency signal representations is studied by authors and they found that the remaining noise artifacts in restored signals is eliminated by block attenuation and provides a good approximation of the attenuation with oracle. A connection between the block attenuation and the decision-directed a priori SNR estimator of Ephraim and Malah is studied by authors. An adaptive block technique based on the dyadic CART algorithm [4, 5] is introduced by authors. The experiments show that the remaining noise artifacts is eliminated and transients of signals are preserved by the proposed method better than the methods which use short-time Fourier do [2]. The experiments were performed on speech signals sampled at 11 kHz. These speech signals were corrupted by white Gaussian noise. The performance of block attenuation is good when compared with the performance of other methods such as Adaptive Block Attenuation with Complex Wavelets, Hard Thresholding with Complex Wavelets, Ephraim and Malah decision-directed a priori SNR estimator + Wiener with Complex Wavelets / Short-Time Fourier. A number of experiments were performed on various music signals also.

The performance of adaptive block attenuation is good when compared with the performance of conventional thresholding operators. Sharper note transitions is obtained than the estimate with short-time Fourier. However, denoising using short-time Fourier performs better than the wavelet counterpart for the stationary parts when high pitch is involved because in high frequency bands short-time Fourier has higher frequency resolution than wavelet representation. In paper [8], denoising problem is considered from the viewpoint of sparse atomic representation. The authors proposed a general framework of time-frequency soft thresholding which encompasses and connects well known shrinkage operators as special cases. Convergence of the corresponding algorithms is numerically evaluated and their performance in denoising real life audio signals is compared to the results of similar existing approaches. The novel approach is competitive with respect to signal to noise ratio and improves the state of the art in terms of perceptual criteria. From the denoising point of view the neighborhood weighting could be considered as non diagonal estimation. Musical noise naturally arising in diagonal estimation is reduced by these approaches.

In paper [9], significant improvements in audio denoising is obtained by exploiting the persistence properties of signals. In this contribution, a novel denoising operator based on neighborhood smoothed, Wiener filter like shrinkage is derived. The purpose of the paper is concerning the operator design and derives a novel audio denoising operator, the persistent empirical Wiener estimate, which fuses recent developments in the field of structured sparsity with the properties of empirical Wiener filtering. According to a given performance criterion a rationale for adaptive threshold selection is proposed. Compared to the optimal thresholds a plain linear model depending on the level of the noise achieves minor performance differences. A simple method for estimating this noise level in case it is unknown is proposed. The proposed operators perform competitively compared to the state of the art, while being much more computationally efficient and robust to minor perturbation of the noise level. The method presented in [10] is based on the Singular Value Decomposition (SVD) of the frame matrix representing the signal in the Overlap Add decomposition. Both the singular values and the singular vectors of the representation are modified to perform denoising. For the former a tapering model is used and for the latter a nonlinear PDE method is used. The aim of the proposed technique is to reduce additive random noise which has corrupted the signal. To test this method the authors performed tests on a variety of sounds from speech and music after corrupting them with additive gaussian noise. The authors used the sampling rate 16 kHz for speech and 44.1 kHz for music. The authors compared their method with Savitzky-Golay filter in terms of MSE and SNR. Results show that performance of their method is good in reducing noise from signal.

In paper [11], the method used is non diagonal in which block parameters are automatically adjusted to the nature of the audio signal. This is done by minimizing a Stein estimator of the risk which is calculated analytically from noisy signal values. Block thresholding method is used to eliminate musical noise. This block thresholding method performs attenuation of time-frequency coefficients after grouping the time-frequency coefficients in blocks. In diagonal time-frequency audio denoising algorithms there is lack of time-frequency regularity because of which it create isolated time frequency structures. This isolated time frequency structures are interpreted as musical noise. Block thresholding is used for audio time frequency denoising which regularizes the estimate and musical noise is reduced efficiently. In paper [12], Adaptive time-frequency Block Thresholding procedure using discrete wavelet transform is used to reduce the noise from the audio signal and to achieve better SNR of the audio signal. For audio signal denoising discrete-wavelet transforms based algorithms are used. For denoising both soft thresholding and hard thresholding are used. In the paper the authors compared the results of soft thresholding and hard thresholding. Results showed that performance of soft thresholding is better than performance of hard thresholding.

Matching Pursuit (MP) is a greedy algorithm that iteratively builds a sparse signal representation. An analysis of Matching Pursuit in the context of audio denoising is presented in the work [13]. The algorithm is interpreted as a simple shrinkage approach, the authors identified factors critical to its success and several approaches to improve its performance and robustness is proposed. The authors have presented experimental results on a wide range of audio signals and shown that the method is able to yield results that are competitive with other audio denoising approaches. The authors introduced a new audio denoising approach called Greedy Time-Frequency Shrinkage (GTFS) that is able to produce competitive denoising results in terms of standard performance metrics, Signal to Noise Ratio (SNR) and Perceptual Evaluation of Audio Quality (PEAQ). The authors focused on the removal of uncorrelated Gaussian white noise from music and speech signals. The various audio denoising techniques are shown in the taxonomy of figure 1 where MMSE-LSA is Minimum Mean Square Error Log Spectral Amplitude Estimation algorithm. Different noises are shown in the taxonomy of figure 2.



Performance comparison of Block Thresholding [7], Block Thresholding (BT) with soft thresholding wavelet [12], Block Thresholding (BT) with hard thresholding wavelet [12], Minimum Mean Square Error Log Spectral Amplitude Estimation algorithm (MMSE-LSA) [7], Minimum Mean Square Error Log Spectral Amplitude Estimation algorithm by using Decision Direct method (MMSE-LSA-DD) [7] of Mozart signal for different SNR values is shown in the below table 1.

Table 1. Performance comparison

Signal and SNR	Block Thresholding	BT with soft thresholding wavelet	BT with hard thresholding wavelet	MMSE-LSA	LSA-DD
Mozart 5dB	14.90	11.57	9.84	7.625	7.625
Mozart 10dB	18.31	15.02	12.76	12.625	-
Mozart 15dB	22.03	18.75	15.97	17.727	-
Mozart 20dB	25.14	22.64	19.48	22.825	-
Mozart 25dB	30.29	27.43	23.62	28.785	-

From the above performance comparison table 1, we are concluding that the block thresholding technique is more efficient than other listed techniques because signal to noise ratio value of block thresholding technique is high.

III. CONCLUSIONS

Audio is corrupted by different types of noise during acquisition of audio. The process of removing such noise from audio signals is audio denoising. In this paper different audio denoising techniques are discussed. From the survey, we are concluding that the non diagonal estimation techniques are efficient compared to diagonal estimation techniques as they avoid producing musical noise.

REFERENCES

- [1] Matko Saric, Luki Bilicic and Hrvoje Dujmic, "White Noise Reduction of Audio Signal using Wavelets Transform with Modified Universal Threshold", University of Split, R. Boskovicica b. b HR, volume 21000, 2005.
- [2] Guoshen Yu, Emmanuel Bacry and Stephane Mallat, "Audio Signal Denoising with Complex Wavelets and Adaptive Block Attenuation", IEEE International Conference on Acoustics, Speech and Signal Processing, Volume 3, 2007.
- [3] T. Cai and B.W. Silverman, "Incorporation information on neighboring coefficients into wavelet estimation", Sankhya, 63, 127-148, 2001
- [4] L. Breiman, J. Friedman, R. Olshen, and C.J Stone, Classification and Regression Trees, Belmont, CA: Wadsworth, 1983.
- [5] D. L. Donoho, "CART and best-ortho-basis: a connection", Ann. Statist. 25 1870–1911.
- [6] Guoshen Yu, Stephane Mallat, Emmanuel Bacry, "Audio Denoising by Time-Frequency Block Thresholding", IEEE Transactions on Signal Processing, Vol. 56, No. 5, May 2008.
- [7] Lalitha kumari, Karunakar Reddy, Hari Krishna and Venkata Subash, "Time-Frequency Block Thresholding Approach for Audio Denoising", International Journal of Advances in Science and Technology, Vol. 2, No. 5, 2011.
- [8] Kai Siedenburg and Monika Dorfler, "Audio Denoising by Generalized Time-Frequency Thresholding", Audio Engineering Society Conference: 45th International Conference: Applications of Time-Frequency Processing in Audio, 2012.
- [9] Kai Siedenburg, "Persistent Empirical Wiener Estimation with Adaptive Threshold Selection for Audio Denoising", Proceedings of the 9th Sound and Music Computing Conference, pages 426 - 433, 2012.
- [10] George Baravdish, Gianpaolo Evangelista, Olof Svensson and Faten Sofya, "PDE-SVD Based Audio Denoising", Proceedings of 5th International Symposium on Communications, Control and Signal Processing, IEEE, 2012.
- [11] K.P. Obulesu and P. Uday Kumar, "Implementation of Time Frequency Block Thresholding Algorithm in Audio Noise Reduction", International Journal of Science, Engineering and Technology Research (IJSETR), Volume 2, Issue 7, July 2013.
- [12] S. S. Joshi and Dr. S. M. Mukane, "Comparative Analysis of Thresholding Techniques using Discrete Wavelet Transform", International Journal of Electronics Communication and Computer Engineering, Volume 5, Issue (4) July, 2014.
- [13] Gautam Bhattacharya and Philippe Depalle, "Sparse Denoising of Audio by Greedy Time-Frequency Shrinkage", 2014 IEEE International Conference on Acoustics, Speech and Signal Processing (ICASSP), 2014.

Efficient Load Balancing Routing in Wireless Mesh Networks

S.Irfan

Lecturer, Dept of Electrical and Computer Engineering, KIOT, Wollo University, Ethiopia.

ABSTRACT

In a Wireless Mesh Network (WMN), the traffic load is disseminated unevenly over the network. A load aware routing scheme is introduced to balance the load in the network, and accordingly improve the overall capacity of network. The load aware routing scheme is designed to maximize the utility by using dual decomposition technique. In the proposed scheme, a WMN is divided into multiple clusters to control the load in the network. Cluster has number of nodes, i.e., routers. One node acts as a cluster head. Cluster head estimates the traffic load in its cluster. As the estimated load gets higher, the cluster head increases the routing metrics of the routes passing through the cluster. Based on the routing metrics, user traffic takes a detour to avoid overloaded areas and, as a result, the WMN achieves global load balancing.

INDEX TERMS—Wireless mesh network, load-aware routing, utility, dual decomposition.

I. INTRODUCTION

Mesh networking is a type of networking where in each node in the network may act as an independent router, regardless of whether it is connected to another network or not. It allows for continuous connections and reconfiguration around broken or blocked paths by “hopping” from node to node until the destination is reached. A Wireless Mesh Network (WMN) has many advantages over conventional wired networks, such as low installation cost, wide coverage and robustness, etc. In the WMN users communicate with in the network and communicate with outside network via wired gateways. The gateway is used to connect the different WMN. In this situation links around the gateways are likely to be a overloaded in the network. If the routing algorithm does not control the traffic load on these links, some gateways may be overloaded while others may not. This load imbalance can be resolved by introducing a load-aware routing scheme that adopts the routing metric with load factor.

In this paper, we propose a load-aware routing scheme, which maximizes the total utility of the users in the WMN. The utility is a value which quantifies how satisfied a user is with the network. Since the degree of user satisfaction depends on the network performance, the utility can be given as a function of the user throughput. Generally, the utility function is concave to reflect the law of diminishing marginal utility. To design the scheme, we use the dual decomposition method for utility maximization. Using this method, we can incorporate not only the load-aware routing scheme but also congestion control and fair rate allocation mechanisms into the WMN.

In the proposed routing scheme, a WMN is divided into multiple overlapping clusters. A cluster head takes role of controlling the traffic load on the wireless links in its cluster. The cluster head periodically estimates the total traffic load on the cluster, and increases the “link costs” of the links in the cluster, if the estimated load is too high. In this scheme, each user chooses the route that has the minimum sum of the link costs on it. Thus, a user can circumvent overloaded areas in the network, and therefore, the network-wide load balance can be achieved.

The major advantages of the proposed load-aware routing scheme can be summarized as follows.

- Designed by the dual decomposition method, the proposed load-aware routing scheme maximizes the system-wide performance.
- The proposed scheme is scalable, has low control and computation overheads, and can be easily implemented by means of the existing ad hoc routing protocols.

II. RELATED WORKS

In WMN, a number of routing metrics and algorithm have been proposed to take advantage of stationary topology. the routing metrics are expected number of transmissions(ETX), minimum loss(ML), minimum time metric(MTM), expected transmission time (ETT), weighted cumulative extended transmission time (WCETT), the intra-flow interference (MIC), interference aware (iAWARE), modified extended number

of transmissions (mETX). These routing metrics contain the standard deviation of the link quality in addition to the average link quality. The blacklist forwarding algorithm (BFA), ExOR algorithm, resilient opportunistic mesh routing (ROMER) have been proposed.

The load aware routing protocols incorporate the load factor into their routing metrics. Compared to these load-aware routing protocols, the proposed routing scheme has three major advantages. First, the proposed scheme is designed to maximize the system capacity by considering all necessary elements for load balancing, e.g., the interference between flows, link capacity, etc. Second, the proposed scheme can guarantee fairness between users. Third, the proposed scheme can provide routes stable over time.

We have used dual decomposition method to design the proposed load-aware routing scheme to maximize the network utility. To use this method, we should formulate the optimization problem under the constraints. After the constraints are relaxed by the Lagrange multipliers, the whole problem can be decomposed into small sub problems which are solved by the different network layers in the different nodes. Therefore, the dual decomposition method provides the systematical way to design a distributed algorithm which finds the global optimal solution.

III. SYSTEM MODEL

A Mesh network structure

Each wireless router in the network is static in their location. The WMN does not change frequently and the channel quality is static. In Figure 1, we illustrate an example of WMN. In this figure, a node stands for a wireless router, which do not only delivers data for its own users but also relays data traffic for the other routers in the network. Among nodes, there are some gateway nodes that are connected to the wired backhaul network. User can send or receive data traffic from outside networks via wired gateway nodes. If node n transmits data to node m directly, there exists a link from node n to node m . In this paper we define link as unidirectional. The WMN under consideration provides a connection-oriented service, where connections are managed in the unit of flow. A flow is a unidirectional.

Data traffic on a flow is conveyed to the destination node through a multi-hop route. We only consider the acyclic routes. Thus, a route can be determined by the set of all intermediate links that the route takes. For a flow there are a number of routes that connect the source and destination. We assume that a flow can utilize multiple routes simultaneously by dividing its data traffic into these routes. Here limit the possible data rate to control the amount of traffic injected to the WMN. The flow data rate, which is defined as the maximum data rate at which the flow f can send data traffic on the route. We can define flow data rate vector. The sum of all components in a flow data rate vector is limited to the "maximum flow data rate". We will call flow data rate vector the "multipath flow data rate vector" if it has more than one route. Otherwise we will refer as "single path flow data rate vector" only for one active route. In case all flows have the single path flow data rate vector, we can denote the "active route vector".

B Physical and medium access control layer model

The proposed scheme can be implemented on top of various physical (PHY) and medium access control (MAC) layer protocols. The effective transmission of the link is defined as the number of actually transmitted bits divided by the time spent for the data transmission, calculated in consideration of retransmissions due to errors. We define the "air time ratio" of the link l . The air time ratio of the link l is defined as the sum of the data rates on the link l divided by the effective transmission rate of the link l .

Roughly, we consider that a fixed portion of the time can be used for data transmission, while the remainder section is used for the purpose of the control, e.g., control message exchange and random back-off. Let β denote the ratio of the time for data transmission to the whole time. The sum of the links in a cluster cannot exceed β .

C Utility and delay penalty as optimization target

The flow longer distance consumes generally more airtime to convey the same amount of time. Therefore, if maximizing system throughput is the optimization target in the WMN, the flows with short distance are likely with long distance. The utility is a highly desirable performance measure since the user satisfaction is the ultimate goal of the network design.

The utility function defines the mapping between the data rate of a flow and the utility of that flow. Since the utility function quantifies the network performance perceived by users when a data rate is given, it can only be estimated by a subjective survey, not by theoretical development. The marginal utility of a flow is the amount of the utility that the system can obtain by assigning a unit data rate to the flow.

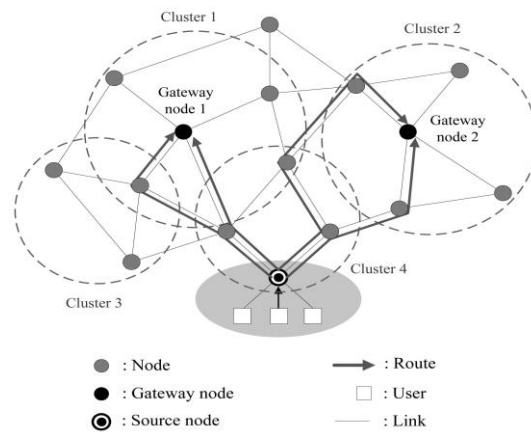


Figure.1. Example mesh network

The delay is also of great importance in the practical WMN, we incorporate the delay term into objective function. To do this, we define the “delay penalty function” for each flow, which penalizes the objective function for selecting the route with long end to end delay.

IV. PROPOSED LOAD-AWARE ROUTING SCHEME

In this section, we design the routing scheme by using the dual decomposition method. We first formulate the optimization problem from the objective function and constraints introduced in the previous section, and derive the dual problem. Next, we explain how to calculate the flow data rate vector for the given Lagrange multipliers, and suggest the subgradient method to iteratively calculate the optimal Lagrange multipliers. Finally we propose the dampening algorithm to alleviate the route flapping problem.

A. Problem formulation

We formulate the optimization problem from air time ratio, β and merged objective function. We solve the optimization problem by converting it to the dual problem according to the Lagrangian method. From the Lagrangian, we define the dual function. From the dual function, we define the dual problem. We can find optimal solution from this problem

B. Flow data rate calculation for given lagrange multipliers

We calculate the flow data rates that maximizes the Lagrangian for given Lagrange multipliers.

Proposition 1: The set of flow data rate vector contains at least one single path flow data rate vector.

Proof: consider the any flow data rate. Let flow data rate be the flow data rate vector such that for the active route that minimizes link cost. This means there exists a single path flow data rate vector.

C. Lagrange multiplier update

We will find the solution of the dual problem. The constraint in the dual problem can be incorporated into the dual function. We define the modified dual function where satisfies the constraint for given Lagrange multiplier.

D. Convergence of flow data rate

We will take the flow data rate vector as the estimation of the optimal flow data rate vector at j th iteration. We will discuss the convergence of this flow data rate vector. Since the optimization problem is strictly feasible and the objective and constraint functions are concave, the strong duality holds from Slater's constraint qualification.

V. DISTRIBUTED IMPLEMENTATION

For implementation, one node with in a cluster is designated as the head of the cluster. The head of the cluster is assumed to be able to communicate with the transmitter nodes of the links in its cluster. The proposed scheme takes the following steps at the j th iteration of the subgradient method. Fig. 2 illustrates an example of control information exchange for this operation.

By the below steps, not only the routing but also the link cost control and the flow control are performed. That is,

- Each cluster head estimates the traffic load with in cluster and the nodes with in the cluster adjust the link costs of its outgoing links, on the basis of estimated loads as in first 5 steps (i.e., link cost control).
- Based on the link costs, the active route for each flow is updated in the steps 6-8 (i.e., routing).
- The flow date is calculated in the step 9.

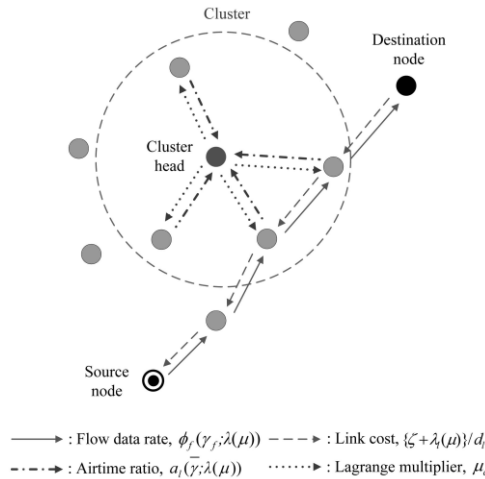


Figure.2. Control information exchange for distributed implementation

- 1) The source node of flow f sends a message containing flow data rate on the active route to the nodes on the active route.
- 2) Each node calculates the air time ratios for its all outgoing links from and broadcasts them to the heads of the clusters to which the links belong.
- 3) The cluster head receives air time ratios for all links in its cluster and updates the Lagrange multipliers.
- 4) The cluster head broadcasts updated Lagrange multiplier to the transmitter nodes of the links in its cluster.
- 5) Each node calculates updated Lagrange multiplier and derives the link cost for its all outgoing links.
- 6) The source node of flow f finds the optimal route.
- 7) The source node of flow f is informed of the link costs on the active route and the new optimal route.
- 8) The source node of flow f sets active route to optimal route if it increase certain margin, if not the active route is not changed.
- 9) The source node of flow f calculates the flow data rate

VI. NUMERICAL RESULTS

The numerical results presented below show that the proposed routing scheme effectively balances traffic load, consequently outperforms the routing algorithm using the ETT as a routing metric. We consider two scenarios, i.e., with and without gateway. To model the load imbalance situation, we introduce the load skewness denoted σ .

A. Gateway scenario

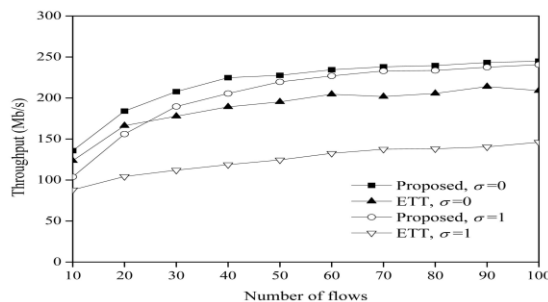


Fig.4. System throughput according to the number of flows in the gateway scenario.

B No gateway scenario

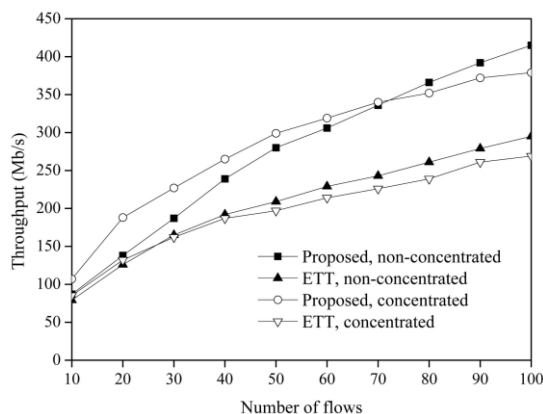


Fig.6. System throughput according to the number of flows in the no gateway scenario.

VII. CONCLUSIONS

In this paper, we have developed a load aware routing scheme for the WMN. We have formulated the routing problem as an optimization problem, and have solved it by using the dual decomposition method. The dual decomposition method makes it possible to design a distributed routing scheme. However, there could be a route flapping problem in the distributed scheme. To tackle this problem, we have suggested a dampening algorithm and have analyzed the performance of the algorithm. The numerical results show the proposed scheme with a dampening algorithm well converges to a stable state, and achieves much higher throughput than the ETT-based scheme does owing to its load-balancing capacity.

FUTURE ENHANCEMENT

The proposed scheme can be applied to various single band PHY/MAC layer protocols. In future work, we can extend the proposed scheme so that we can applied to the multiband protocols, which can provide larger band width to the WMN.

REFERENCES

- [1] R. Bruno, M. Conti, and E. Gregori, "Mesh Networks: Commodity Multihop Ad Hoc Networks," *IEEE Comm. Magazine*, vol. 43, no. 3, pp. 123-131, Mar. 2005.
- [2] D. De Couto, D. Aguayo, J. Bicket, and R. Morris, "High-Throughput Path Metric for Multi-Hop Wireless Routing," *Proc. ACM MobiCom*, Sept. 2003.
- [3] D. Passos, D.V. Teixeira, D.C. Muchaluat-Saade, L.C.S. Magalhaes, and C.V.N. Albuquerque, "Mesh Network Performance Measurements," *Proc. Int'l Information and Telecomm. Technologies Symp.*, Dec. 2006.
- [4] B. Awerbuch, D. Holmer, and H. Rubens, "The Medium Time Metric: High Throughput Route Selection in Multi-Rate Ad Hoc Wireless Networks," *Mobile Networks and Applications*, vol. 11, no. 2, pp. 253-266, Apr. 2006.
- [5] R. Draves, J. Padhye, and B. Zill, "Routing in Multi-Radio, Multi-Hop Wireless Mesh Networks," *Proc. ACM MobiCom*, Sept. 2004.
- [6] Y. Yang, J. Wang, and R. Kravets, "Designing Routing Metrics for Mesh Networks," *Proc. IEEE Workshop Wireless Mesh Networks*, Sept. 2005.
- [7] A.P. Subramanian, M.M. Buddhikot, and S.C. Miller, "Interference Aware Routing in Multi-Radio Wireless Mesh Networks," *Proc. IEEE Workshop Wireless Mesh Networks*, Sept. 2006.
- [8] C.E. Koksal and H. Balakrishnan, "Quality-Aware Routing Metrics for Time-Varying Wireless Mesh Networks," *IEEE J. Selected Areas in Comm.*, vol. 24, no. 11, pp. 1984-1994, Nov. 2006.
- [9] S.J. Lee and M. Gerla, "Dynamic Load-Aware Routing in Ad Hoc Networks," *Proc. IEEE Int'l Conf. Comm.*, June 2001.

Multimode Vector Modalities of HMM-GMM in Augmented Categorization of Bioacoustics' Signals

Mayorga P.¹, Ibarra D.¹, Druzgalski C.²

¹ Depto. de Posgrado, Instituto Tecnológico de Mexicali

² Elec. Eng. Dept., California State. University

ABSTRACT:

A Merged Hidden Markov Model and Gaussian Mixed Models (HMM-GMM) can serve as a very useful tool in classification of dominant characteristics in biological data. In particular, the aim of this approach was to enhance classifications of lung sounds (LS) and heart sounds (HS). In order to achieve these objectives, the LS and HS signals were expressed in terms of Mel-frequency cepstral coefficients (MFCCs) and Quantile acoustic vectors. Once the signals were vectorized, a clusters' quantity analysis for the LS and HS signals was executed for both classes, representing normal abnormal sounds, in such a way that a criterion for the model's size was obtained. The clusters' quantity analysis was carried out applying dendrograms, silhouettes and the Bayesian Information Criterion (BIC). Starting from these computations, the HMM-GMM model architecture for the normal and abnormal classes were conceptualized. The models for the LS signals using Quantile vectors, specifically Quartile, yielded excellent results, while for HS signals, the best results for the HMM-GMM models were obtained with MFCC vectors. In both cases, i.e., LS and HS signals, a close to 100% classification efficiency was achieved for studied cases. Furthermore, the evaluations were assessed in terms of sensitivity and specificity defined as a true positive rate and a true negative rate respectively; LS signals achieved a 100% in sensitivity and specificity, while HS signals also reached a 100%, excluding the normal vs stenosis case, which obtained a 85% in specificity. The importance of this approach lies in the possibility of implementing automated assessment diagnostics for patients with respiratory and cardiac disorders, and essentially the ability to bring this diagnostic capability to remote and limited medical resource areas utilizing low cost technologies.

KEYWORDS: Cluster, Stethoscope, Quantile, MFCC, HMM, Dendrogram, Silhouette, BIC.

I. INTRODUCTION

Bioacoustic approach involving evaluation of the production and perception of biological sounds, including in this case lung sounds (LS) and heart sounds (HS) [2] can be used as a useful diagnostic indicator. The environmental conditions and including air pollution are among critical factors contributing to the increase of respiratory and cardiovascular diseases. Thus, as a part of screening and classification of diagnostic indicators during assisted auscultation one can diagnose the existence of abnormalities of cardiopulmonary origin; for example for the heart, the sounds could make evident the possible presence of Stenosis and Ventricular Septal Defect (VSD) as considered in this project, and for example for the lung's ventilation limitations. Invariably, these sounds and their detection via auscultation, using a traditional stethoscope or other devices including an electronic stethoscope has been a standard practice in medicine. However, the use of a traditional acoustic-mechanical stethoscope is hindered by the degree of the physician's or nurse's experience and their sensory abilities. A description of acoustic indicators by its qualitative nature is frequently used in a subjective way fashion, especially when being evaluated by different medical personnel.

To overcome the drawbacks previously mentioned, one can utilize quantitative methods based among others on pattern recognition. Within the existing methodologies considered were Support Vector Machines (SVM), Linear Discriminant Analysis, Gaussian Mixed Models (GMM) and Hidden Markov Models (HMM). The most important difference is in their way to process data. The HMM processes data or as time series as of state sequences associated to the signal's events, while the other techniques are focused on clusters regardless of the sequences in which they are produced. In other application areas [5], it has been observed that HMM modeling is more susceptible to information loss than to noise, while cluster modeling is more susceptible to noise than to information loss [11, 12]. In this sense, HMM models have advantage in noisy environments, even though it could be computationally costly.

Another attribute about the methodologies mentioned above is the feasibility of their implementation on a simple laptop computer, and could be available in almost all socio-economic scenarios and in remote locations. This is relevant because the world's prevailing socio-economic level is low, for example, in Latin America 70% of the population is lives below the average poverty rate [6]. Moreover, many applications are not necessarily oriented to a traditional third world but to patient's evaluation settings in general [7-9]. In this context, often patient's evaluation settings are located in areas with environmental noise, which interferes with the recordings of LS or HS signals and may negatively impact diagnostic procedures.

An intelligent system (either for voice, cardiopulmonary or other sound signals) simulates the recognition process that the human hearing mechanism performs on the acoustic signal, or in our case an acoustic peculiar event [10]. Most approaches used in intelligent systems for the LS or HS signal classification are based in clusters, classic filtering and other approximations susceptible to noise and to signal degradation during the filtering process. Specifically, the LS signals share a significant frequency range with the HS signals, which suggests that HMM could be a good alternative in this domain [14], since they are oriented to detect event sequences. This project deals with the application of HMM models to LS and HS signals assessment. Besides, two modalities are used as a feature extractor, MFCC already successful in voice and another feature extractor inspired on classifying pathologies based on lung function testing [13]. The HMM models need feature vectors to train the models, which are a state sequences and these states are modeled by Gaussian Mixed Models.

II. MFCC AND QUANTILE FEATURE VECTORS

The feature vectors highlight relevant characteristics of a class by means of values, in such a way that the classification is improved. In this section, the approximations used in the experiments are described and they include MFCC and quantiles.

2.1 Mel-frequency cepstral coefficients (MFCCs) vectors

The MFCC vectors reflect a successful methodology in acoustic featuring, based on cepstraldeconvolution. The cepstrum represents a method based on the Fourier transform, which allows the extraction of the acoustic signal's fundamental frequencies. The MFCC vectors are an extension of the cepstral principles, and their transformation to a nonlinear frequency space is related to human hearing [15-18].

In MFCC, the sounds are parameterized by doing a pre-emphasis with FIR filters, followed by a Hamming window applied to each analysis frame. In this paper, the experiments were carried out using 30 ms Hamming windows with a 15 ms shift for HS signals, to which the Fast Fourier Transform (FFT) was applied; subsequently, the module is obtained and then multiplied by a filter bank whose frequency range and central frequencies are distributed according to the Mel or Bark scale. This is followed by calculating a log stage of the values previously obtained from each filter and subsequently the Inverse Fourier Transform. The outcome is a feature vector called MFCC [15, 19].

2.2Quantile Vectors

Another acoustic vector is the quantile, which is based on the cumulative distribution function (CDF). A random variable's quantile q_p is defined as the smallest value q in such a way that the cumulative distribution function is greater than or equal to a probability p , where p is $0 < p < 1$. This can be calculated from a continuous density probability function $f(x)$ through the Eq.1:

$$p = \int_{-\infty}^{q_p} f(x) dx \tag{1}$$

For acoustic featuring purposes, it is needed to find the quantile coefficients q_p , and for that reason one must start with the CDF inverse function. In the case of acoustic signals such as LS and HS, it is important to

perform the calculations within the limit of stationarity; this limit is determined by the time in which the events are stably generated. Considering a rate of 15 breaths per minute (the usual range for healthy adult subjects is from 12 to 20 breaths per minute and much higher for toddlers), the stationarity is related to the duration of the inhalation, exhalation and the silences in between, which were experimentally determined, obtaining 400 ms (considering about 3 seconds including inhalation, silence and exhalation) [20,21]. A similar analysis was applied to HS signals. In this process, the first stage consists in reading the signal, starting from a *.wav archive; subsequently, the FFT is applied. Fulfilling a basic principle for a probability distribution function, the spectral distribution is normalized (Eq. 2).

$$F_N(f) = \int_{-\infty}^{\infty} \frac{f(t)e^{-j2\pi ft} dt}{\text{arsa}(F(f))} \tag{2}$$

The Eq. 2 guarantees that the sum of the distribution of the frequency values obtained from the FFT will be equal to Eq. 1, therefore N implies a normalization process. A particular quantile example is the use of quartiles, calculated by Eq 3, where each frequency value $f_{0.25}, \dots, f_{0.75}$ corresponds to its respective quartil coefficient. The calculation of the last quartil is not important because it always equals 1, hence a 3 three dimensional vector is obtained.

$$A_{0.25} = \int_{-\infty}^{f_{0.25}} F_N(f) df, \dots, A_{0.75} = \int_{-\infty}^{f_{0.75}} F_N(f) df \tag{3}$$

Algorithmically, A_p , is calculated by an iterative sum to obtain the area and detect the frequency values in which the obtained area is $A = 0.25, \dots, A = 0.75$. The same principle applies to Octile and any other quartil type. For a more extensive description, the paper [21] should be reviewed.

III. CLUSTERS' QUANTITY ANALYSIS FOR THE MODEL DEVELOPMENT

The clusters' quantity used for the model calculation can be defined by means of various techniques. Specifically, the agglomerated data visualization represents an important criterion for the clusters' quantity definition. In this section, some techniques to optimize the results are assessed through an analytical approach. The techniques discussed include the analysis with dendrograms, silhouettes, and the Bayesian Information Criterion (BIC).

A dendrogram is basically a tree diagram based on the distance from each datum point against the others, which associates those closer together (considering a distance metric, e.g., Euclidean). Here, it is meant that the closer the data points are, the greater the probability of belonging to the same cluster. With this, the data points are linked one to one until all data is related to one cluster, as shown in Figure 1 [33].

The silhouettes represent the number of existing clusters in a time series. Firstly, the quantity of clusters is chosen. Subsequently, the silhouettes divide the data in the quantity of clusters specified, showing the probability of belonging to a cluster (Figure 2, right side), and the uncertainty of not belonging to such cluster (Figure 2, left side) [34, 35].

Another alternative to analyze the quantity of clusters in a time series is applying the Bayesian Information Criterion (BIC), as shown in Figure 3. The model with the highest BIC value is considered the "best" model [36]. The BIC is useful to estimate how well the model is adjusted to the data, considering the number of parameters in the GMM model, namely: weights, covariance matrices and means [36]

$$p(X|M_g) \approx BIC_g = 2 \log p(X|\hat{\theta}_g M_g) - m_g \log(n) \tag{4}$$

In our study case, it is important to determine the clusters' quantity of HS and LS signals. For BIC curves, the best model is influenced by the covariance type applied.

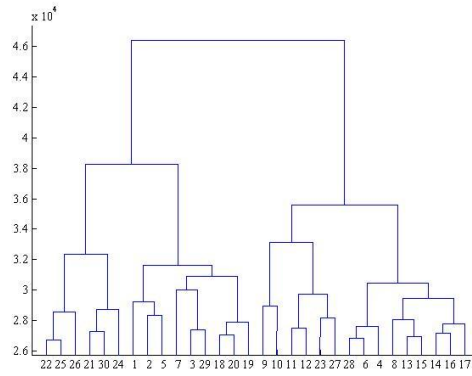


Figure 1. Dendrogram for normal LS signal

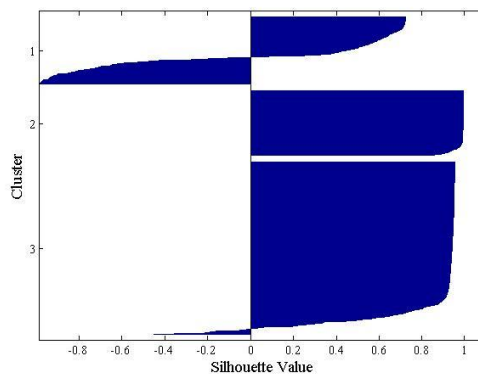


Figure 2. Silhouette for normal LS signal

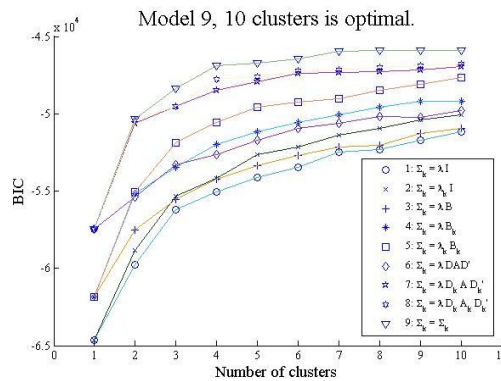


Figure 3. Best model according BIC curve for LS normal signal

IV. MODELLING

4.1 Gaussian Mixed Models (GMM) and Hidden Markov Model (HMM)

In this project, the GMM was applied as an emission function for the HMM states. Since the GMM models have been successful in other areas related to analysis of acoustic signals, they are used in this project as a representation of the states in the HMM models for the LS and HS signals.

4.1.1 GMM Models

A GMM model represents a triplet composed by the means, covariances and weights; generally, each class is represented by a GMM Δ model (in our case the model's states). A model Δ is trained with the acoustic vectors obtained from the signals' sampled data. The GMM modeling uses the expectation-maximization (EM)

algorithm to train the models $\Lambda_i = \{m_i, \vec{\mu}_i, \Sigma_i\}$. This calculation is performed with the acoustic vectors extracted from the different recordings (LS or HS). The mean $\vec{\mu}_i$ represents the average over all the vectors, while the covariance matrix Σ_i models the characteristics variability on the acoustic class [16, 22].

$$p(\vec{x}|\Lambda) = \sum_{i=1}^M m_i b_i(\vec{x}) \tag{5}$$

Where \vec{x} is a random D-dimensional vector (MFCC, Octile or Quartile acoustic vectors), $b_i, \forall i = 1, \dots, M$ are the component densities and $m_i, \forall i = 1, \dots, M$ are the mixtures weight [5, 23-25]. Here, $\vec{\mu}$ represents a mean vector and Σ_i is the covariance matrix. Besides, the weights for the mixtures must satisfy the constraint $\sum_{i=1}^M m_i = 1$. The GMM models are parameterized by mean vectors, covariance matrices and Gaussian mixture weights constituting each state of the HMM model. Then, each Gaussian density contains the parameters represented by the following expression [5, 23-25]:

$$b_i(\vec{x}) = \frac{1}{(2\pi)^{\frac{D}{2}} |\Sigma_i|^{\frac{1}{2}}} \exp\left\{-\frac{1}{2}(\vec{x} - \vec{\mu}_i)^T \Sigma_i^{-1} (\vec{x} - \vec{\mu}_i)\right\} \tag{6}$$

4.1.2 HMM Models

The cardiac cycle is sequential and acoustically primarily consists of two main events known as the first heart sound, “S1” and the second heart sound “S2”, as shown in Figure 4. The S1 refers to the mitral and tricuspid valves closure, while “S2” is generated by the aortic and pulmonary valves operation. The lung sounds (LS) occurrence is also a cyclical process formed by two main events, inhalation and exhalation.

In both cases, HS and LS signals, there are silences in between the main events, which are different depending on the event taking place before and after. Therefore, both cases are sequences of events that may vary depending on the circumstances, health conditions, and even the person’s mood.

In HS analysis, S1 and S2 as well as the silences, could be the stages of the signal to model, while for the LS, the inhalation, exhalation and the silences could be the signal’s stages to model (Figure 4). Then, these are modeled through Hidden Markov Models (HMM), which represents a finite state automaton.

In this project, the experiments were carried out with HS and LS signals separately; however, the main purpose is to utilize a HMM-GMM architecture as a combined HS-LS diagnostic assessment tool.

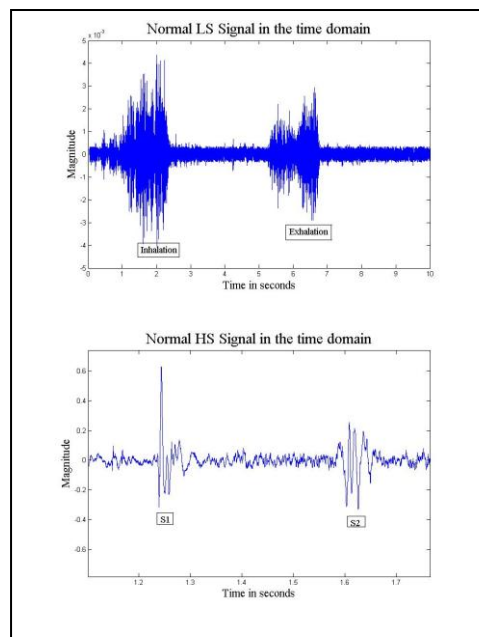


Figure 4. Normal signals in time domain, LS (upper), HS (lower)

A HMM can be considered as a state-based model, in which each state is not directly observed, in fact, each one is characterized by a GMM that models the observations (acoustic vectors) corresponding to the state. Formally, a HMM is defined by the following components [26]:

- $S = \{S_1, S_2, \dots, S_N\}$ is the finite set of possible states (hidden);
- The transition matrix $A = \{a_{i,j}, 1 \leq j \leq N\}$, corresponding to the probability to transit from a state S_i to a state S_j . $a_{i,j} = P[q_{t+1} = S_j | q_t = S_i], 1 \leq i, j \leq N$ with the constraint $a_{i,j} \geq 0, \sum_{j=1}^N a_{i,j} = 1$, where q_t denotes an occupied state at a time t .
- The emission function of a state j (in our case a GMM) $B = \{b(O|S_j)\}$, denotes the emission probability for an observation $O \in V$ when the system is at the state S_j ; V corresponds to continuous observations, for this project experiments, MFCC or Quantile acoustic vectors were applied, hence $b(O|S_j)$ is a GMM model.
- $\pi = \{\pi_i\}$, the probabilities of initially being in a state i , $\pi_i = P[q_1 = S_i], 1 \leq i \leq N$ Con $\pi_i \geq 0$ and $\sum_{i=1}^N \pi_i = 1$.

As in the case of GMM models, the HMM are conventionally expressed as triplets $\lambda = (A, B, \pi)$. An example of an acoustic signal HMM model is shown on the Figure 5.

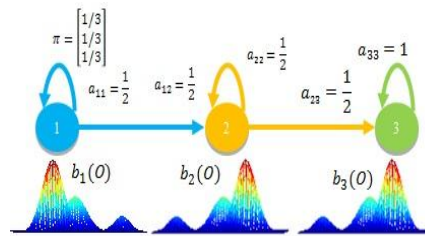


Figure 5.HMM model as triplet

The training for the HMM parameters, given a set of observation sequence $\{O_i\}$, is normally done by applying the Baum-Welch algorithm [26], which resolves the parameters by maximizing the likelihood or probability $P(O_i|\lambda)$. For the evaluation stage, it is required to calculate $P(O|\lambda)$, given the model λ and a sequence O of observations; here the forward-backward algorithm was applied [26].

4.2 Confusion Matrix (or Contingency Table)

In a classification problem it is possible to evaluate the efficiency of the system by confusion matrices, also known as contingency tables, where formally, an instance is mapped to a set labeled as positive class (Y) or negative class (N), and the system's hypothesis can yield a positive class (p) or negative class (n). Considering a binary classifier and an instance, there are four possible outcomes [32, 33, 37]:

- True positive: positive instance classified as positive.
- False negative: positive instance classified as negative.
- True negative: negative instance classified as negative.
- False positive: negative instance classified as positive.

This process is illustrated on the Table1:

Table1. ConfusionMatrix

ConfusionMatrix		Input	
		Y	N
Prediction	p	TP	FP
	n	FN	TN

The importance of the contingency tables is to express the results in terms of sensitivity, specificity and accuracy because these terms are fairly standard in the medical domain.

- Sensitivity (TPR, true positive rate)

$$TPR = \frac{TP}{P} = \frac{TP}{TP+FN} \tag{6}$$

- Specificity (TNR, true negative rate)

$$TNR = \frac{TN}{N} = \frac{TN}{FP+TN} \tag{7}$$

- Accuracy (ACC):

$$ACC = \frac{TP+TN}{P+N} \tag{8}$$

V. DATABASES

The set of HS signals used for these experiments came from databases available for academic and scientific purposes [27, 28]. Specifically, for this project this included, a set of HS recordings comprising of 21 HS signals recorded at the sampling frequency of 11025 Hz, and a 9 to 12 seconds duration, “.wav” format and mono channel. The original signals were captured with a 44 kHz and 22 kHz rate, but were sub-sampled at 11 kHz.

These signals include seven Normal, seven Stenosis and seven Ventricular Septal Defect (VSD). In order to train and evaluate the HMM models, these signals had to be partitioned. The evaluation and the modeling were performed by applying cross-validation and contingency tables.

For the LS signals experiments, two databases (RALE and BDITM) were used. The first database is RALE and consists of a set of normal and adventitious LS sounds as .wav format recordings, which was developed in Winnipeg, Canada. The signals from RALE were filtered with a 7.5 Hz band-pass to suppress any DC offset by means of a first order Butterworth filter. Besides, an eight-order Butterworth low-band filter was applied at 2.5 kHz to avoid overlapping. The signals from the database were sampled at 11025 Hz. For this project, the adventitious signals used were crackles and wheezes.

The other database used was BDITM, which comprises of only normal lung sounds recordings from students in the age range of 18 to 25 years. In the LS case, the evaluation was performed by means of cross-validation, leaving a signal to evaluate, and using the remaining signals to calculate the model and changing the settings until all possibilities were exhausted. The signals used were seven normal from BDITM, seven Crackles and seven Wheeze sounds sequences from RALE.

VI. RESULTS

The Table 2 and Table 3 show the best value for Bayesian Information Criterion (BIC), where quartile vectors with a 400 ms frame, 300 ms shift and a full covariance were used. The BIC calculus gives us the idea about the possible size of the models, since it gives the best model in order to adapt it to the data. Furthermore, an acceptable quantity of clusters spans from 3 to 4 for LS signals, and 3 to 8 for HS signals.

Table 2. Best models for LS signals using BIC and Quartiles

Signal	Covariance type	Number of Gaussians
Normal	full	10 (tentative)
Crackles	full	3
Wheeze	full	4

Table 3. Best models for HS signals using BIC and Quartiles

Signal	Covariance type	Number of Gaussians
Normal	full	6
Stenosis	full	8
VSD	full	3

To evaluate the efficiency of the HMM models for the LS and HS signals (shown in Table 4 and Table 5), the octile and quartile vectors were calculated with 400 ms frames and 300 ms shifts (i.e. 100 ms overlap). As far as it regards MFCC vectors, these were calculated with 30 ms frames, 15ms shifts and 12 cepstral coefficients. For these experiments, dimensionality reduction was not applied because in previous trials it did not provide a significant improvement [10, 38].

The values obtained from the Table 4, are values considering three classes: Normal, Crackles, and Wheeze. The signals were partitioned in three sets for the HMM calculation of each class; a signal was extracted

to test the models, i.e., of all three classes, one class contained only six signals to train the model while the rest contained seven. For this process, the test signal was alternated until all the possibilities were exhausted and 21 evaluations were performed.

Table 4. Best results of LS signals with HMM models using 3 Gaussians, 3 states and 3 iterations

Covariance type	Vector type	Efficiency
Complete	Quartile	95.2381
Diagonal	Quartile	100
Spherical	Octile	95.2381

Table 5. Best results of HS signals with HMM models using 3 Gaussians, 3 states and 3 iterations

Covariance type	Vector type	Efficiency
Complete	Octile	47.6190
Diagonal	MFCC	76.1905
Spherical	MFCC	100

The HMM models for the LS were calculated using three states ($N_s = 3$), three Gaussians ($k = 3$) and three iterations ($it = 3$). The HMM architecture used was left-to-right (Bakis), and the states were represented with GMM models, as shown by Figure 5. The proposed architecture concept came from the experiments with BIC, Silhouettes, Dendrograms and previous works (as mentioned before).

Here, the vector π denotes the initial probabilities (a priori) of being in some state q , and the values a_{ij} are the transition probabilities between states, while $b_j(\mathbf{O})$ are the emission functions of an observation in some state (in this case a GMM). It is important to note that the transition probabilities and their initial state were initialized randomly.

Moreover, Table 5 shows the best results for the experiments using HS signals. For this case, three classes were also used: Normal, Stenosis and VSD, each class having seven signals, so, a database with 21 signals was obtained. The procedure for the partition and evaluation of the model was the same used for the LS signals previously mentioned. Namely, 21 evaluations were performed, wherein the HMM model (left-to-right type) were calculated using three states ($N_s = 3$), three Gaussians ($k = 3$) and three iterations ($it = 3$). It can be observed in Table 4 that a 100% efficiency was obtained using quartiles for LS signals. On the other hand, as shown in Table 5 a 100% efficiency was obtained using MFCC vectors for HS signals.

The covariance is important when one wants to model the clusters' shape, volume and orientation for each class; the full covariance involves more calculations, more iterations, more data and convergence is not always achieved for the models, hence, it is necessary to analyze the models before proposing a final HMM-GMM architecture. However, to validate the previous remark, it is useful to have a larger number of signals per class since the full covariance is more versatile.

In order to carry out evaluations in terms of sensitivity and specificity, two classes were considered experimentally, one including the normal class, and another corresponding to an adventitious class (Crackles or Wheeze for LS; Stenosis or VSD for HS signals). Here, 14 signals were used for each experiment, seven in each class. To calculate the HMM model the configuration used was $it = 3, N_s = 3, K = 3$, while the evaluation was implemented by means of cross-validation and contingency tables.

The best results obtained for LS signals are shown on Table 6 and Table 7, where a 100% efficiency was achieved applying quartile vectors and a full or spherical covariance. However, for HS signals, the results were not 100% considering Stenosis as an adventitious signal, as for the VSD case, as shown by Table 8 and Table 9, both using a spherical covariance. The fact that the MFCC vectors allowed a better classification must be highlighted.

Table 6. Results of HMM model evaluation using 3 Gaussians, 3 states and 3 iterations for LS signals and Quartiles.

Normal vs. Crackles	Input		Sensitivity	Specificity
	p	n		
Output	P	7 0	1	1
	N	0 7		

Table 7. Results of HMM model evaluation using 3 Gaussians, 3 states and 3 iterations for LS signals and Quartiles.

Normal vs. Wheeze	Input		Sensitivity	Specificity
	p	n		
Output	P	7 0	1	1
	N	0 7		

Table 8. Results of HMM model evaluation using 3 Gaussians, 3 states and 3 iterations for HS signals and MFCC

Normal vs. VSD	Input		Sensitivity	Specificity
	p	n		
Output	P	7 0	1	1
	N	0 7		

Table 9. Results of HMM model evaluation using 3 Gaussians, 3 states and 3 iterations for HS signals and MFCC

Normal vs. Stenosis	Input		Sensitivity	Specificity
	p	n		
Output	P	7 1	1	0.8571
	N	0 6		

For the contingency tables, the input signals are denoted by p and n, and the hypothetical recognition given by the system’s output is P and N. From the tables, one can observe an excellent efficiency of the system to detect true positives (normal sounds) and true negatives (pathologies). Based on the results, it may be concluded that the quartile vectors are more suitable for LS while the MFCC vectors are better for HS signals. Considering the MFCC background for voice processing, the HS sounds are closer to phonetic acoustic signals so the MFCC are capable to reveal fine details for these signals. On the other hand, the LS signals seem more like noise and have a broader spectrum, with less defined formants compared to the phonetic acoustic signals. Hence, the quartile vectors are efficient for the LS signals, but the MFCC are better for the HS case. Another aspect to highlight is the HMM model robustness to noise, which suggests that in events’ sequences during noise presence, a HMM combined with a GMM is superior to a GMM modeling alone. The results obtained here are similar but superior to the ones obtained previously by applying linear discriminants [10].

VII. CONCLUSIONS

The experimental data shows remarkable capacity of the HMM-GMM twofold technique to classify LS and HS signals with different vector modalities: Octiles, Quartiles and MFCC. In both cases of LS and HS signals, a 100% classification efficiency was achieved. In an evaluation of LS and HS, the HMM-GMM concept made it possible to differentiate normal signals from pathologies. The size model analysis with the Bayesian Information Criterion (BIC) was not decisive since convergence was not always achieved; the best cases included three clusters. Besides, these sets of three clusters were consistent with the HMM models and their efficiency results, which reached up to 100% in terms of sensitivity and specificity.

Another important consideration to note, as demonstrated in the Table 4 and Table 5, is that the covariance type combined with a certain kind of vector influences the results. In this case, the diagonal and spherical covariances were the most consistent. As previously discussed in other papers [30, 31], the event sequence modeling for LS and HS with HMM, seems to be superior to the GMM modeling alone. Besides, HMM turned out to be less sensitive to noise, in spite of the HS interference with the LS signal’s sequence of events.

This is advantageous for the quantitative screening and use in medical facilities with inadequate resources, as well as medical personnel with limited training levels, so the classification can be performed automatically. In the future, it would be useful to extend this classification to other pathologies and to specific

sectors of the population to assess the effects of localized pollution. In addition, the implementation of inclusive architecture to classify LS and HS signals with indexed events will represent beneficial diagnostic tool.

REFERENCES

- [1] Kosmidou V E, Hadjileontiadis L J. "Sign language recognition using intrinsic-mode sample entropy on sEMG and accelerometer data". *IEEE Trans Biomed Eng*, 2009; 56(12): 2879-90.
- [2] Gaunt S L, Nelson D A, Dantzker M S, Budney G F, Bradbury J W, Zink R. "New directions for bioacoustics collections". *The Auk*, 2005; 122(3): 984-987.
- [3] Reyna-Carranza M A, Moreno-Flores A P, Lopez-Avitia R. "Acute respiratory infections and its Spearman correlation with meteorological and air pollutants data from Mexicali, BC, Mexico". *PAHCE-2010 (Pan American Health Care Exchanges Conf. 2010)*, 2010; Lima, Peru
- [4] Reyna-Carranza M A, Merida-Palacio J V, Soria-Rodriguez C. "Acute effects of the PM10 and O3 in the healthy school children pulmonary function from Mexicali, BC, Mexico". *PAHCE-2010 (Pan American Health Care Exchanges Conf. 2010)*, 2010; Lima, Peru
- [5] Mayorga P, Besacier L, Lamy R, Serignat J F. "Audio packet loss over IP and speech recognition". *Automatic Speech Recognition and Understanding*, 2003. ASRU '03. 2003 IEEE Workshop on, 2003;
- [6] (CEPAL) C E P A L Y E C. "Panorama Social de AméricaLatina <http://www.eclac.org/publicaciones/xml/5/48455/PanoramaSocial2012DocI-Rev.pdf>". 2012;
- [7] Moussavi Z. "Respiratory sound analysis". *IEEE Engineering in Medicine and Biology Magazine*, 2007; 26 (1): 15.
- [8] Gnitecki J, Moussavi Z, Pasterkamp H. "Diagnostic potential in state space parameters of lung sounds". *Medical & biological engineering & computing*, 2008; 46(1): 93-99.
- [9] Charleston-Villalobos S, Martinez-Hernandez G, Gonzalez-Camarena R, Chi-Lem G, Carrillo J G, Aljama-Corrales T. "Assessment of multichannel lung sounds parameterization for two-class classification in interstitial lung disease patients". *Comput Biol Med*, 2011; 41(7): 473-82.
- [10] Mayorga Ortiz P, Druzgalski C, Criollo Arellano M, González Arriaga O. "GMM y LDA Aplicado a la Detección de Enfermedades Pulmonares". *Revista Mexicana de Ingeniería Biomédica*, 2013; 34(2):
- [11] Solé-Casals J, Zaiats V. "Advances in nonlinear speech processing". *International Conference on Nonlinear Speech Processing, NOLISP 2009*, 2009;
- [12] Milner B, James A. "Robust speech recognition over mobile and IP networks in burst-like packet loss". *Audio, Speech, and Language Processing*, *IEEE Transactions on*, 2006; 14(1): 223-231.
- [13] Kiyokawa H, Pasterkamp H. "Volume-dependent variations of regional lung sound, amplitude, and phase". *Journal of Applied Physiology*, 2002; 93(3): 1030-1038.
- [14] Besacier L, Mayorga P, Bonastre J F, Fredouille C, Meignier S. "Overview of compression and packet loss effects in speech biometrics". *Vision, Image and Signal Processing, IEE Proceedings -*, 2003; 150(6): 372-376.
- [15] Istrate D M. "Detection et Reconnaissance des Sons pour la Surveillance Médicale, These Doctorale, France". *INPG*, 2003; 183.
- [16] Mayorga P, Druzgalski C, Vidales J. "Quantitative Models for Assessment of Respiratory Diseases". *PAHCE-2010 (Pan American Health Care Exchanges Conf. 2010)*, 2010; Lima, Peru. DOI: 10.1109/PAHCE.2010.5474607
- [17] Milner B, Semnani S. "Robust Speech Recognition over IP Networks". *IEEE Int. Conf. on Acoustics, Speech, and Signal Processing, ICASSP2000*, Jun 2000; Istanbul, Turkey
- [18] Pearce D. "An Overview of ETSI Standards Activities for Distributed Speech Recognition Front-Ends". *AVIOS 2000: The Speech Applications Conference*, May 22-24 2000; San Jose, CA, USA
- [19] Fredouille C, Mariéthoz J, Jaboulet C, Hennebert J, Mokbel C, Bimbot F. "Behavior of a Bayesian Adaptation Method for Incremental Enrollment in Speaker Verification". *IEEE Int. Conf. on Acoustics, Speech and Signal Processing (ICASSP2000)*, 2000; Istanbul, Turkey
- [20] Mayorga P, Olguín M, González O H, Flores N, Luis V. "Quantile Acoustic Vectors vs. MFCC Applied to Speaker Verification". *International Journal of Advanced Robotic Systems*, 2013;
- [21] Mayorga P, Druzgalski C, González O H, Lopez H S. "Modified classification of normal Lung Sounds applying Quantile Vectors". *Engineering in Medicine and Biology Society (EMBC), 2012 Annual International Conference of the IEEE*, 2012;
- [22] Mayorga P, Druzgalski C, González O H, Zazueta A, Criollo M A. "Expanded Quantitative Models for Assessment of Respiratory Diseases and Monitoring". *PAHCE-2011 (Pan American Health Care Exchanges Conf. 2011)*, March 2011; Rio de Janeiro, Brazil. DOI: 10.1109/PAHCE.2011.5871917
- [23] Pearce D. "An Overview of ETSI Standards Activities for Distributed Speech Recognition Front-Ends". *AVIOS 2000: The Speech Applications Conference*, 2000.; San Jose, California, USA
- [24] Reynolds D. A. "Gaussian Mixture Modeling Approach to Text-Independent speaker Identification ". *Georgia Institute of Technology*, 1992;
- [25] Webb Andrew R. *Statistical Pattern Recognition*. John Wiley & Sons Ltd, 2002.
- [26] Rabiner L R, Juang B H. *Fundamentals of speech recognition*. PTR Prentice Hall (Englewood Cliffs, N.J.), 1993.
- [27] "Boston Children's Hospital <http://www.childrenshospital.org/>".
- [28] "Texas Heart Institute <http://www.texasheartinstitute.org/AboutUs/index.cfm>".
- [29] Mayorga P, Druzgalski C, Gonzalez O H. "Quantile vectors based verification of normal lung sounds". *PAHCE-2012 (Pan American Health Care Exchanges Conf. 2012)*, 2012; Miami, Florida. DOI: 10.1109/PAHCE.2012.6233424
- [30] Mayorga P, Druzgalski C, Miranda J, Zeljkovic V, Gonzalez O H. "The HMM diagnostic models of respiratory sounds". *PAHCE-2014 (Pan American Health Care Exchanges Conf. 2014)* 2014; Brasilia, Brazil. DOI: 10.1109/PAHCE.2014.6849611
- [31] Mayorga P, Druzgalski C, Calderas D, Zeljkovic V. "Multimodal classification of heart sounds attributes". *PAHCE-2014 (Pan American Health Care Exchanges Conf. 2014)* 2014; Brasilia, Brazil. DOI: 10.1109/PAHCE.2014.6849615
- [32] Fawcett T. "An Introduction to ROC Analysis". *Pattern Recognition Letters*, EISEVIER, 2005;
- [33] Benabdeslem, K.; Bennani, Y., "Dendrogram based SVM for multi-class classification," *Journal of Computing and Information Technology-CIT* 14, 2006, 4, 283-289;
- [34] Xue Mei Lu; Sung Jong Eun; Taeg Keun Whangbo, "Vector Silhouette Extraction for Generating Blueprint," *Automation and Logistics*, 2007 IEEE International Conference on , vol., no., pp.2946,2951, 18-21 Aug. 2007
- [35] Xuejun, Li; Jiaguang, Sun; Changgui, Yang, "Extracting silhouette curves of NURBS surfaces by tracing silhouette points," *Tsinghua Science and Technology*, vol. 3, no. 2, pp. 1005, 1008, June 1998.

- [36] Jianhua Zhao, "Efficient Model Selection for Mixtures of Probabilistic PCA Via Hierarchical BIC," *Cybernetics, IEEE Transactions on*, vol.44, no.10, pp.1871,1883, Oct. 2014.
- [37] Marom, N.D.; Rokach, L.; Shmilovici, A., "Using the confusion matrix for improving ensemble classifiers," *Electrical and Electronics Engineers in Israel (IEEEI), 2010 IEEE 26th Convention of*, vol., no., pp.000555,000559, 17-20 Nov. 2010
- [38] Mayorga Ortiz P, Druzgalski C, Miranda Vega, J. E., Calderas Ochoa D. O. "Modelos Acústicos HMM Multimodales para Sonidos Cardiacos y Pulmonares". *Revista Mexicana de Ingeniería Biomédica*, 2014; 35(3).